NTNU
Norwegian University of
Science and Technology

Exploring V_2C MXene as Cathode Constituent for Rechargeable Magnesium Batteries

Lars-Arne Boge

Nanotechnology
Submission date: July 2019
Supervisor: Kjell Wiik, IMA
Co-supervisor: Henning Kaland, IMA
Frode Håskjold Fagerli, IMA

Norwegian University of Science and Technology
Department of Materials Science and Engineering

Preface

This thesis has been completed in partial fulfilment of the requirements for the degree of Master of Science in Nanotechnology at NTNU. The project has been carried out at the Department of Materials Science and Engineering, under the supervision of Prof. Kjell Wiik, and has been strongly connected to the projects of PhD candidates and co-supervisors Henning Kaland and Frode Håskjold Fagerli.

I would like to start by thanking my supervisor Kjell for his guidance and valuable feedback throughout the project. Moreover, I would like to express my eternal gratitude to Henning and Frode, for the countless hours you have dedicated to mentoring me and guiding my work; this would not have been possible without your help. Specifically, the co-supervisors are thanked for performing the etching procedures for me, for allowing me to use some of their mixed electrolytes, for the introduction to several of the experimental techniques used in this project, and for their valuable feedback on my written work. Furthermore, I would like to thank Fride Vullum-Bruer for her help in the early stages of this project.

Lars-Arne Boge

Trondheim, 02.07.2019

Abstract

Rechargeable magnesium batteries are envisioned to outperform state-of-the-art Li-ion batteries with regard to volumetric capacity, safety, cost and scalability. The major challenges halting the development and commercialization of magnesium based batteries consist of finding cathode materials that are able to host Mg-ions, and electrolytes that are compatible with magnesium metal anodes. A relatively new family of two-dimensional transition metal carbides, nitrides and carbonitrides, known as MXenes, have been proposed as possible constituents in different cathode designs for rechargeable magnesium batteries, due to their favourable electronic conductivity and intercalation properties. In this work, V_2C MXene, which has previously been demonstrated to intercalate mono-, di- and trivalent ions, has been synthesised and electrochemically characterized in different cathode designs to assess its performance as a constituent in cathodes for rechargeable magnesium batteries.

To prepare the V_2C MXene, the parent V_2AlC MAX phase was synthesised by sintering a mixture of vanadium, aluminium and carbon powder precursors, followed by exfoliation of the aluminium monolayers from the MAX phase structure utilizing a solution of concentrated hydrofluoric acid. The particle size and etching duration were optimized with regard to completeness of the exfoliation process. Additionally, a V_2C-S composite was synthesised by a melt diffusion technique. The crystallinity, phase purity, morphology and elemental composition of the MAX phase, MXene and composite material were characterized by X-ray diffraction, scanning electron microscopy and energy-dispersive X-ray spectroscopy. Insertion type cathodes were prepared by drop casting a slurry containing the MXene material onto graphite paper discs, while conversion type cathodes were prepared by tape casting a slurry containing the MXene-S composite onto aluminium foil. Coin cells utilizing the insertion cathodes were assembled using three different electrolytes, and tested by electrochemical cycling. The conversion cathodes were assembled in both Mg-S and Li-S systems, and tested by electrochemical cycling. After cycling, the Mg-S system was disassembled and subjected to post-mortem characterization by scanning electron microscopy and energy-dispersive X-ray spectroscopy, with the purpose of investigating possible side reactions.

The optimized etching parameters were found to result in the complete exfoliation of the V_2AlC MAX phase, yielding a V_2C MXene powder free of the parent MAX phase. Although, significant amounts of secondary phases were observed in the synthesised MXene samples. During the electrochemical cycling, the cells utilizing the insertion cathodes displayed extremely poor performances with negligible charge and discharge capacities, suggesting that reversible intercalation of Mg-ions into the MXene structure was not taking place as intended. The Mg-S system utilizing a V_2C-S conversion cathode displayed a decent initial discharge capacity of 312.4 mAh/g, but was found to suffer from serious polysulfide shuttling, which was confirmed by the post-mortem investigation, resulting in a severely limited cycling performance following the initial cycle. The Li-S systems utilizing the conversion cathodes displayed decent capacities of approximately 400 mAh/g for several hundred consecutive cycles, thus verifying the conversion cathode design. In spite of the poor performances observed for the magnesium battery systems in this work, further efforts should be directed towards investigating possible routes to achieve Mg-ion intercalation in the insertion cathodes design, as well as possible ways to mitigate the polysulfide shuttling effect hindering the realization of practical Mg-S batteries.

Sammendrag

Oppladbare magnesiumbatterier er spådd å kunne utkonkurrere moderne Li-ion-batterier når det kommer til volumetrisk kapasitet, sikkerhet, pris og skaleringspotensiale. Hovedutfordringene som står i veien for utviklingen og kommersialiseringen av magnesiumbaserte batterier består av å utvikle katodematerialer som kan fungere som vert for Mg-ioner, og i tillegg utvikle elektrolytter som er kompatible med anoder av magnesiummetall. En relativt ny familie av todimensjonale overgangsmetallkarbider, nitrider og karbonitrider, kjent som MXener, har blitt foreslått som mulige bestanddeler i forskjellige katodetyper for oppladbare magnesiumbatterier, med bakgrunn i at materialene har god elektroniske ledningsevne og gode interkaleringsegenskaper. I dette prosjektet har V_2C MXene, som tidligere har vist seg å interkalere mono-, di- og trivalente ioner, blitt syntetisert og elektrokjemisk testet som bestanddel i forskjellige typer katoder, med hensikt å vurdere materialets egnethet som bestanddel i katoder for oppladbare magnesiumbatterier.

I fremstillingen av V_2C MXenen ble først V_2AlC MAX-fasen, som er utgangsfasen, syntetisert ved sintring av en blanding av vanadium-, aluminium- og karbonpulverforløpere, etterfulgt av eksfoliering av monolagene med aluminium fra MAX-fasestrukturen ved bruk av en løsning med konsentrert flussyre. Partikkelstørrelsen og etsetiden ble optimalisert med fokus på fullstendig fjerning av aluminiumslagene fra MAX-fasestrukturen. I tillegg ble en V_2C-S kompositt syntetisert med en teknikk basert på diffusjon av flytende svovel. Krystallinitet, fase renhet, morfologi og kjemisk sammensetning av MAX-fasen, MXenen og kompositten ble karakterisert ved røntgendiffraksjon, elektronmikroskopi og energidispersiv røntgenspektroskopi. Innsettingskatodene ble fremstilt ved å dryppe en oppslemming som inneholdt MXene-materialet på grafittpapirskiver, mens konverteringskatodene ble fremstilt ved støping av en oppslemming inneholdende MXene-S-kompositten på aluminiumsfolie. Knappceller med innsettingskatoder ble satt sammen med tre forskjellige elektrolytter og testet ved elektrokjemisk sykling. Konverteringskatodene ble inkorporert i både Mg-S og Li-S-systemer og testet ved elektrokjemisk sykling. Etter sykling ble Mg-S-systemet demontert og post-mortem elektronmikroskopi og energidispersiv røntgenspektroskopi ble utført, med det formål å undersøke om potensielle sidereaksjoner hadde funnet sted under syklingen.

De optimaliserte etseparametrene resulterte i fullstendig eksfoliering av V_2AlC MAX-fasen, noe som ga et V_2C MXene pulver fritt for den overordnede MAX-fasen, men med signifikante mengder sekundære faser. Under den elektrokjemiske syklingen viste cellene med innsettingskatoder ekstremt dårlige ytelse og veldig lave ladnings- og utladningskapasiteter, som tyder på at reversibel interkalering av Mg-ioner i MXene-strukturen ikke fant sted. Mg-S-systemet med V_2C-S konverteringskatode viste en relativt høy utladningskapasitet på 312,4 mAh / g for den første syklusen, men viste senere tegne til alvorlig skyttel av polysulfider under sykling, og dette ble bekreftet av post-mortem undersøkelsene. Dette resulterte i en veldig begrenset ytelse i de resterende syklene. Li-S-systemene som benyttet konverteringskatoder viste gode kapasiteter på ca. 400 mAh / g for flere hundre påfølgende sykluser, og dette verifiserte at konverteringskatoden fungerte som den skulle. Til tross for de dårlige ytelsene som observeres for magnesiumbatteriene i dette prosjektet, bør ytterligere innsats rettes mot å undersøke mulige veier for å oppnå Mg-ion-interkalering i innsettingskatoder, så vel som mulige måter å redusere skyttel-effekten av polysulfider som hindrer realisering av praktiske Mg-S batterier.

Table of Contents

Chapter 1

Introduction

1.1 Background and motivation

Modern human society is experiencing rapid technological, economic and social development, leading to an ever-increasing demand for energy to maintain the accelerated advancement of society[1,2]. Today, more than 85% of the energy consumed annually is derived from fossil fuels[3], resulting in serious challenges related to global warming and environmental pollution[2,4–6]. It is commonly accepted that the non-renewable fossil fuels must be gradually replaced by sustainable alternatives, such as wind energy, solar energy, geothermal energy and tidal power[2,4], in order to mitigate the negative consequences of global warming. However, these renewable sources of energy are all inherently intermittent, prompting the need for advanced energy storage technologies with the ability to efficiently store and distribute energy upon demand. Additionally, due to the increasing global population, the worldwide energy demand is predicted to double by 2050[7,8], further strengthening the need for new sustainable energy conversion and storage technologies.

Following the technological development of the last thirty years, rechargeable batteries have become immensely popular as an energy storage technology, and are today utilized in everything from personal electrical devices to electrical energy storage systems that stabilize the power grid. At present, the global battery market is divided between a number of competing technologies, including nickel-metal hydride (NiMH), nickel-cadmium (NiCd), lead-acid batteries and Li-ion batteries (LiBs). LiBs have proven to be more competitive than the other rechargeable battery technologies in terms of energy density, power density and durability[9]. However, the introduction of the electric vehicles prompted an urgent need to further improve the existing LiB systems with respect to energy density and cost per unit of stored energy[10], as this was considered necessary to increase the market acceptance of the new vehicle technologies. In order to further improve the LiB technology, a number of key technological challenges regarding the performance and safety of LiBs has to be addressed. The difficulty of overcoming these challenges has lead to the search for alternative battery technologies that can replace LiBs, and some of the candi-

dates are lithium-sulfur, lithium-air, rechargeable sodium-ion batteries and rechargeable magnesium batteries (RMBs)[11–15].

Rechargeable battery chemistries based on Mg-ions are expected to achieve higher volumetric capacities than today's commercial LiBs[10], which can be attributed to the fact that the multivalent Mg-ions are able to transport twice as much charge per ion as compared to the monovalent Li-ions. More importantly, the homogeneous and dendrite-free deposition[16,17] of Mg metal allows for a pure Mg metal anode to be used in RMBs without representing a safety concern, which further increases the theoretical capacity compared to LiBs[18]. Moreover, due to the natural abundance and low cost of Mg compared to Li[19], RMB technologies are considered more scalable than LiB technologies, which is a necessity for new energy storage technologies in a global society where the demand for energy increases with an increasing population. The commercialisation of RMB technology is halted by a couple of important challenges that have to be overcome; the search for compatible electrolytes and suitable cathode materials that can host Mg-ions and operate at a suitable potential.

In the search for suitable cathode materials for RMBs, members of a recently discovered family of two-dimensional transition metal carbides, nitrides or carbonitrides, known as MXenes, have been proposed as possible candidates. Since they were first synthesised in 2011[20], the MXenes have been demonstrated to have favourable ion intercalation properties[21] and to be electrically conductive[22], making them outstanding candidates for energy storage applications. Additionally, the MXenes have been reported to perform well as sulfur hosts in Li-S batteries, owing to their high electronic conductivity and functionalized surfaces[23,24]. In this work, V_2C MXene, which has previously been shown to intercalate Li-ions[25,26], Na-ions[27] and Al-ions[28], has been investigated as a possible cathode material for RMBs. Two different designs utilizing V_2C MXene have been explored: the use of MXene as an active material in insertion cathodes and the utilization of MXene as an electrically conductive framework in conversion cathodes containing sulfur.

1.2 Aim and scope of this work

The main goal of this work was to explore the suitability of V_2C MXene as a possible constituent in both insertion and conversion cathode designs for RMBs. In order to reach this goal, the work was divided into several subgoals, where the first subgoal was the optimization of milling and etching parameters in the MXene synthesis, with regard to phase purity and a suitable narrow size distribution. Following the completion of the MXenes synthesis, the second subgoal was to evaluate the suitability of MXene as an insertion cathode for magnesium batteries, by assembling and testing V_2C MXene cathodes in coin cells with two different electrolytes. To obtain more insight into the Mg-ion intercalation process, reference cells with a Li-containing electrolyte were also tested. The third subgoal was to synthesise a V_2C MXene-sulfur composite and investigate if the V_2C MXene could enable well performing sulfur based cathodes for magnesium-sulfur batteries. Moreover, the fourth and last subgoal was to conduct post mortem characterization of the cycled cell constituents to investigate possible unwanted side reactions that may occur instead of re-

versible Mg-ion electrochemical reactions, in order to find efficient strategies for further work.

Chapter 2

Theory

2.1 Introduction to battery technology

2.1.1 Working principle

The term ”battery” describes a container, comprising one or more electrochemical cells, capable of storing energy and serving as a source of power for electrical devices. The electrochemical cells are characterized by their ability to either generate electrical energy from spontaneous electrochemical reactions or to drive non-spontaneous electrochemical reactions by application of an electrical current. One type of electrochemical cell deriving electricity from electrochemical reactions is the galvanic cell (Figure 2.1), consisting of two electrodes, the anode and the cathode, separated by an ion conducting, electronically insulating electrolyte. During discharge of the cell, the electrodes are connected through an external electrical circuit, and spontaneous reduction and oxidation reactions occur at the cathode and at the anode, respectively. The reduction and oxidation reactions arise from a difference in electrochemical potential, and causes electrons to flow from the anode to the cathode. Due to the electrolyte being electronically insulating, the electron current is forced through the external circuit, where it is able to do work. An accompanying flow of ions across the electrolyte maintains the potential difference between the electrodes, whilst simultaneously ensuring electroneutrality. The ion current continues until the spontaneous reaction at one of the electrodes has run to completion, at which point the electron current through the external circuit ceases, rendering the cell unable to continue doing work.

The electrochemical cells operating as galvanic cells are further categorized into two groups: primary cells and secondary cells. A primary cell is a galvanic cell in which the spontaneous electrochemical reactions are non-reversible, implying that the cell is non-rechargeable. Thus, a primary battery cell is designed to be used once and then discarded. A secondary cell, on the other hand, is a galvanic cell in which the spontaneous electrochemical reactions are reversible, causing the cell to be rechargeable. During the charge process, the secondary cell is operated as an electrolytic cell, in which an electrical current

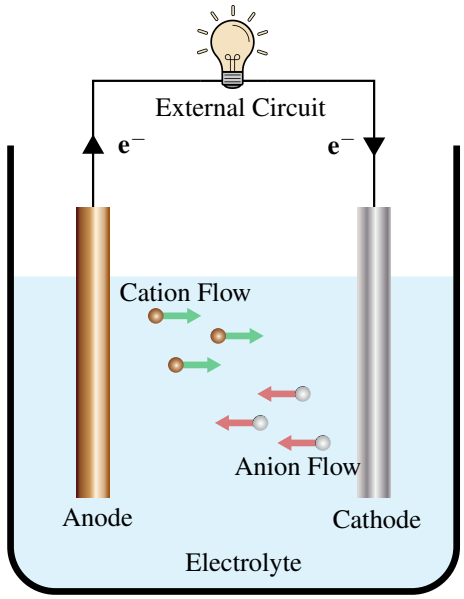

Figure 2.1: A simplified schematic of a galvanic cell, illustrating the flow of ions and electrons during discharge of the cell.

is applied in the opposite direction of the discharge current, driving the non-spontaneous electrochemical reactions and consequently charging the cell to its initial state. Thus, a secondary cell is intended for many repeated cycles of discharge and charge, before being discarded. It is worth noting that the electrode acting as the anode during discharge becomes the cathode during charge, and, conversely, the electrode acting as cathode during discharge becomes the anode during charge. In order to avoid confusion, the convention for galvanic cells will be used, i.e. the anode and the cathode are the electrodes being oxidized and reduced during discharge, respectively.

The rather simplistic design of the basic galvanic cell does not quite depict the complexity of the modern-day battery systems, as these often contain additional components that are necessary for the systems to fulfil application-specific requirements. In systems utilizing a liquid electrolyte, an essential component is the electrolyte-permeable separator, which is tasked with preventing electronic contact between the electrodes, whilst simultaneously allowing an efficient flow of ions across the cell[29]. The separator contributes to maximizing the energy density of the cell, as it allows for the distance between the electrodes to be reduced, thus minimizing the total cell volume. Additionally, decreasing the distance between the electrodes reduces the internal resistance of the cell, which in turn reduces the voltage drop between the electrodes during cell operation[30]. There are several important parameters that determine the properties of the separator, e.g. thickness, permeability, porosity, wettability and chemical stability, and each of these parameters must be optimized to fit the requirements for a given application[29].

The electrodes that are used in modern battery systems may comprise a combination of several different materials, where each material has a specific task to fulfil in the electrode. The part of the electrode undergoing electrochemical reactions during cell operation is called the active material, and its main purpose is to host the charge carrying ions. In addition to the active material, the electrodes usually contain a current collector, which purpose is to transfer electrons between the electrode and the electrical circuit. The current collector is especially important for electrodes in which the active material has a low electrical conductivity, as it reduces the path that the electrons have to travel in the active material, thus increasing the overall conductivity of the electrode. Additionally, in electrodes where the active material is not able to form free-standing films and thereby support itself structurally, the current collector functions as a substrate that the active material can be deposited onto. Thin metal foils are commonly used as current collectors, due to their structural integrity, high conductivities and good corrosion stabilities[31].

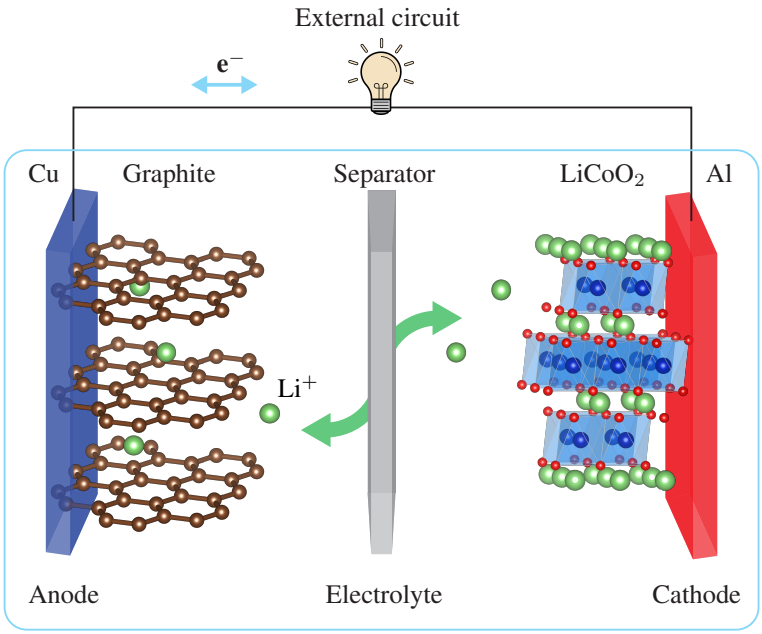

Figure 2.2: A schematic representation of a modern Li-ion battery, utilizing an anode consisting of graphite on a copper current collector and a cathode consisting of $LiCoO_2$ on an aluminium current collector. The separator is semi-permeable, allowing the Li-ions to flow across, while the electrons are forced through the external circuit. Adapted from[1].

The $Li_{1-x}CoO_2$/C LiB (Figure 2.2), first assembled by Yoshino in 1985[32], is a good example of a modern battery system incorporating active materials, current collectors, an electrolyte and a separator. When such a system is assembled, each of the components

have to be carefully selected, in order to guarantee compatibility between all the different constituents of the cell. An incompatibility between two or more components could hinder the cell from operating properly, and in some cases even lead to degradation of certain cell constituents, resulting in cell failure. A relevant example of component incompatibility related to LiB technology is the use of pure Li metal as the anode material. Despite being considered an ideal candidate due to its high theoretical capacity, low density and favourable electrochemical potential, the Li metal anodes suffer from uncontrollable dendritic Li growth during operation with today's electrolytes, which poses a safety risk as the dendrites may pierce through the separator and thus short-circuit the cell[33]. This example emphasizes the complexity of modern-day battery systems, and further illustrates the challenging nature of developing new systems or improving on already existing battery designs.

2.1.2 Battery performance parameters

Rechargeable batteries can be described by a number of critical performance parameters, and which ones that are most important is highly dependent upon the intended application. The most common performance parameters are[30]:

- Volumetric and gravimetric energy density
- Specific power and power density
- Cycle life
- Shelf life
- Efficiency
- Cost
- Safety
- Environmental friendliness

The energy content of a battery is commonly expressed either as the volumetric energy density, which is the stored energy per unit volume (Wh dm^{-3}), or as the gravimetric (specific) energy density, which is the stored energy per unit mass (Wh kg^{-1}). The volumetric and gravimetric energy densities are important parameters for non-stationary applications, e.g. smartphones, cameras and electric vehicles, where weight and size are limiting factors. Furthermore, for some applications the power that is available from the battery, expressed in watts (W), may be of greater importance than the amount of stored energy. Similarly to the terms for stored energy, the power is commonly described relative to the mass or the volume of the battery. Thus, the specific power is the power output per unit mass (W kg^{-1}), and the power density is the power output per unit volume (W dm^{-3}).

The battery cycle life describes the number of charge-discharge cycles a battery can sustain, before reaching a point at which the battery no longer performs adequately. A common definition of this endpoint is the number of cycles until the retained capacity of the

battery is reduced to 80% of the initial value. The shelf life of a battery describes the time a battery can be stored before it becomes unfit for use. Additionally, the production cost, safety and environmental friendliness are parameters that are always important, as they greatly influence the commercialization potential of the battery system in question.

The open-circuit voltage, V_{OC}, of a battery cell is the voltage across the cell terminals when there is no net current. This voltage is determined by the difference in electrochemical potential between the two electrodes, and is given by

$$V_{\mathrm{OC}} = \frac{\mu_{\mathrm{A}} - \mu_{\mathrm{C}}}{e}, \tag{2.1}$$

where μ_{A} and μ_{C} are the electrochemical potentials of the anode and the cathode, respectively, and e is the elementary charge[1]. However, when there is a current flow through the cell, the operating voltage will differ from the open-circuit voltage, due to the system being forced away from equilibrium conditions. The shift in cell potential away from the equilibrium value is known as the overpotential, η, and is a result of the internal impedance of the battery. The impedance, comprising polarization losses at the electrodes and ohmic losses in the active material, current collectors and electrolyte[30], varies as a function of the state of charge, q, where $0 < q < 100\%$. The effect of the internal impedance on the operating voltage of the cell is seen as a decrease in the output voltage, V_{dis}, during discharge, and as an increase in the voltage needed to reverse the electrochemical reactions, V_{ch}, during charge. The voltages are given by

$$V_{\mathrm{dis}} = V_{\mathrm{OC}} - \eta(q, I_{\mathrm{dis}}), \tag{2.2}$$

and

$$V_{\mathrm{ch}} = V_{\mathrm{OC}} + \eta(q, I_{\mathrm{ch}}), \tag{2.3}$$

where I_{dis} and I_{ch} are the currents during discharge and charge, respectively[1].

The capacity of a battery, $Q(I)$, either expressed as the gravimetric capacity (Ah kg^{-1}) or as the volumetric capacity (Ah dm^{-3}), is the total amount of charge transferred by the current $I = \frac{\mathrm{d}q}{\mathrm{d}t}$ during charge or discharge. The capacity is dependent on the current, because the flow of ions across the interface between the electrode and the electrolyte becomes diffusion-limited at high currents. However, capacity loss related to high rates of charge or discharge is partially reversible. Depending on the material in question, some or all of the lost capacity is regained when cycled at lower current rates, as the flow of ions is no longer diffusion-limited. On the other hand, capacity loss caused by changes in electrode volume, unwanted electrochemical reactions between the electrolyte and the electrodes or decomposition of one or both electrodes is irreversible[1]. In order to determine the capacity of a given battery, it is convenient to measure the total time, Δt, it takes to completely

discharge or charge the cell at a constant current, $I = \frac{\mathrm{d}q}{\mathrm{d}t}$. The capacity is then given by[1]

$$Q(I) = \int_0^{\Delta t} I \mathrm{d}t \tag{2.4}$$

$$= \int_0^{Q} \mathrm{d}q. \tag{2.5}$$

The theoretical specific capacity of a battery, Q_{th}, expressed in mAh g^{-1}, is given by

$$Q_{\text{th}} = \frac{C_{\text{A}} C_{\text{C}}}{C_{\text{A}} + C_{\text{C}}}, \tag{2.6}$$

where C_{A} and C_{C} are the specific capacities of the anode and the cathode, respectively[34]. It is evident from the expression that the capacity of a battery is determined by the specific capacities of the two electrodes, and that the electrode with the lowest capacity is the limiting factor. This implies that a large difference in the specific capacities of the electrodes is undesirable. The theoretical specific capacity of one electrode is given by

$$C_{\text{sp}} = \frac{nF}{M_{\text{w}}}, \tag{2.7}$$

where n is the number of electrons taking part in the electrochemical reaction at the electrode, F is the Faraday constant and M_{w} is the atomic or molecular mass of the reacting electrode material[35]. The volumetric capacity of one electrode can be obtained by simply multiplying the specific capacity by the density, ρ (g $\text{cm}^{-}3$), of the reacting compound

$$C_{\text{vol}} = \frac{nF}{M_{\text{w}}} \times \rho. \tag{2.8}$$

Similarly as for the battery capacity, the total amount of energy, E, that can be recovered from a fully charged cell is dependent on the discharge current. By determining the total discharge time at a given current, the energy can be calculated from

$$E(I) = \int_0^{\Delta t} IV(t)\mathrm{d}t \tag{2.9}$$

$$= \int_0^{Q} V(q)\mathrm{d}q, \tag{2.10}$$

where $V(t)$ is the time dependent voltage, $V(q)$ is the voltage as a function of the state of charge[1]. Furthermore, the amount of energy utilized during discharge is always smaller than the amount used to fully charge the cell. The energy efficiency (EE) of the battery, expressed in percent, is defined as the ratio between the utilized energy and the energy needed during charging:

$$\mathrm{EE} = 100 \times \frac{\int_0^{Q_{\mathrm{dis}}} V_{\mathrm{dis}}(q)\mathrm{d}q}{\int_0^{Q_{\mathrm{ch}}} V_{\mathrm{ch}}(q)\mathrm{d}q}. \tag{2.11}$$

The energy efficiency can be a crucial parameter, especially for applications where the electricity cost is a major part of the total operating cost, as the energy that is lost during cycling represents an economic loss. On the other hand, to better illustrate the reversibility of the electrochemical reactions, the efficiency in terms of capacity fade is more important, as it describes the capacity balance between charge and discharge processes. This efficiency, denoted as the Coloumbic efficiency (CE), is given by

$$\mathrm{CE} = 100 \times \frac{Q_{\mathrm{dis}}}{Q_{\mathrm{ch}}}. \tag{2.12}$$

For fully reversible processes, the Coloumbic efficiency will be 100%.

2.2 Rechargeable magnesium batteries

2.2.1 Introduction

RMBs are made up of the same general components as the LiBs, and operates by the same electrochemical principles as the Li-based cells. However, the fundamental difference between these two technologies is the ions responsible for the charge transport within the cell, and while LiBs utilize Li-ions for charge transport, the RMBs rely on Mg-ions instead. The research of RMBs as a competitive battery technology is motivated by the following three main aspects

1. The multivalency of the Mg-ion
2. The possibility of using a Mg metal anode
3. The abundance and low cost of Mg

The Mg-ion, Mg^{2+}, is a divalent cation, while the Li-ion, Li^{+}, is a monovalent cation, implying that the Mg-ion is able to transport twice as much charge as the Li-ion. Furthermore, the insertion of a single Mg-ion into one of the electrodes of a RMB will ideally result in a two-electron reduction reaction, whilst the equivalent reaction for a Li-ion involves only one electron. Due to the ionic radius of Mg^{2+} (0.86 Å) being rather similar to the one of Li^{+} (0.90 Å), the theoretical volumetric capacity in identical hosts is doubled for Mg-ions compared to Li-ions[10]. However, as the molar mass of the Mg-ion is about four times the molar mass of the Li-ion, the theoretical gravimetric capacity of a battery utilizing Mg-ions is only about half of what is possible for a battery using Li-ions.

While the Li metal anodes in LiBs are plagued by dendrite formation during cycling, the reversible electrochemical stripping and deposition of Mg on Mg metal anodes has been shown to occur without any significant dendrite formation for several different electrolytes[16,17]. As a result, this alleviates the safety concerns regarding its application as an anode material in RMBs. Additionally, the volumetric and specific capacities of Mg metal are 3832 mAh cm^{-3} and 2205 mAh g^{-1}, respectively, and both these values are considerably higher than the corresponding values of 837 mAh cm^{-3} and 372 mAh g^{-1} for the graphite anode commonly used in LiBs[18]. Furthermore, the Mg metal has a low reduction potential, and in combination with the high theoretical capacity this forms the basis for energy dense batteries. Another aspect making Mg metal an excellent candidate for the anode material in RMBs, is its high electronic conductivity, which eliminates the need for an additional current collector in the anode design, thus reducing the total weight and cost of the battery.

Mg is estimated to be about 1000 times more abundant in the earth's crust than lithium, implying that Mg-based batteries may possibly be a cheaper alternative than the conventional LiBs. The implication is strengthened by taking into account the fact that the annual production of Mg (by mass) is more than 250 times that of Li, and additionally, that the

price of Li is approximately ten times higher than that of Mg[19]. Thus, RMB technology may represent a more scalable and cheaper alternative to LiB technology.

The state-of-the-art RMB technology is represented by the first practical prototype developed by Aurbach et al. in 2000[36], consisting of a Mg metal anode, an electrolyte based on Mg organohaloaluminate salts dissolved in tetrahydrofuran (THF), and a $Mg_xMo_6S_8$ ($0 < x < 2$), Chevrel phase cathode. The prototype system exhibited a cycle life of more than 2000 cycles, with a fade in capacity of less than 15%. However, the specific capacity was only about 70 mAh g^{-1} at an operating voltage of approximately 1.1 V. Since then, only minor improvements of the RMB prototype have been reported[16], although several large corporations, such as Sony, LG and Toyota, have made efforts towards developing new RMB technologies in recent years[37,38].

In order to establish a competitive RMB technology, there is a couple of challenges related to the electrochemistry of Mg that have to be overcome. Firstly, there is a need for electrochemically stable electrolytes that can easily dissolve Mg-salts and transport the ions across the cell. Secondly, cathode materials allowing fast and reversible Mg insertion at decent operating potentials and at ambient temperatures must be developed[39].

2.2.2 Anode

Due to its high capacity and favourably low electrochemical potential, Mg metal has been considered the anode material of choice ever since the demonstration of the first prototype RMB system. However, the high activity of the Mg metal may lead to undesirable reactions upon contact between the anode and certain electrolytes, resulting in the formation of a solid electrolyte interface (SEI). This interface can block the diffusion of the Mg-ions, and thereby hinder the electrochemical deposition and stripping of Mg from taking place on the anode. Therefore, the use of Mg metal as anode limits the choice of electrolyte, and imposes additional challenges on the development of new electrolytes.[18]

In order to avoid the limitations of the electrolytes caused by the reactivity of the Mg metal, insertion type anodes have been proposed as alternatives to the Mg metal anode. Arthur et al.[40] demonstrated reversible electrochemical insertion and extraction of Mg-ions in $Bi_{0.88}Sb_{0.12}$ and $Bi_{0.55}Sb_{0.45}$ alloy insertion anodes, where $Bi_{0.88}Sb_{0.12}$ displayed the highest initial specific capacity of 298 mAh g^{-1}. However, the capacity was reduced to 215 mAh g^{-1} after only 100 cycles, due to pulverization of the anode as a result of volume expansion during operation. Furthermore, other research groups have reported Li_3VO_4 and $Li_4Ti_5O_{12}$ as possible materials for insertion anodes, displaying specific capacities of 318 mAh g^{-1} and 175 mAh g^{-1}, respectively[41,42]. In spite of the decent capacities of these materials, the reported results also uncover challenges related to low coulombic efficiencies and strongly decreasing capacities with increasing current rates, implying sluggish diffusion kinetics of Mg-ions in the host materials[18]. Thus, despite circumventing the issues related to the formation of an SEI layer, the insertion anodes display severely limited performances compared to Mg metal anodes. As a result, the majority of RMB related research is therefore focused towards finding electrolytes that are compatible with the Mg

metal rather than developing new anode materials.

2.2.3 Electrolyte

The research and development of suitable electrolytes for RMBs is a challenging endeavour, as the battery system imposes a number of demanding requirements on the electrolyte. The most crucial requirements are summarized below[18]

- High ionic conductivity
- High Mg-ion transference number
- Electronically insulating
- Electrochemically stable
- Chemically stable
- Non-corrosive
- Acceptable safety properties
- Low cost

As the main task of the electrolyte is to ensure efficient transport of ions across the cell, a high ionic conductivity is an absolute requirement. More specific, the ionic conductivity must be sufficiently high for all practical current rates, in order to avoid that the ion transport becomes a limiting factor for the performance of the battery. Additionally, the Mg-ion transference number of the electrolyte, stating the fraction of the ionic conductivity that is attributed to the Mg-ions, is desired to be high. Another requirement that is absolute, is that the electrolyte must be electronically insulating, as to guarantee that the electrons can not traverse the cell internally, but is instead forced through the external circuit.

The electrochemical stability of an electrolyte is determined by its electrochemical potential window, defined by the energy gap between the lowest unoccupied and highest occupied molecular orbitals (LUMO and HOMO) of a liquid electrolyte or the bottom of the conduction band and top of the valence band of a solid electrolyte. A stable configuration, illustrated for a liquid electrolyte in figure 2.3, is achieved when the HOMO level of the electrolyte is below the electrochemical potential of the cathode, while the LUMO level of the electrolyte is above the electrochemical potential of the anode. In general, an μ_{A} above the LUMO level would lead to reduction of the electrolyte, and similarly, an μ_{C} below the HOMO level would result in the electrolyte being oxidized. However, the formation of an SEI layer can block these reactions and, thereby, hinder any further decomposition of the electrolyte, which is the case for today's LiBs[1].

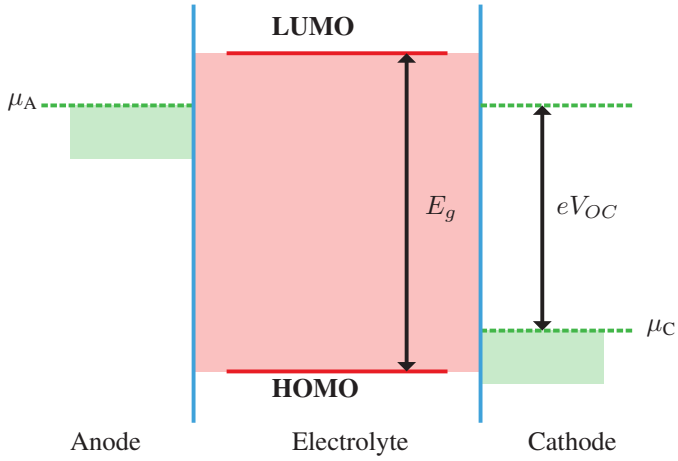

Figure 2.3: The electrochemical stability window, E_g, is given by the difference between the HOMO and LUMO levels of the electrolyte. The open-circuit voltage, V_{OC}, is given by the difference between the electrochemical potential of the anode, μ_A, and the cathode, μ_A. Adapted from[1].

The electrolyte is expected to perform consistently over a large number of cycles and range of temperatures, and is therefore required to be chemically stable. The chemical stability implies that the electrolyte is able to maintain its properties throughout the lifetime of the battery, without decomposing in any way. Additionally, the electrolyte is required to be non-corrosive, in order to avoid degradation of the other cell components, including spacers, current collectors, the separator and the cell housing.

The safety properties of an electrolyte, including high thermal stability, low volatility, low flammability, low toxicity and low reactivity with ambient air, are important factors in the development of new RMB technologies, as a failure to meet these requirements would pose a safety risk. Furthermore, the production cost of the electrolyte is desired to be as low as possible, as this increases the commercialization potential of the battery system as a whole.

Preceding the demonstration of a working RMB prototype by Aurbach et al. in 2000, Gregory et al. showed dissolution and deposition of Mg from solutions of organomagnesium compounds in ethers or tertiary amines[43]. These electrolytes were characterized by low coulombic efficiency and anodic stability, and in working towards the realization of the first RMB prototype, Aurbach and co-workers developed improved electrolytes based on Mg organohaloaluminate salts dissolved in THF or polyethers of the glyme family[36]. The improved electrolytes displayed reversible electrochemical deposition and dissolution of Mg, with a Coloumbic efficiency close to 100%, and an electrochemical stability window of more than 2.5 V. In more recent studies, electrolytes based on either organomagnesium chloride complexes, such as the "dichloro complex" (DCC) and the "all phenyl complex" (APC), or inorganic magnesium aluminium chloride complexes (MACC) have been sug-

gested for use in RMB systems, as they exhibit anodic stability around 3.1 V and a high degree of reversible Mg deposition and stripping[44–47]. However, these electrolytes contain chloride and are known to corrode various cell components, including stainless steel housings and a number of common current collectors at potentials above 2.2 V vs Mg metal[15,38]. Additionally, the use of THF as solvent in some of these electrolytes is undesirable, as it is a highly volatile and flammable compound.

In an attempt to overcome the challenges related to corrosion of cell constituents, Mohtadi[48], Carter[49], Tutusaus[50], and colleagues at Toyota R & D developed a series of halogen-free electrolytes, e.g. Mg boron-clusters and carboranes. These electrolytes possess exceptionally high anodic stabilities of 3.8-4.0 V and are less corrosive towards cell constituents than their chloride-containing predecessors. Another electrolyte that has gained a lot of interest over the last couple of years is Mg bis(trifluoromethane sulfonyl)imide ($Mg(TFSI)_2$) dissolved in glyme-based solvents, which is characterized by excellent anodic stability exceeding 4.0 V, reduced corrosive behaviour toward the current collectors, low volatility and high solvating power[51]. Furthermore, a group of room temperature ionic liquids (ILs) based on imidazolium and pyrrolidinium have been proposed as possible electrolytes for RMBs. One research group has reported reversible deposition and dissolution of Mg and a large electrochemical stability window for these ILs[52], whilst two other groups were unable to reproduce this result[53,54].

As an alternative to the liquid electrolytes, Kumar et al.[55] reported on a solid state gel polymer electrolyte consisting of poly(methylmethacrylate) and magnesium triflate, which was demonstrated to have a wide electrochemical stability window and a promising ionic conductivity. Moreover, a solid polymer electrolyte consisting of a poly(ethylene oxide)-ploy(vinyl pyrrolidone) blend and a $Mg(NO_3)_2$ salt have also been proposed for the use in solid state RMBs, due to its high anodic stability of 4 V and favourable ionic conductivity[56]. All in all, a number of interesting electrolytes have emerged over the last couple of years, yet, more research is needed to further improve the performance of the RMB electrolytes.

2.2.4 Cathode

Analogous to the development of suitable electrolytes, the search for suitable cathode materials for RMB technologies is also a challenging task, as the battery system imposes several stringent requirements on the cathode. The most important requirements are listed below

- High reversible gravimetric and volumetric capacities
- High operating potential vs the anode material
- Fast Mg-ion diffusion
- High electronic conductivity
- Chemical stability

- Non-toxic
- Low cost
- Low environmental impact

The main task of the cathode is to host Mg-ions in such a manner that they can be easily incorporated and retrieved during cell operation. The incorporation of ions into the cathode follow one of three possible reaction mechanisms: insertion, alloying or conversion. These reaction mechanisms are illustrated for the case of LiBs in figure 2.4, with the concepts being directly transferable to RMBs. Cathodes based on alloying and conversion reactions typically display higher capacities than insertion cathodes, but suffer from large volume changes during operation, resulting in severely reduced cycle lifetime. Furthermore, the fundamental challenge to overcome in the development of new RMB cathodes, is the slow diffusion of Mg-ions within the host material, caused by a combination of attractive interactions between the divalent ions and the host, and repulsive interactions between the ions themselves[18].

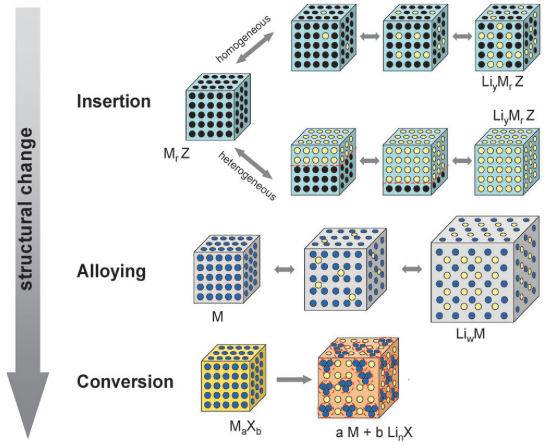

Figure 2.4: Schematic illustration of the different reaction mechanisms observed in electrode materials for LiBs. Black circles: voids in the crystal structure, blue circles: metal, yellow circles: lithium. Adapted from ref.[57]

The search for suitable cathode materials for RMBs began in the 1980s, when Gregory et al. evaluated a number of transition metal oxides, sulphides and borides as possible candidates[43]. However, the first real breakthrough regarding RMB cathode materials came in 2000, when Aurbach et al.[36] used a $Mg_xMo_6S_8$, Chevrel phase cathode in their demonstration of the first viable RMB prototype. Although the cathode displayed good cyclic stability, the operating voltage of 1.1 V and specific capacity of only 70 mAh g^{-1} excluded it as a candidate for commercial applications. The limited capacity of the Chevrel phase cathode is partially explained by Mg-ion trapping in the host material, resulting in

incomplete extraction of the intercalated specie[58–61].

The $Mg_xMo_6S_8$ Chevrel phase structure is part of a larger family of materials known as the chalcogenides. Several transition metal sulphides and selenides from this family have been proposed as possible candidates for RMB cathodes, due to their high Mg-ion mobilities, which in turn is attributed to their highly polarizable anion frameworks[38,58,62]. Currently, TiS_2 is considered the most promising candidate from this family of materials, with a reported stable capacity of 115 mAh g^{-1}[63]. However, like many of the other chalcogenide materials, TiS_2 displays a low operating voltage, resulting in limited energy density.

In an attempt to identify cathode materials with higher operating voltages and capacities, a number of transition metal oxides, including MnO_2[64,65] and V_2O_5[66,67], have been investigated, as the oxides are known to have higher intercalation voltages than the sulphides and selenides[68]. The MnO_2 and V_2O_5 materials exhibited operating voltages of more than 1.5 V and specific capacities higher than 150 mAh g^{-1}. Yet, varying cyclic stabilities were reported for the different materials, and in some of the systems prolonged cycling was associated with a large fade in capacity[65].

A conversion cathode based on sulphur has been proposed as a promising alternative to intercalation based cathodes, due to its high theoretical capacity of 1671 mAh g^{-1} and natural abundance. The conversion cathode design is based on the reduction of solid cyclo-S_8 to solid MgS_2 over a number of steps[69]. In the first step (equation 2.13), cyclo-S_8 is reduced to S_8^{-2} by the formation of polysulfide MgS_8 in the liquid state. Thereafter, the MgS_8 is further reduced to polysulfide MgS_6, and then subsequently to polysulfide MgS_4. In the next step (equation 2.14), the liquid MgS_4 polysulfide is reduced to solid MgS_2. In the final step (equation 2.15), the solid MgS_2 is further reduced to MgS. Furthermore, Vinayan et al. reported a reversible capacity of 448 mAh g^{-1} in a Mg/S system, with a capacity retention of 236 mAh g^{-1} after 50 cycles[69]. Although these are promising results, there are still several important challenges limiting the development of RMBs utilizing sulphur cathodes. One of these challenges is related to the strong electrophilic nature of sulphur, as this limits the choice of suitable electrolyte to one that is non-nucleophilic. Additionally, challenges such as polarization effects during charging, low cyclic stability, initial capacity fading, electrically insulating nature of sulphur and polysulphide dissolution are all crucial to solve in the development of sulphur cathodes for RMBs.

$$S_8 + 4e^- + 2Mg^{2+} \rightarrow 2MgS_4 \tag{2.13}$$

$$MgS_4 + 2e^- + Mg^{2+} \rightarrow 2MgS_2 \tag{2.14}$$

$$MgS_2 + 2e^- + Mg^{2+} \rightarrow 2MgS \tag{2.15}$$

The search for suitable cathode materials with the ability to host Mg-ions has uncovered several promising candidates along the way, but so far none of these have proven viable for commercial applications. More recently, a new family of materials known as MXenes have been proposed as possible candidates for RMB cathodes[21], and these materials will be further discussed in the following section.

2.3 MXenes

2.3.1 Background

MXenes are a family of two-dimensional early transition metal carbides, nitrides and carbonitrides, that are usually synthesized from so-called MAX phases. The name "MAX phases" is derived from their general chemical formula $M_{n+1}AX_n$ ($n = 1, 2$ or 3), where M represents a transition metal, A represents a group 13 or group 14 element, most commonly aluminium or silicon, and X represents carbon and/or nitrogen. These compounds have a layered hexagonal structure, where the $M_{n+1}X_n$ layers are separated by monolayers of the A-element[70], as illustrated in figure 2.5.

In 2011, while researching the application of MAX phase compounds as possible anodes in LiBs, M. Naguib decided to etch the MAX phase compounds with a solution of aqueous hydrofluoric acid (HF), with the purpose of modifying the material and improving its Li diffusion properties. This lead to the discovery of MXenes, as the etching of Ti_3AlC_2 resulted in the selective removal of Al from the MAX phase structure, leaving only the Ti_3C_2 MXene sheets[20,71]. The name "MXene" was appropriately chosen based on the fact that only the $M_{n+1}X_n$ layers remained after the etching process, and that there is a resemblance between the MXenes and the well known two-dimensional material graphene. Currently, there are more than 70 known MAX phases[72], and around 20 different MXenes that have been successfully synthesized[73].

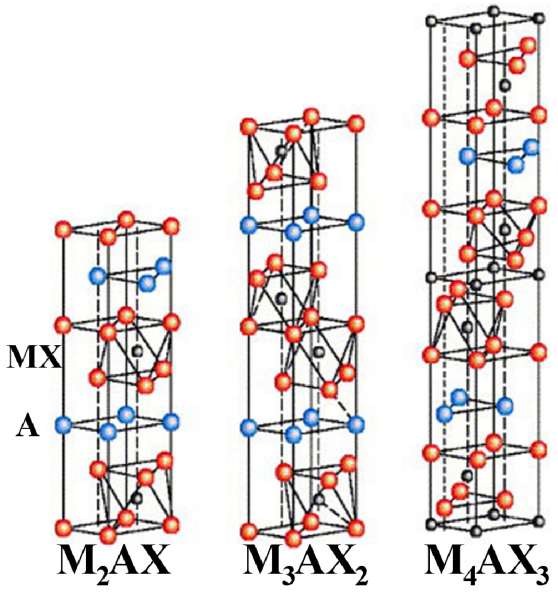

Figure 2.5: Illustration of the different MAX phase structures. Adapted from ref. [74]

2.3.2 Synthesis

The established route for the synthesis of MXenes (figure 2.6) is by chemical etching of the MAX phase in aqueous HF or HF-forming etchants, e.g. HCl and LiF[22,75]. Importantly, this etching process results in functionalized surfaces that are terminated by -O, -F and -OH groups, bound to the transition metal atoms. These surface termination groups can be explicitly denoted as T_x in the MXene formula, i.e. $M_{n+1}X_nT_x$.

The chemical reactions taking place during the etching of a MAX phase are proposed to be[20,76]

$$M_{n+1}AlX_n + 3HF \rightarrow M_{n+1}X_n + AlF_3 + 1.5H_2 \tag{2.16}$$

$$M_{n+1}X_n + 2H_2O \rightarrow M_{n+1}X_n(OH)_2 + H_2 \tag{2.17}$$

$$M_{n+1}X_n + H_2O \rightarrow M_{n+1}X_nO + H_2 \tag{2.18}$$

$$M_{n+1}X_n + 2HF \rightarrow M_{n+1}X_nF_2 + H_2 \tag{2.19}$$

where equation (2.16) describes the process of removing the Al (A-element) and equation (2.17), (2.18) and (2.19) describes the formation of the different surface termination groups. Theoretical calculations and experimental reports have shown that the surface termination groups greatly influence the properties of the MXenes[77–80], implying that controlling the composition and distribution of termination groups may be crucial for certain applications. For the remainder of this report the $M_{n+1}X_n$ notation will be used to describe the MXenes, and unless otherwise stated the presence of termination groups is implied.

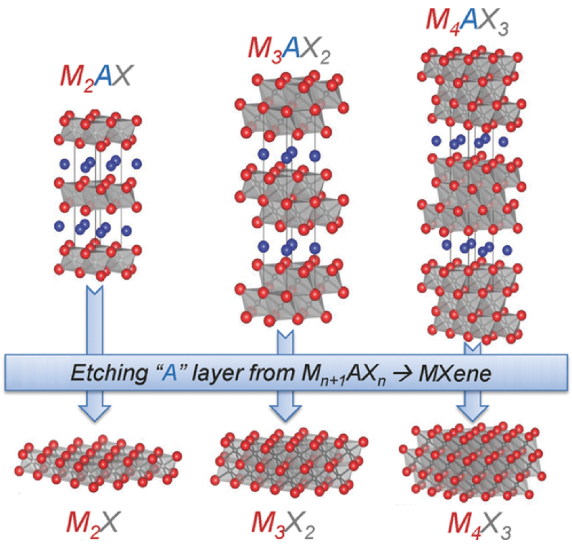

Figure 2.6: Overview of the structural transformation upon etching from MAX phase to MXene. Adapted from ref. [75]

The etching of MAX phases to produce MXenes require strict control of critical parameters such as temperature, etching time and HF concentration[75,81]. The optimal etching conditions for the MAX phases containing different transition metals have been shown to vary greatly, depending on the atomic bonding, particle size and structure. In general, increasing the atomic number of the transition metal requires longer etching time and higher HF concentration, due to increasing bond energies for the M-A bonds[75]. Additionally, when n in the MAX phase formula increases, a stronger etching regime is needed to completely convert the MAX phase to MXene. Moreover, the particle size is an important parameter in determining the etching regime required to completely exfoliate the MXene transition metal sheets[25], as the lateral dimension of the particles determine the diffusion path the etchant molecules must travel in order to reach the innermost Al (A-element) atoms. Thus, the particle size determines the diffusion time required to complete the etching process. The etchant concentration will also greatly affect the etching time, and it has been shown that harsh etching parameters, i.e. high HF concentration and long etching time, may lead to complete dissolution of the MAX phase particles[82]. Similarly, if the etching time is too short or the etchant concentration is too low, the exfoliation of the MXene particles may be incomplete. Moreover, the temperature of the etching solution has been shown to affect the time needed for complete exfoliation of the MAX phase particles, where increased temperature leads to a decrease in the required etching duration[81].

Following the completion of the exfoliation process, the MXene sheets stick together due to attractive Van der Waals forces, resulting in stacked MXene particles termed multilayered (ml-) MXenes. For some applications it may be more convenient with single- (sl-) or fewlayered (fl-) MXenes, and this can be achieved by an additional two-step process (figure 2.7). In the first step of the process, the multilayered MXene structure is preinter-

calated with either cations[83] or organic molecules such as TBAOH[81], leading to swelling of the structure and weakening of the attractive Van der Waals forces between the MXene sheets. In the following step, sonication or shaking of a dispersion containing the MXene particles is utilized to delaminate the ml-MXene into sl- and fl-MXene[84].

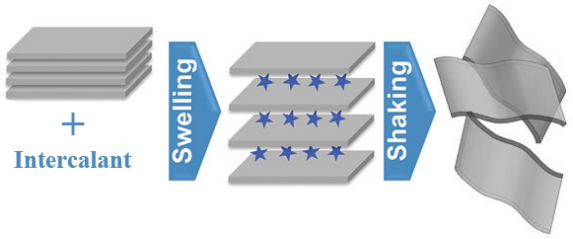

Figure 2.7: Schematic overview of the delamination process of ml-MXene to fl- and sl-MXene. Adapted from ref.[84]

2.3.3 Intercalation properties

In recent years, the MXenes have received considerable attention as possible materials for energy storage applications, due to their outstanding combination of properties such as high electrical and thermal conductivity, hydrophilic nature, excellent thermal stability, easily tunable structure, high surface area, great oxidation resistance and capability to host a range of intercalants[81,83,85–90], including Mg-ions. In addition to the previously discussed surface termination groups, the interlayer distance between the two dimensional transition metal sheets is also known to greatly influence the properties of the MXenes. Thus, by controlling the surface terminations and the interlayer distance, the ion hosting properties of the MXenes can be finely tuned[72,80,91]. As briefly mentioned earlier, it is possible to adjust the interlayer distance of the ml-MXene by preintercalation of cations or organic molecules. Additionally, due to the hydrophilic nature of the MXene sheets, water molecules have been demonstrated to easily intercalate into the structure[25,92], resulting in an increase of the interlayer distance of the MXene. Furthermore, the formation of the surface termination groups is generally dependant upon the etchant concentration, and increasing the HF concentration leads to an increase in the amount of F-terminations that are formed[80]. Post-synthesis treatments such as annealing[93], chemical treatment in alkaline solutions[80,94] and delamination[84] have been demonstrated to reduce the amount of F-terminations, in favour of O- and OH-terminations, which could be critical for the obtained intercalation properties.

The current understanding of the Mg-ion intercalation sites in MXene materials is based primarily on theoretical predictions[21,95], although recent experimental reports have made efforts towards investigating the matter as well[96]. The cation intercalation sites in the MXene structure have been predicted by density functional theory calculations[21], and the suggested sites are illustrated in figure 2.8. Moreover, the calculated results indicate that oxygen terminations are more favourable than the alternative termination groups, with re-

spect to achievable capacity and rate capability[95].

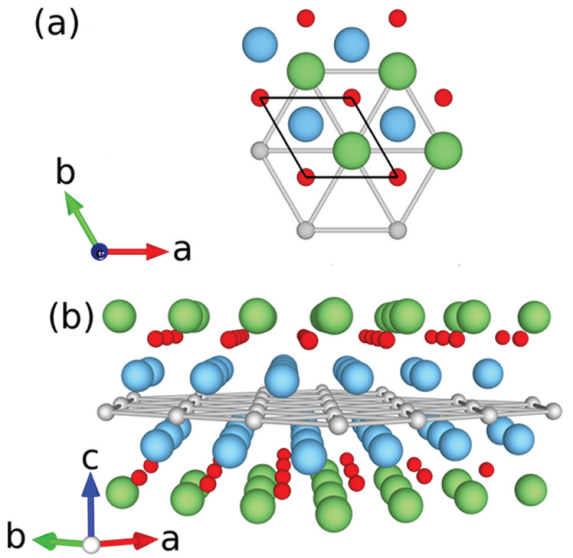

Figure 2.8: Illustration of the predicted cation intercalation sites in the MXene structure: (a) view down the c-axis and (b) side view. Sphere colour key: green - intercalant, red - functional group, blue - transition metal, gray - carbon. The unit cell is outlined in black in (a). Adapted from ref. [21]

2.3.4 MXene-sulphur conversion cathodes

In order to address the challenges hindering the use of sulphur conversion cathodes in RMBs, a composite consisting of nanodispersed active sulphur in a suitable carbon host matrix has been proposed as a possible conversion cathode design[69]. MXenes are suggested as excellent candidates for the matrix in sulfur cathodes for lithium-sulfur batteries, due to their high electrical conductivity and self-functionalized surfaces[23,97]. The hydrophilic surfaces of MXenes are predicted to strongly bind polysulfides via hydrophilic surface interactions, which in turn counters the challenge of capacity degradation due to polysulphide dissolution in the electrolyte, thus extending the cycle life. Although there are currently no experimental reports on MXene-sulphur composites in RMBs, several research groups have observed discharge capacities of more than 1200 mAh g^{-1} and high cyclic stability for Ti_2C-S[23] and Ti_3C_2-S[24] composites in lithium-sulfur batteries, suggesting that MXene-sulphur composites may also be suitable as conversion cathodes in RMBs.

2.3.5 V_2C MXene

The V_2C MXene is synthesized from the V_2AlC MAX phase, which belongs to the group of MAX phase compounds with the thinnest transition metal layers, i.e. $n = 1$ in the general MAX phase formula. V_2AlC has a layered hexagonal structure with lattice parameters $a = 2.9107$ Å and $c = 13.101$ Å, belonging to the $P6_3/mmc$ space group[98]. The transition metal layers consist of hexagonally close packed vanadium atoms, with interstitial carbon atoms in the octahedral sites. The unit cell and layered structure of the V_2AlC MAX phase are illustrated in figure 2.9 and 2.10, respectively. As mentioned earlier, the MXene particles retain the layered structured of the MAX phase after removal of the Al atoms, although with an increased interlayer distance. Generally, the conversion from V_2AlC MAX phase to V_2C MXene can be confirmed by X-ray diffraction (XRD), where a downward shift of the (002) peak, corresponding to an increase in the interlayer distance, indicates the formation of MXene.

In previous reports on V_2C MXene, exfoliation of the parent MAX phase has been achieved by utilizing HF concentrations as high as 50% with etching durations between 8 and 96 h[25,27,28,84]. The large span in etching time is attributed to varying MAX phase particle size, as some of the groups included milling of the MAX phase as an extra step prior to etching[25]. In comparison to the more researched Ti_2C MXene, the etching time of 96 h utilized for V_2C MXene synthesis is quite high, which can be explained by the difference in bond energy between the V-Al bonds and the Ti-Al bonds (1.09 eV vs 0.98 eV, respectively) in the respective parent MAX phases[99]. Furthermore, V_2C MXene has previously been demonstrated to intercalate Li-ions[25,26], Na-ions[27] and Al-ions[28], making it a promising candidate for hosting Mg-ions as well. It is also worth noting that there exist no previous reports on V_2C-S composites as cathode material for RMBs or LiBs.

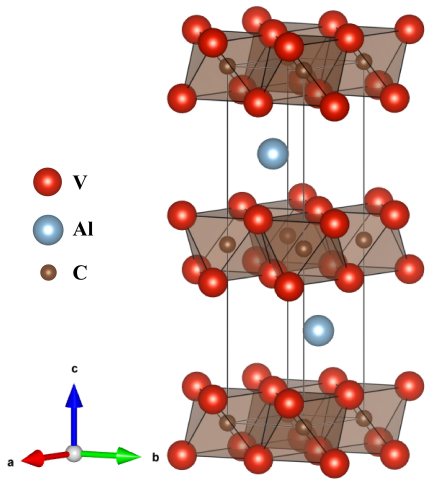

Figure 2.9: Unit cell for the V_2AlC MAX phase. Figure drawn in VESTA[100]

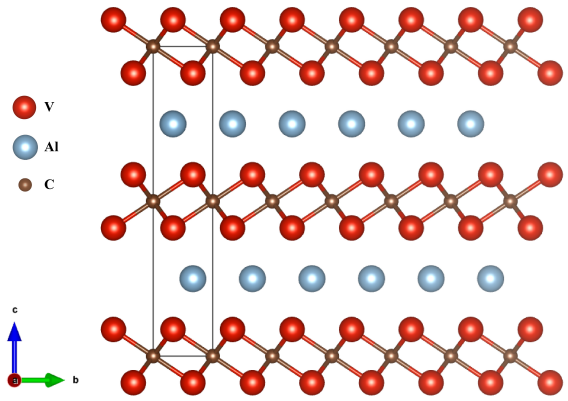

Figure 2.10: Layered structure of the V_2AlC MAX phase, with the unit cell indicated by the black rectangle. Figure drawn in VESTA[100]

Chapter 3

Experimental

3.1 Overview

In order to achieve the main goal of this work, which was to investigate the suitability of V_2C MXene as a constituent in both insertion and conversion cathode designs for RMBs, a series of experiments were conducted. A flowchart displaying an overview of the performed experiments is presented in figure 3.1. To begin with, two separate MAX phase batches were synthesized through a solid state sintering procedure. Then, the effects of particle size and etching duration on the following MXene synthesis was investigated through the use of various downsizing methods and etching parameters. The first batch, hereafter termed "Batch 1" (red arrows in flowchart), underwent rather simplistic downsizing by mortar and pestle before being etched for 96h, in order to synthesise the MXene. The second batch, hereafter termed "Batch 2" (blue arrows in flowchart), underwent a more complicated downsizing by wet planetary milling, where two different milling speeds of 300 RPM and 400RPM were utilized to establish a relationship between the milling speed and particle size as a function of time. Each of the samples obtained for the two milling speeds were then etched for different etching durations; the sample milled at 300 RPM was etched for 48h and 96h, while the sample milled at 400 RPM was etched for 24h and 48h. This was done in order to establish a relationship between the particle size and etching duration, with respect to completeness of the exfoliation process. The resulting powder samples were then characterized by XRD, scanning electron microscopy (SEM), energy-dispersive X-ray spectroscopy (EDX) and laser diffraction, in order to assess the effect of the different synthesis parameters utilized. Based on the results from the characterization, the sample from Batch 2 that was milled at 300 RPM and etched for 96h was chosen for further electrochemical testing. The sample resulting from Batch 1 was also utilized in further electrochemical testing, in order to assess and compare the effects of the downsizing procedures on the electrochemical performance of the MXene material.

To explore the Mg-ion intercalation properties of the V_2C MXene material, insertion cathodes were produced with the powders from Batch 1 and Batch 2 (separately), by a drop casting technique. The cathodes were then assembled in coin cells utilizing different electrolytes and thereafter subjected to galvanostatic cycling, with the purpose of assessing the electrochemical performance of the MXene in combination with different electrolytes. Moreover, to investigate the internal barriers of charge transfer in RMBs compared to LiBs, electrochemical impedance spectroscopy was performed on two sets of coin cells, where one set utilized an electrolyte with Mg-ions and the other utilized an electrolyte with both Li- and Mg-ions. Additionally, to verify the Mg stripping and plating capabilities of the electrolytes, cyclic voltammetry was performed on coin cells containing different electrolytes (orange arrows in flowchart).

To investigating if V_2C MXene could improve the performance of sulfur based cathodes for RMBs, a V_2C-S composite (green arrows in flowchart) was synthesised by a melt diffusion procedure, utilizing MXene from Batch 1. The composite material was characterized by a number of techniques, before being utilized in the production of conversion cathodes, which was done by a tape casting procedure. To evaluate the performance of the conversion cathodes, two parallel tests were performed; galvanostatic cycling of one RMB system and one LiB system, where both were utilizing the conversion cathodes. The LiB system was intended as a reference for the RMB system, with the purpose of providing grounds of comparison. A three electrode cell was utilized for the testing of the RMB system, as to gain information about the overpotentials in the cell, during electrochemical cycling. After completion of the testing, the three electrode cell was disassembled and the cell constituents were subjected to post-mortem characterization. Additionally, a rate test was performed for the conversion cathodes, in order to determine the current rate capabilities of the cathode design.

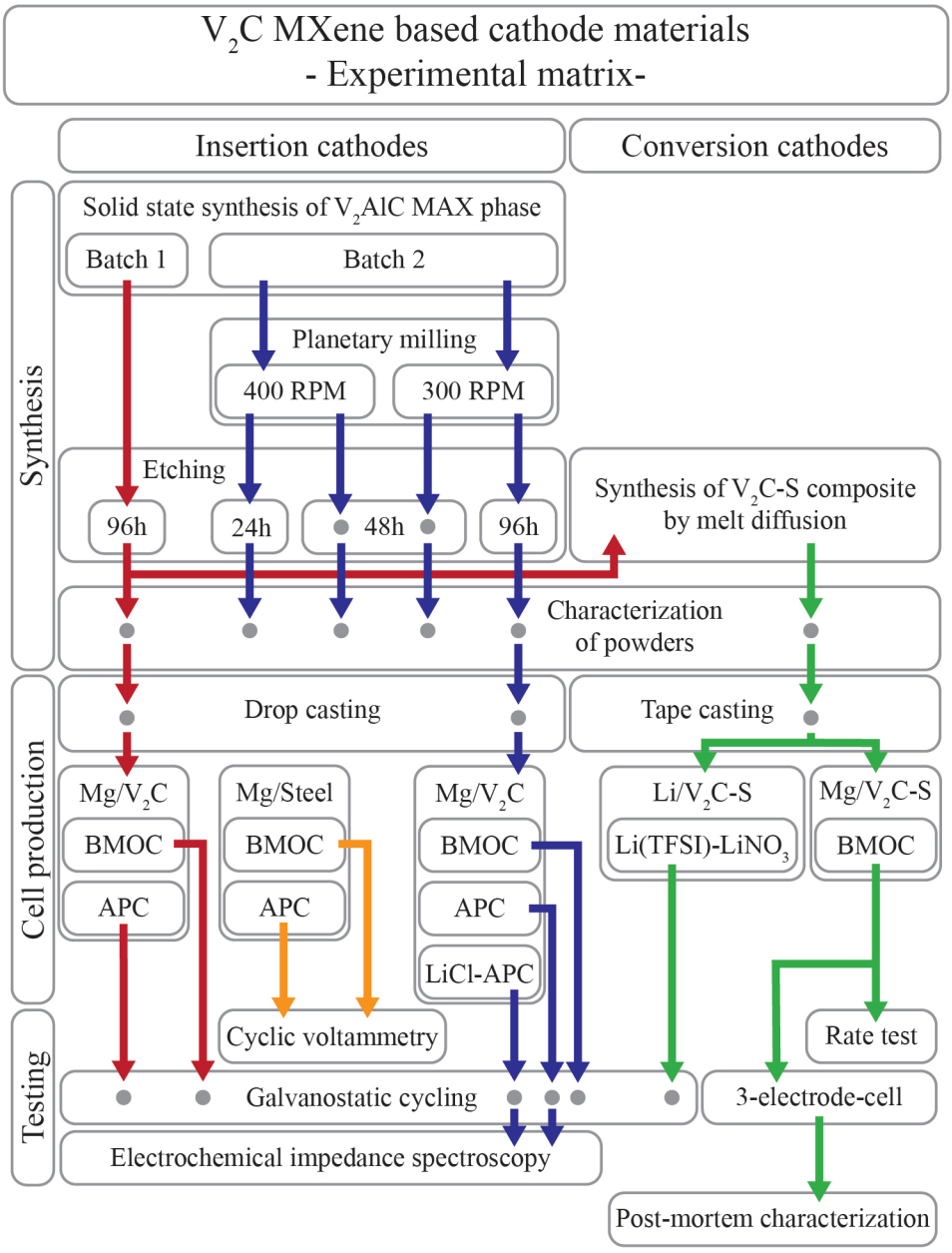

Figure 3.1: Overview of the experimental work that was performed, with a detailed view of the varying parameters utilized and the different battery systems evaluated. The red arrows indicate the path of the sample from Batch 1, while the blue arrows correspond to the path of the samples from Batch 2. The green arrows indicate the path of the composite material, and the orange arrows represent the cells that contained steel as the counter electrode instead of insertion or conversion cathodes. The abbreviated electrolyte names (BMOC, APC, LiCl-APC, Li(TFSI)-$LiNO_3$) are described in full in section 3.5.3.

3.2 MXene synthesis

3.2.1 MAX phase synthesis

For the synthesis of the V_2AlC MAX phase, vanadium powder (99.5%, 325 mesh, Sigma-Aldrich®), aluminium powder (99.5%, 325 mesh, Alfa Aesar) and graphite powder (99.5%, 400 mesh, TIMCAL TIMREX) precursors were mixed in a molar ratio of 2.00:1.30:1.00 in a 125 ml milling bottle. The vanadium and aluminium powders were stored and weighed inside an argon filled glovebox (MBraun, $O_2 < 0.1$ ppm, $H_2O < 0.1$ ppm), in order to prevent oxidation of the metal powders. Thereafter, approximately 300 g of 5 mm yttria stabilized zirconia milling balls were added to the milling bottle, leaving about 1/3 of the bottle empty. In order to minimize the exposure of the precursors to air and ensure complete mixing, the appropriate amount of isopropanol needed to exactly cover the milling balls was added. Finally, the graphite powder was weighed and added to the mixture, before the bottle was sealed and placed on a roll mill (U.S. Stoneware Long Roll Jar Mill). The precursors were milled for 16 h at 205 rpm, to ensure a homogeneous mixture.

After the milling procedure, the precursor mixture was poured through a 5 mesh (4 mm pore size) plastic sieve, in order to separate the milling balls from the mixture. In order to maximize the yield of this process step, the milling bottle and balls were then washed with isopropanol to collect the remaining precursor residues. Further, the isopropanol was evaporated by utilizing a rotavapor (Büchi®R 210), where the flask containing the precursor mixture was rotated in a water bath at 50 °C, whilst the pressure inside the flask was reduced to 140 mBar.

Prior to sintering, cylindrical pellets with diameter 10 mm and approximate mass 1 g were uniaxially pressed from the dry precursor mixture. The pressing was conducted manually in a toggle press (Mäder VK 2500-40). The procedure consisted of an initial step where a pressure of 2 kN was applied for 10 s, a second step in which the pressure was released for 10 s, and finally, a third step where a pressure of 4 kN was applied for 10 s. The purpose of the two first steps was to allow excess air to escape before applying the final pressure. After pressing, the pellets were placed in an alumina crucible, which was later inserted into a sealed tube furnace (Entech ETF 17). The tube furnace was then flushed with argon for a duration of 1 h, in order to achieve an inert atmosphere for the following sintering process. The sintering was carried out under flowing argon at 1500 °C for 4 h, using a heating and cooling rate of 300 °C h^{-1}.

Two separate batches of V_2AlC MAX phase pellets were synthesised by the procedure described above, and different downsizing techniques were used on the pellets from the two batches, with the purpose of investigating the effects of particle size distribution on the etching procedure. The sintered pellets from Batch 1, were ground to a fine powder and sieved through a 325 mesh sieve, equivalent to a pore size of 44 μm, in order to establish an upper limit for the particle size distribution prior to etching. A steel mortar and pestle was used for the downsizing procedure instead of the more common alternative made from agate, which was due to the hardness of the V_2AlC particles.

The pellets from Batch 2 were ground to a course powder using a steel mortar and pestle, in preparation for the powder to be further milled by planetary milling. V_2AlC MAX phase powder and tungsten carbide (WC) milling balls with a diameter of 7 mm were added to a 125 ml WC milling jar in a weight ratio of 1:10 ($\approx$11 milling balls per 3 g MAX phase powder), and the appropriate amount of isopropanol needed to exactly cover the milling balls was added to the milling jar. The milling was then carried out in a planetary mill (Retsch®PM100), where one portion of the powder was milled at 300 rpm for 6 h and a second portion was milled at 400 rpm for 6 h. Samples of the powders were retrieved prior to milling and after 10 min, 30 min, 1 h, 2 h, 4 h and 6 h of milling and analysed by laser diffraction to determine the particle size distribution, which is described in detail in section 3.3.2. Following the completion of the planetary milling, the powder mixture was separated from the milling balls and dried in a rotavapor, following the same procedure as described earlier in this section.

Before conducting the etching, both the pristine and milled MAX phase powders were characterized by XRD with the purpose of verifying that the correct MAX phase had been synthesized, that an acceptable phase purity had been achieved and to check for possible impurities from the milling procedure.

3.2.2 Etching of MAX phase

Due to regulations prohibiting master/project students from working with concentrated hydrofluoric acid (HF) at the department, the work described in this section involving HF has been carried out by the project's co-supervisors, with the author attending as an observer. However, the procedure will be described in full.

An aqueous solution containing 48% HF was used as etchant for the selective etching of Al from the V_2AlC MAX phase. First, 50 ml of the etchant solution was measured and poured in a plastic beaker containing a teflon coated magnet. A total amount of 2.5 g of V_2AlC powder was then immersed in the etching solution in small portions at a time and over a total period of 15 minutes, in order to control the formation of hydrogen gas and also the heating of the solution. After adding the powder, the beaker was covered with parafilm to prevent evaporation. A tiny hole was made in the parafilm to avoid the build-up of hydrogen gas. The dispersion was then left stirring at room temperature for the desired etching duration. In order to establish a relationship between particle size and etching time, a total of five samples were etched with varying etching durations: one sample from Batch 1 was etched for 96 h, two samples of the powder from Batch 2 that had been milled at 300 rpm was etched for 48 and 96 h, and two samples of the powder from Batch 2 that had been milled at 400 rpm was etched for 24 and 48 h.

After the chosen etching time, the powders were washed with deionized water to remove the HF and etching side products. The dispersions were therefore transferred to 125 ml plastic centrifuge bottles, and deionized water was added until the bottles were almost full. The dispersions were then centrifuged (VWR Mega Star 600) at 4350 rpm for 7 minutes, with an acceleration and deceleration time of 30 s and 190 s, respectively. The relatively

long acceleration and deceleration times were used to avoid any unnecessary shaking of the dispersions. Thereafter, the supernatant in each bottle was decanted and discarded, and the remaining powder mixtures were diluted with deionized water and centrifuged again. The centrifugation, decantation and dilution of the powder mixtures was repeated until the measured pH was above 5 (typically 4-5 centrifugations).

The different dispersions containing the powder mixtures were then vacuum filtered using a filter paper with a pore size of 0.22 μm (GVWP09050 Durapore®Membrane Filters), in order to remove the majority of the water. The filter papers with the powder mixtures were then dried under vacuum at 120 °C for 24 h in a vacuum oven (Binder VD 23) to evaporate the remaining water from the powders. After drying, the powders were scraped off the filter paper and stored in glass sample bottles.

3.3 Characterization of MAX phase and MXene powders

3.3.1 Crystallinity and phase purity

The synthesized V_2AlC and V_2C powders were investigated by X-ray diffraction (XRD), to evaluate the phase purity and crystal structure. The measurements were conducted in a Bruker D8 Focus Diffractometer, utilizing a Cu Kα radiation source and divergence slit size of 0.2 mm. The small slit size was chosen to reduce the background noise at lower 2Θ angles. In preparing the powder samples, Si cavity sample holders with a diameter of 10 mm were filled with powder, and then a thin glass slide was used to flatten the surface completely.

One sample of each powder was prepared and then scanned using a customized XRD scan program. The program scanned over the 2Θ range from 5° to 75°, divided into 4898 separate steps with a scan time of 0.68 s per step. This program was designed to give an overview enabling the identification of most of the peaks related to V_2AlC and V_2C, as well as any peaks related to impurity phases. The resulting diffractograms were analysed using the DIFFRAC.EVA software (Version 5.0.0.22) from Bruker, with the PDF 2018+ database. The V_2C and V_4C_3 MXene peaks were not part of this database, and the identification of these phases was therefore performed based on reported diffraction data from the literature[2,26,27,84,101–103]. Moreover, Rietveld refinement[104] of the diffractograms measured for the different MAX phase samples was performed using the TOPAS software (Version 5) from Bruker, in order to quantify the amounts of the different phases present each the samples. The Rietveld refinements were performed with structure files from the PDF 2018+ database for the detected phases, allowing the grain size to be varied between 20 μm and 300 μm for each phase, and with a polynomial order of 10 to match the background. The weighted profile residual (R_{wp}) was used as a measure of the quality of the fit between the calculated and experimental pattern.

3.3.2 Particle size and morphology

Particle size distributions of the V_2C and V_2AlC powders were obtained by analysing powder samples in a laser diffraction particle size analyser (Horiba Partica LA-960). The measurements were conducted by first dispersing small portions of the powder samples in the isopropanol solvent, until the transmittance level was reduced to between 80 and 90 % for both the red and blue laser. Thereafter, 2 minutes of sonication was performed on the dispersion to break up powder aggregates, followed by de-bubbling to remove possible air bubbles stuck in the analyser system. Lastly, the measurements were conducted and the system was thoroughly rinsed with isopropanol before the next sample was to be measured, as to avoid any cross contamination between different samples.

SEM images of the V_2C and V_2AlC particles were captured in a Carl Zeizz AG - ULTRA 55 SEM, using an aperture size of 30 μm, an acceleration voltage of 2.00 kV and a working distance of 10 mm. The samples were prepared by first dispersing a small amount of powder in isopropanol and thereafter carefully distributing a few drops of the dispersion on a silicon wafer, before the isopropanol was evaporated by placing the wafers on a hotplate that held a steady temperature of 60°C. Furthermore, EDX measurements of the different particles were performed by utilizing the X-ray detector (XFlash®4010) in the SEM. In order to achieve a sufficient signal range and intensity, the parameters were changed to an aperture size of 120 μm, an acceleration voltage of 15 kV and the high current mode was activated. The working distance was kept at 10 mm. In order to achieve representative data, measurements from five different points on the particles were analysed and used to calculate the average elemental composition of the materials. The analysis of the EDX data was done using the ESPRIT software (Version 1.9.4.3535), and the SEM images were analysed using the ImageJ software (Version 1.52a).

3.4 V_2C-S composite

3.4.1 Composite synthesis

The sulphur was incorporated into the MXene structure by a melt diffusion method. V_2C MXene and elemental sulfur powders (99.998%, Sigma Aldrich) were weighed in a weight ratio of 1:1 and carefully mixed in a mortar, before being transferred to a glass sample bottle. In order to prevent evaporated sulphur from escaping the sample vessel at elevated temperatures, the sample bottle opening was covered with aluminium foil. Then, the powder mixture was heat treated in a calcination furnace (Nabertherm B180) at 155°C for 10 h, with a ramp up time of 1 h and 30 min. The heat treatment was carried out in an ambient air atmosphere. Following the completion of the melt diffusion, the resulting composite was carefully ground down to a fine powder by mortar and pestle, before being transferred to a glass sample bottle and stored at room temperature.

3.4.2 Characterization of composite

The crystallinity and phase purity of the composite material was investigated by XRD, following the exact same sample preparation and measurement procedure as described in section 3.3.1. Furthermore, the particle size and morphology was examined by SEM, using the same sample preparation method and imaging parameters as described in section 3.3.2.

3.5 Cell manufacture

3.5.1 V_2C insertion cathode preparation

The preparation of cathodes with V_2C MXene as active material was done by making a slurry containing the MXene powder, a binder and a conductive carbon powder. The slurry comprised 120 mg (80 wt.%) V_2C MXene, 15 mg (10 wt.%) polyvinlylidine fluoride (PVDF) binder (Kynar F2801) and 15 mg (10 wt.%) carbon black (Imerys C-nergy super C65), mixed in 1 g of 1-Ethyl-2-pyrrolidone (NEP) (98%, Sigma-Aldrich®). The slurry was prepared by first weighing the NEP into a 5 ml steel shaker jar, followed by adding the PVDF powder. In order to ensure that the PVDF was properly dissolved in the NEP, the mixture was shaken with a 7 mm steel ball in a shaker mill (Retsch MM 400) at 25 Hz for 20 minutes. Thereafter, the carbon black and V_2C powders were added to the shaker jar, and the mixture was shaken at 25 Hz for additional 30 minutes to obtain a homogeneous slurry.

The cathodes were prepared by drop casting the slurry onto circular discs of carbon paper current collectors (Spectracarb 2050A-0550). The carbon paper discs had been pre-cut with a diameter of 16 mm using a specialized electrode cutter (Hohsen Corp.), and weighed prior to the casting process. After drop casting, the cathodes were placed on steel plate and dried at 60° for 30 minutes, before the cathodes were transferred to a sheet of aluminium foil and left to dry inside a fume hood for 16 h, followed by further drying under vacuum in a vacuum oven at 120 °C for 2 h. Afterwards, the cathodes were weighed and placed in labelled plastic bags, and then stored inside an argon filled glovebox.

3.5.2 V_2C-S conversion cathode preparation

The process of preparing conversion cathodes containing V_2C-S as the active material resembles the procedure described for the insertion cathodes in the previous section. A slurry comprising 150 mg (80 wt.%) V_2C-S, 18.8 mg (10 wt.%) carbon black and 18.8 mg (10 wt.%) PVDF was prepared, by first mixing PVDF powder with NEP in a weight ratio of 1:19 and then stirring the mixture until the PVDF was completely dissolved. Thereafter, the V_2C-S and carbon black powders were mixed in a 5 ml steel shaker jar and shaken in a shaker mill at 25 Hz for 5 minutes, in order to obtain a homogeneous powder mixture. The appropriate amount of PVDF solution corresponding to the target weight of PVDF was added to the shaker jar, and the mixture was shaken at 25 Hz for additional 30 minutes to obtain a homogeneous slurry. After the initial shaking duration, additional NEP was added and the shaking was repeated, until the viscosity of the slurry resembled that of motor oil. In contrast to section 3.5.1, the shaking procedure was performed without

the 7 mm ball, as iron contamination was observed and attributed to the shaking procedure.

The cathodes were prepared by tape casting the slurry onto a sheet of aluminium foil (Alfa Aesar, 0.025 mm, 99.45%). First, a rectangular aluminium foil sheet, measuring approximately 15 cm by 5 cm, was cleaned with ethanol and mounted on the tape caster. Secondly, the slurry was distributed on the foil in a tooth-shaped pattern and a 150 μm gap was utilized on the tape caster to produce the cast. After completion of the casting process, the cast was left on the tape caster hot plate to dry at 60 °C for 30 minutes, before being placed in a fume hood for further drying overnight at room temperature. As a final drying step, the cast was dried under vacuum for 3h at room temperature, in order to ensure that all the solvent had been evaporated. This was done in an antechamber connected to a glovebox designated for sulfur work, to minimize risk of cross contamination as sulfur easily sublimes. The specialized electrode cutter was used to cut circular cathodes of diameter 16 mm from the cast, before the cathodes were weighed and placed in labelled plastic bags. All cathodes were stored inside an argon filled glovebox. Additionally, to determine the weight of the active material on each electrode, a few aluminium discs of diameter 16 mm were cut from a sheet of aluminium and weighed, and the average weight of the discs was used as the reference weight for the electrodes.

3.5.3 Electrolytes

In this project, four different electrolytes were used; all phenyl complex (APC) in tetrahydrofuran (THF), 0.4 M lithium chloride (LiCl) in APC-THF, a borate magnesium oxide complex (BMOC) in 1, 2-dimethoxyethane (DME) and 1 M lithium bistrifluoromethanesulfonimidate (LiTFSI), 0.1 M lithium nitrate ($LiNO_3$) in 1,3-Dioxolane:DME (DOL:DME, v/v 1:1) (referred to as LiTFSI-$LiNO_3$-DOL-DME). Prior to electrolyte preparation, the electrolyte glass bottles and magnets were dried in an oven at 80 °C overnight to remove moisture. All electrolytes were prepared inside an argon filled glovebox. The APC-THF electrolyte was prepared according to the procedure described by Byeon et al.[105]. First, 4 ml THF (>99.9%, inhibitor-free, Sigma Aldrich) was slowly added to 2.5 ml of 2 M phenyl magnesium chloride in THF (Sigma Aldrich) in a glass bottle while stirring. Secondly, 4 ml of 0.5 M $AlCl_3$ in THF (Sigma Aldrich) was carefully added to the solution. Finally, the solution was left stirring overnight. The 0.4 M LiCl in APC-THF electrolyte was prepared by first adding 0.0509 g LiCl (99.7%, VWR) to a glass bottle and thereafter adding 3 ml of APC-THF, before the mixture was left stirring for 24h. The BMOC-DME preparation was based on the procedure described by Xu et al.[106]. First, 0.004 g of magnesium oxide (99.99%, Sigma-Aldrich) was added to a glass bottle. Then, 128 μl of the anion receptor tris(2H-hexafluoroisopropyl) borate (THFPB), corresponding to 0.2048 g, was added. The THFPB has a melting point of 31 °C, and was first heated at 40 °C for 5 minutes on a hot plate to remove crystallized particles. Lastly, 2 ml of DME (99.5%, inhibitor-free, Sigma Aldrich) was added, and the electrolyte was stirred overnight. Prior to electrolyte preparation, the DME was dried using molecular sieves (UOP Type 3Å) for more than 48h. The dried DME was filtered through a syringe filter (Whatman® Puradisc, 0.2 μm, PTFE), where the first 1 ml was discarded to avoid impurities from the filter. The LiTFSI-$LiNO_3$-DOL-DME electrolyte was prepared based on the work of Ding et al.[107]. The lithium salts were dried at 150 °C under vacuum for 15h in an antechamber connected

to the glovebox, before 0.0207 g of $LiNO_3$ (99.99%, Sigma Aldrich) and 0.8613 g LiTFSI (99.95%, Sigma Aldrich) was weighed and added to a glass sample bottle. Equal volumes of DOL(99.8%, Sigma Aldrich) and DME (4 ml of each) was added to a separate bottle, and stirred for 10 min. Then, 3 ml of the DOL-DME solution was added to the lithium salts, and the finished electrolyte was stirred overnight. The APC-THF, BMOC-DME and LiTFSI-$LiNO_3$-DOL-DME electrolytes were prepared by one of the co-supervisors of the project, while the LiCL-APC-THF electrolyte was prepared by the author.

3.5.4 Coin cell assembly

Magnesium metal anodes were prepared from sheets of magnesium foil (99.95%, Solution Materials) by polishing using a 30 μm grain sized silicon carbide (SiC) sandpaper (Struers), with the purpose of removing the oxide layer on the foil. The metal sheet was then washed with absolute ethanol to remove the majority of the particles resulting from the polishing. Further, a punch cutter (Bohem France) was used to cut discs of diameter 12 mm from the Mg foil, and the discs were then washed an additional time in absolute ethanol. In order to minimize the oxidation of the metal surface in-between process steps, the discs were stored in absolute ethanol before being dried under vacuum at 50 °C for 1 h. The separators (Whatman™ GF/A glass microfibre filters) were cut using a punching tool of diameter 17 mm, and then dried under vacuum at 50 °C for 1 h. Immediately after drying, the anodes and separators were introduced into an argon filled glovebox. Lithium metal anodes were prepared from sheets of Li foil (99.9%, Alfa Aesar) that were stored and handled inside the argon filled glovebox, in order to avoid reactions between the Li metal and ambient air. The Li anodes were prepared directly prior to cell assembly by first polishing the Li foil with a brush to leave a fresh metal surface, before a 12 mm punching tool was utilized to cut anode discs from the foil.

The coin cell batteries were assembled under an inert argon atmosphere in a glovebox, in order to avoid exposing the cathodes, anodes and electrolytes to ambient air. A schematic of the CR2016 coin cell is shown in figure 3.2, and in addition to the aforementioned constituents, the cell also comprise a stainless steel spacer disc (steel type 304, diameter 15.5 mm), a gasket, and a two-part casing. During assembly, the electrolyte was added in two portions of 55 μl, with one portion being added before the separator and one after. The portions were reduced to 40 μl for the cells containing Li anodes, as these anodes were thicker than the Mg anodes. After assembling and aligning all the parts, the cells were crimped in an automatic crimping tool (Hohsen Corp.), before being removed from the glovebox and wiped gently with ethanol to remove potential electrolyte residues from the crimping process. A total of 25 coin cells and one 3-electrode cell were assembled, where the cell ID and cell constituents (anode, cathode and electrolyte) for the cells are summarized in table 3.1. The purpose of the cells together with the cycling program, will be further described in section 3.7.

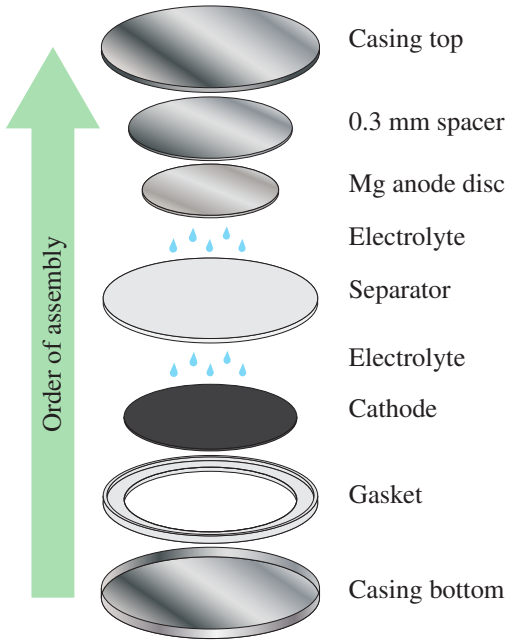

Figure 3.2: A schematic of the CR2016 coin cell, illustrating the order of assembly.

Table 3.1: Overview of the cells assembled in this work, specifying the anode material, cathode material and electrolyte utilized in each cell. The cells are grouped based on which electrochemical characterization techniques they underwent. Each cell is assigned an unique Cell ID based on the anode, electrolyte and cathode used, and IDs are on the form Anode/Electrolyte/Cathode. B1 and B2 are abbreviations of "Batch 1" and "Batch 2", and refer to the different batches of MXene that were synthesised.

Cell ID	Anode	Electrolyte	Cathode
Galvanostatic cycling (Insertion cathodes) Standard cycling programme: 0.2-2.1V, 10 mA/g, 100 cycles			
Mg/APC/V_2C-B1-1	Mg	APC-THF	V_2C B1
Mg/APC/V_2C-B1-2	Mg	APC-THF	V_2C B1
Mg/APC/V_2C-B1-3	Mg	APC-THF	V_2C B1
Mg/BMOC/V_2C-B1-1	Mg	BMOC-DME	V_2C B1
Mg/BMOC/V_2C-B1-2	Mg	BMOC-DME	V_2C B1
Mg/BMOC/V_2C-B1-3	Mg	BMOC-DME	V_2C B1
Mg/APC/V_2C-B2-1	Mg	APC-THF	V_2C B2
Mg/APC/V_2C-B2-2	Mg	APC-THF	V_2C B2
Mg/APC/V_2C-B2-3	Mg	APC-THF	V_2C B2
Mg/BMOC/V_2C-B2-1	Mg	BMOC-DME	V_2C B2
Mg/BMOC/V_2C-B2-2	Mg	BMOC-DME	V_2C B2
Mg/BMOC/V_2C-B2-3	Mg	BMOC-DME	V_2C B2
Extended cycling programme: 0.01-2.1V, 10 mA/g, 100 cycles			
Mg/BMOC/V_2C-B1-4	Mg	BMOC-DME	V_2C B1
Mg/BMOC/V_2C-B1-5	Mg	BMOC-DME	V_2C B1
Mg/BMOC/V_2C-B1-6	Mg	BMOC-DME	V_2C B1
Electrochemical impedance spectroscopy (Insertion cathodes)			
Mg/APC/V_2C-B2-4	Mg	APC-THF	V_2C B2
Mg/APC/V_2C-B2-5	Mg	APC-THF	V_2C B2
Mg/LiCl-APC/V_2C-B2-1	Mg	LiCl-APC-THF	V_2C B2
Mg/LiCl-APC/V_2C-B2-2	Mg	LiCl-APC-THF	V_2C B2
Cyclic voltametry			
Mg/APC/Steel	Mg	APC-THF	Steel
Mg/BMOC/Steel	Mg	BMOC-DME	Steel
Galvanostatic cycling (Conversion cathodes) - Three electrode setup: 0.4-2.1V, 10 mA/g, 10 cycles + 0.4-2.3V, 10 mA/g, 100 cycles			
Mg/BMOC/V_2C-S-3-Electrode	Mg	BMOC-DME	V_2C-S
Rate capability test (Conversion cathodes) Cycling programme: 0.4-2.5V			
Mg/BMOC/V_2C-S-1	Mg	BMOC-DME	V_2C-S
Mg/BMOC/V_2C-S-2	Mg	BMOC-DME	V_2C-S
Galvanostativ cycling of Li-systems for reference (Conversion cathodes) Cycling programme: 1.8-2.8V, 837.5 mA/g, Cycled until failure			
Li/Li(TFSI)/V_2C-S-1	Li	LiTFSI-$LiNO_3$-DOL-DME	V_2C-S
Li/Li(TFSI)/V_2C-S-2	Li	LiTFSI-$LiNO_3$-DOL-DME	V_2C-S

3.6 Three electrode cell assembly

To investigate and distinguish the overpotentials on the cathode and anode from the full cell, a 3-electrode cell (PAT-Cell-Aqu, EL-CELL) (Figure 3.3) was assembled utilizing a V_2C-S cathode, Mg anode and BMOC-DME electrolyte. Prior to assembly, all the reusable cell constituents, i.e. the cell base, the polyether ether ketone (PEEK) lower plunger, gold current collector, PEEK upper plunger and screw cap, were cleaned with ethanol, in order to remove any potential residues from previous cell experiments. Then, all the cell constituents were dried at 80 °C overnight before being introduced into an argon filled glovebox for cell assembly. In the first step of the assembly, the V_2-S cathode and gold current collector were inserted into the insulation sleeve containing the separator and a Mg reference ring, and locked in place by the lower plunger. Thereafter, the insulation sleeve assembly was inserted into the cell base, before 100 µl of BMOC-DME electrolyte was evenly distributed on the separator using a micropipette. The anode and gold current collector was inserted into the insulation sleeve assembly and locked in place by the upper plunger. Finally, the PE-seal and screw cap was mounted on the cell base, completely sealing the three electrode cell. The cell was removed from the glovebox and directly brought to a test station for electrochemical characterization.

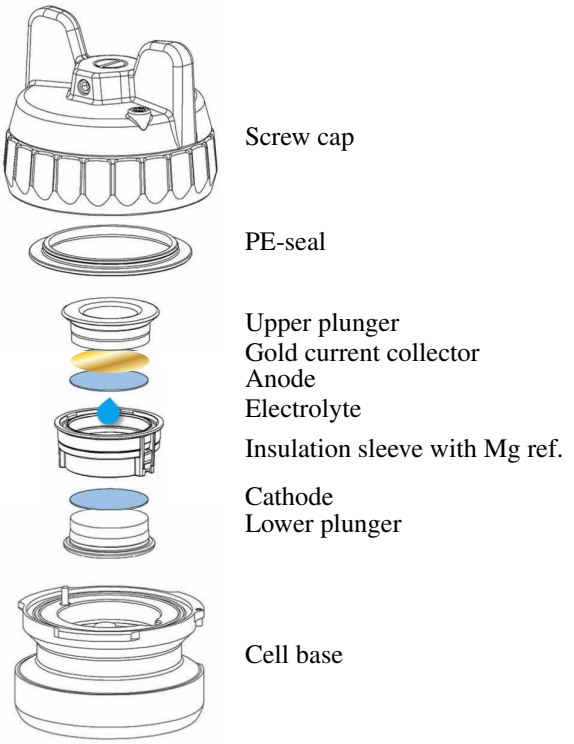

Figure 3.3: A schematic of the EL-CELL® PAT-Cell-Aqu three electrode test cell, illustrating the assembly of the different cell components. Adapted from the PAT-Cell user manual[108].

3.7 Electrochemical characterization

In order to verify the APC-THF and BMOC-DME electrolytes, Mg deposition and stripping capabilities on a stainless steel electrode (steel type 304, diameter 15.5 mm) was conducted by cyclic voltammetry (CV) on a Bio-Logic VMP300. The two cells were scanned from -0.9 to 2.1 V, with a scan rate of 1 mV/s and with a Mg counter electrode.

The galvanostatic cycling of the coin cell batteries was performed on a Bio-Logic BCS-805 cycler in a temperature controlled room of 20 °C. To investigate the effects of different electrolytes on the operating voltage and capacity, two sets of coin cells containing V_2C MXene insertion cathodes from Batch 1 were tested. The first set utilized the APC-THF electrolyte and the second set utilized the BMOC-DME electrolyte. A standard cycling programme consisting of 100 cycles of discharge to 0.2 V and charging to 2.1 V, at a constant current of 10 mA per gram of active cathode material was used for the cycling, and the relatively low current density was chosen to avoid that the current became a limiting factor for the electrochemical reactions, as the main goal of the cycling was to look for signs of Mg intercalation in the V_2C MXene. Additionally, as the capacities obtained for the first two sets of cells were limited, a third set of coin cells, containing insertion cathodes from Batch 1 and the BMOC-DME electrolyte, was tested using a cycling programme where the lower cutoff potential was lowered to 0.01V, to see if this could lead to improved Mg intercalation. The extended cycling programme consisted of 100 cycles of discharge to 0.01 V and charging to 2.1 V, at a constant current of 10 mA per gram of active cathode material. In order to investigate the effects of particle size and phase purity, two sets of cells containing V_2C MXene insertion cathodes from Batch 2 were tested. Again, the first set utilized the APC-THF electrolyte and the second set utilized the BMOC-DME electrolyte. The cells were cycled using the standard cycling programme. Additionally, to further evaluate the ion intercalation properties of the MXene, a set of coin cells utilizing the LiCl-APC-THF electrolyte were cycled using the standard cycling programme.

To evaluate the charge transfer resistance to investigate the ion intercalation process, electrochemical impedance spectroscopy (EIS) was conducted for two cells with the APC-THF electrolyte (Cell ID Mg/V_2C-B2-7 and Mg/V_2C-B2-8). To compare the Mg intercalation with the Li intercalation process, EIS was also conducted for two cells with the LiCl-APC-THF electrolyte (Cell ID Mg/V_2C-B2-9 and Mg/V_2C-B2-10). The impedance was measured over a frequency range of 10 mHz to 500 kHz with 6 measurement points per decade and an amplitude of 10 mV. The impedance of each cell was measured after one cycle and after the final cycle, in order to investigate how the impedance of each cell changed with cycling.

To verify that the V_2C-S conversion cathodes were able to perform properly, two coin cells containing Li anodes, LiTFSI-$LiNO_3$-DOL-DME electrolyte and conversion cathodes were tested. The two coin cells containing conversion cathodes were cycled at higher voltages than the cells containing insertion cathodes, as the electrochemical reactions between sulphur and lithium is expected to take place at higher potentials. The cycling programme used for these cells therefore consisted of 100 cycles of discharge to 1.8 V and charging to 2.8 V. The current was 837.5 mA/g sulfur in the cathode, which corresponds

to C/2 (where 1C is the current needed to fully charge the battery based on the theoretical capacity of sulfur, 1672 mAh/g). In order for the electrolyte to properly wet the cathode, all cycling programmes started with a 1 h dwelling step.

In order to assess the performance of the V_2C-S conversion cathodes in RMBs, a three electrode cell containing a V_2C-S conversion cathode, Mg anode and BMOC-DME electrolyte was cycled on a Bio-Logic VMP-300 cycler. A cycling programme consisting of 100 cycles of discharge to 0.4 V and charge to 2.1 V, at a constant current of 10 mA/g sulphur in the cathode, was utilized. As the cell appeared not to reach the charged state, the programme was aborted after 10 cycles and restarted with the upper cutoff potential increased to 2.3V.

To assess the performance of the conversion cathodes at different current rates, a rate test was performed for two coin cells containing conversions cathodes and the BMOC-DME electrolyte. The cells were cycled on a Bio-Logic BCS-805 cycler using a cycling program consisting of four steps with five cycles of discharge to 0.4 V and charge to 2.5 V, and one final step with thirty cycles of discharge to 0.4 V and charge to 2.5 V. In chronological order, the currents used in the different steps, given per gram of sulphur in the cathode, were: 10 mA/g, 25 mA/g, 50 mA/g, 100 mA/g and 10 mA/g. The reason for returning to 10 mA/g in the last step, after gradually increasing from 10 mA/g to 100 mA/g in the previous steps, is to test whether or not the cell is able to regain the capacity that is lost when cycling at high currents. As for the previously described tests, the rate tests also started with a 1 h dwelling step.

3.8 Post mortem characterization

The three electrode cell displayed severe capacity fade and signs of side reactions taking place during cycling, and it was therefore decided to investigated the cycled cathode, separator and anode by post mortem SEM and EDX, with an aim of identifying reasons for the capacity fade and potential side reactions. In order to do so, the three electrode cell was disassembled after cycling (in total 110 cycles) in its charged state inside a fume hood, and the cathode, anode and separator were placed on an aluminium foil sheet and left to dry in the fume hood overnight. Thereafter, the cell constituents were placed in labelled ziplock bags, before the unsealed bags were transferred to an antechamber and left under vacuum for 30 minutes, to ensure that all the DME had evaporated. After the evaporation of the solvent, the plastic bags with the cell constituents were sealed and stored inside the glovebox until further characterization was performed.

The post mortem characterization of the cathode, anode and separator by SEM and EDX was performed utilizing the same instrument parameters as described previously in section 3.3.2. The different samples were attached to sample stubs using carbon tape, and carefully inserted into the vacuum chamber. Both point scans, with a scan time of 30 seconds, and area scans, with a scan time of 120 seconds, were conducted on all three samples, in order to capture signs of possible side products formed during cycling. Additionally,

elemental mappings of the Mg anode and separator were performed to look for signs of polysulfide shuttling and other unwanted side reactions occurring at the anode or separator during cycling. A capture time of 10 minutes was used for the mappings.

Chapter 4

Results

4.1 Characterization of MAX phase and MXene powders

4.1.1 Crystallinity and phase purity

A general note regarding the readability of the figures in this section; the diffraction lines corresponding to secondary phases appearing in one or more spectra within one figure are labelled on the lowermost spectrum in which the diffraction line is present, generally indicating that the phase is also present in all the spectra plotted above as well.

The results of the XRD characterization performed on the synthesised V_2AlC MAX phase powder from Batch 1 before and after etching with HF for 96h are presented in figure 4.1, where the significant diffraction lines have been labelled. Due to a large number of diffraction lines close together, an additional plot presenting the segment between 30° and 50° is presented in figure 4.2. Both the pristine and the etched sample display diffraction lines corresponding to the V_2AlC MAX phase. Additionally, a diffraction line centred at approximately 11.2° related to the formation of V_2C MXene can be observed in the etched sample. Furthermore, diffraction lines corresponding to the V_4AlC_3 MAX phase are also present in both samples, and a diffraction line related to the V_4C_3 MXene is observed at approximately 6.1° for the etched sample. Two additional secondary phases, Al_2O_3 and Al_4C_3, are identified in both samples.

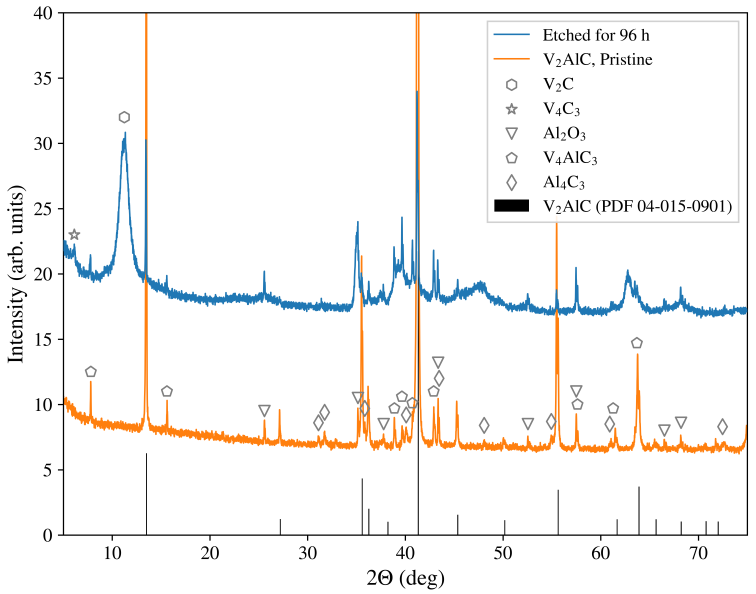

Figure 4.1: XRD plots of the synthesised V_2AlC MAX phase powder Batch 1 prior to etching (Pristine) and after being etched with 48% HF for 96h (Etched for 96h).

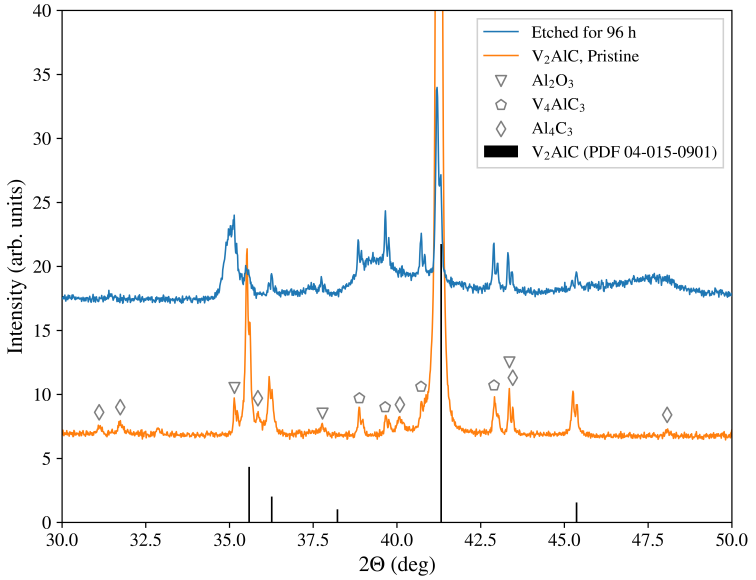

Figure 4.2: Overview of the diffraction lines in the section from 30.0° to 50.0° of the XRD plots in figure 4.1, showing the synthesised V_2AlC MAX phase powder Batch 1 prior to etching (Pristine) and after being etched with 48% HF for 96h (Etched for 96h).

The XRD spectra for both the pristine sample and the milled samples of the synthesised V_2AlC MAX phase powder from Batch 2 is presented in figure 4.3. All three spectra display diffraction lines corresponding to the V_2AlC MAX phase. Moreover, the spectra display diffraction lines corresponding to Al_2O_3 and VAl_3 secondary phases.Additionally, diffraction lines centred at 31.5 and 48.3° corresponding to WC appear in the sample milled at 400 RPM, but is not present in the sample milled at 300 RPM.

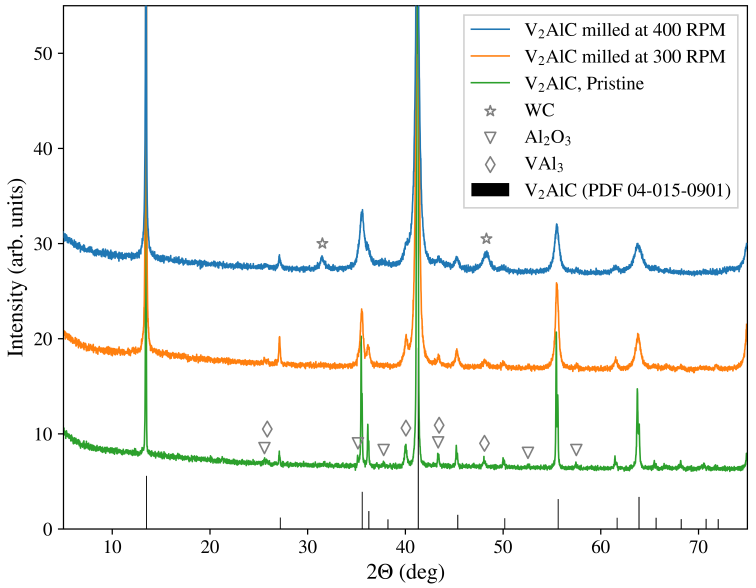

Figure 4.3: XRD plots of the pristine and milled powders of V_2AlC MAX phase Batch 2.

An overview of the calculated phase quantities for the different MAX phase samples is presented in table 4.1, where the ratio of the different phases is given in weight percent. In Batch 1 of the synthesised MAX phase powder, the wt. percentage of V_2AlC MAX phase was calculated to be 79.7%, with significant amounts of V_4AlC_3, Al_2O_3 and Al_4C_3 impurity phases present. For the pristine Batch 2 MAX phase sample, the calculated quantity of V_2AlC was 90.3%, with considerable amounts of Al_2O_3 and VAl_3 impurity phases present as well. The samples from Batch 2 that were milled at 300 RPM and 400 RPM display calculated phase quantities that are similar to the pristine sample, but with a significant amount of the additional WC impurity phase present for the sample milled at 400 RPM.

Table 4.1: Results of the Rietveld refinement of the XRD spectra that were measured for the different MAX phase powders. R_{wp} is the weighted profile residual, which is a numerical value quantifying the quality of the fit between the calculated and experimental pattern.

Sample	**Phase [%]**						**R_{wp}**
	V_2AlC	V_4AlC_3	Al_2O_3	Al_4C_3	VAl_3	WC	
V_2AlC Batch 1	79.7	5.7	8.0	6.6	-	-	7.701
V_2AlC Batch 2	90.3	-	4.3	-	5.4	-	7.273
V_2AlC Batch 2 Milled 300 RPM	90.0	-	2.7	-	7.3	-	12.357
V_2AlC Batch 2 Milled 400 RPM	87.1	-	3.2	-	7.2	2.5	9.807

The XRD spectra that were measured for the V_2AlC MAX phase powder milled at 300 RPM after etching with HF for 48h and 96h are presented in figure 4.4, with the plot of the milled powder before etching included for reference. A diffraction line related to the formation of V_2C MXene appear at approximately 9.2° and 9.0° for the samples etched for 48h and 96h, respectively. Additionally, the diffraction lines corresponding to Al_2O_3 that are displayed in the milled sample before etching are also present in the samples after etching, with two additional diffraction lines appearing at approximately 35.2 and 37.8° for the etched samples. Moreover, the diffraction lines corresponding to VAl_3, which were visible in the sample before etching, is not present in either of the two etched samples.

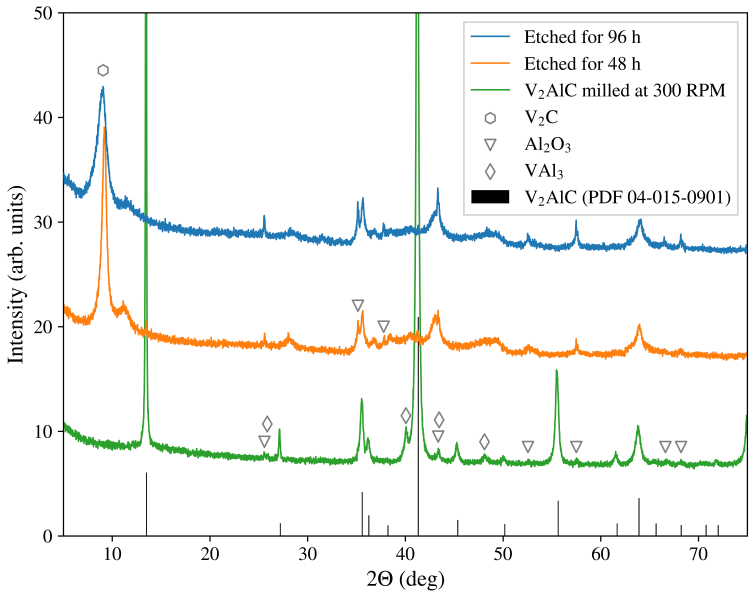

Figure 4.4: XRD spectra of the V_2AlC MAX phase powder (Batch 2) milled at 300 RPM prior to etching (V_2AlC milled at 300 RPM), after etching with HF for 48h (Etched for 48h) and 96h (Etched for 96h).

The XRD analysis of the V_2AlC MAX phase powder milled at 400 RPM after etching with HF for 24h and 48h are presented in figure 4.5, with the plot of the milled powder prior to etching included for reference. A diffraction line corresponding to the formation of V_2C MXene appears at approximately 8.3° and 8.1° for the samples etched for 24h and 48h, respectively. Furthermore, the diffraction lines corresponding to Al_2O_3 that were identified in the milled sample are also present in the etched samples, with additional diffraction lines appearing at approximately 25.6 and 52.6° for the etched samples. Similarly, the diffraction lines corresponding to WC in the milled sample were also present in the etched samples, with the etched samples displaying an additional diffraction line at approximately 73.1°. The diffraction lines corresponding to VAl_3 that were identified in the milled sample prior to etching are not present in either of the etched samples.

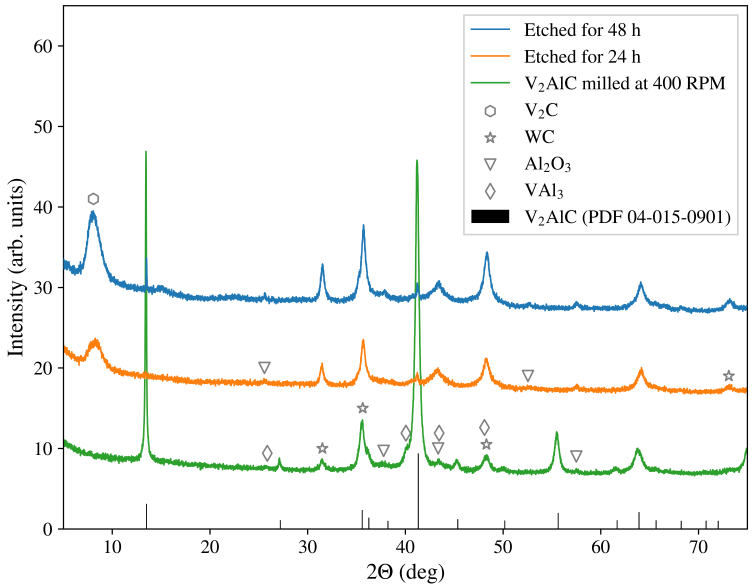

Figure 4.5: XRD spectra of the V_2AlC MAX phase powder (Batch 2) milled at 400 RPM prior to etching (V_2AlC milled at 400 RPM), after etching with HF for 24h (Etched for 24h) and 48h (Etched for 48h).

By utilizing Bragg's law[109], the interlayer distance between the transition metal layers in the different V_2AlC MAX phase and V_2C MXene samples can be calculated based on the positions of the (0002) peaks. The calculated interlayer distances are summarized in table 4.2.

Table 4.2: Overview of the (0002) peak positions and calculated interlayer distances for the synthesised V_2AlC MAX phase and V_2C MXene samples.

Sample				(0002) Peak position [°]	Interlayer distance [Å]
V_2AlC	Batch 1	Pristine		13.5	6.6
V_2C	Batch 1		Etched 96h	11.2	7.9
V_2AlC	Batch 2	Pristine		13.5	6.6
V_2AlC	Batch 2	Milled 300 RPM		13.5	6.6
V_2C	Batch 2	Milled 300 RPM	Etched 48h	9.2	9.6
V_2C	Batch 2	Milled 300 RPM	Etched 96h	9.0	9.8
V_2AlC	Batch 2	Milled 400 RPM		13.5	6.6
V_2C	Batch 2	Milled 400 RPM	Etched 24h	8.3	10.6
V_2C	Batch 2	Milled 400 RPM	Etched 48h	8.1	11.0

The XRD plot of the synthesised V_2C-S composite is presented in figure 4.6, where the XRD spectra of the V_2C MXene that was used for the synthesis is included for reference. The XRD spectrum for the composite material display diffraction lines corresponding to crystalline sulfur. Additionally, the diffraction lines related to the V_2C MXene remains after the melt diffusion procedure.

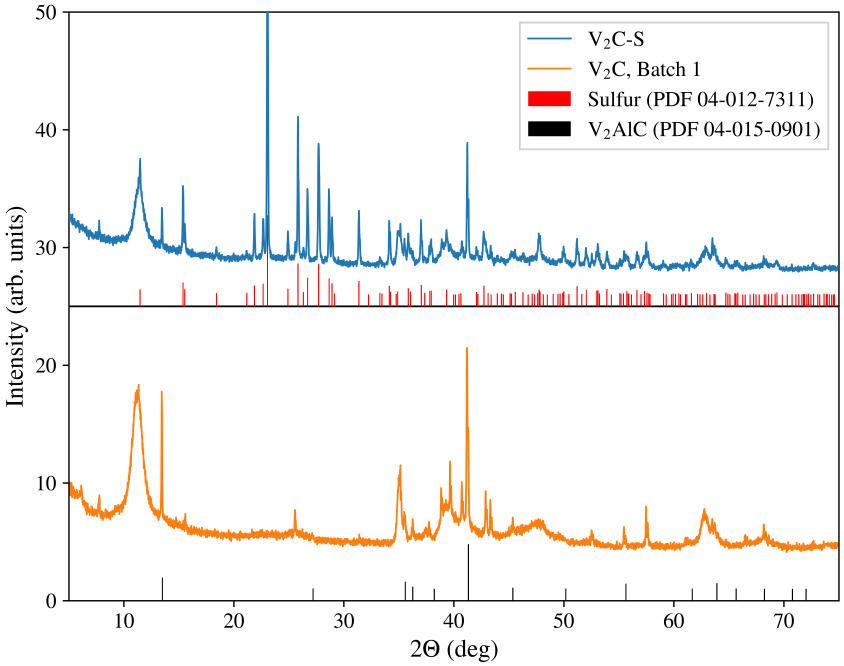

Figure 4.6: XRD plot of the V_2C-S composite produced by melt diffusion of a mixture of elemental sulfur and V_2C MXene Batch 1, with the XRD plot of the V_2C MXene included for reference.

4.1.2 Particle size and morphology

The particle size distribution measurements conducted on the V_2AlC MAX phase Batch 1 and the corresponding V_2C MXene powders are presented in figure 4.7. The mean particle size of the MAX phase powder particle size distribution was 24.8 μm, with a standard deviation of 15.0 μm. For the MXene powder particle size distribution, the mean particle size was 19.0 μm with a standard deviation of 10.5 μm. Furthermore, the SEM images acquired of the MAX phase and MXene particles from Batch 1 are included in figure 4.8. In the images captured at lower magnification (figure 4.8a and 4.8c), a wide particle size distribution is observed for both samples, with particle sizes ranging from the upper limit set by the sieve used in the synthesis (44 μm) down to submicron. Figure 4.8b is a high magnification image of a typical V_2AlC MAX phase particle, illustrating the characteristic layered structure of the MAX phase. Similarly, the high magnification image presented in figure 4.8d displays a typical MXene particle, where the accordion-like morphology resulting from the etching step is observed.

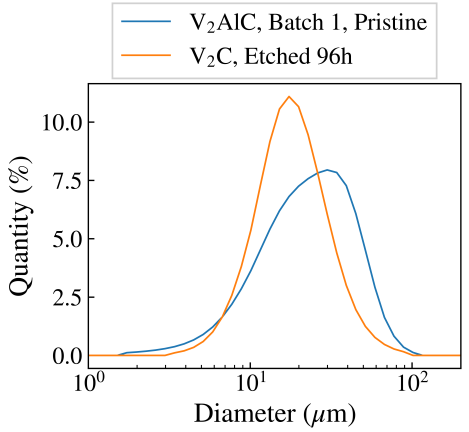

Figure 4.7: Particle size distribution of the V_2AlC MAX phase powder (Blue, "V_2AlC, Batch 1, Pristine") and V_2C MXene powder (Orange, "V_2C, Etched 96h") from Batch 1.

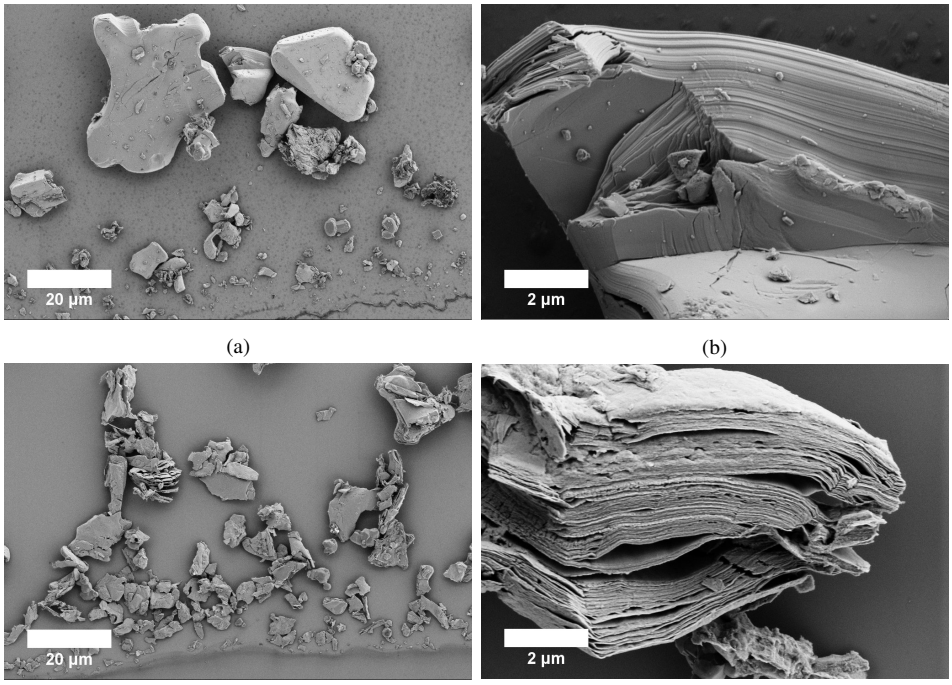

Figure 4.8: SEM images of the synthesised V_2AlC MAX phase particles from Batch 1 (a and b) and the V_2C MXene particles resulting after 96h of etching of the MAX phase (c and d).

The particle size distribution results from the milling experiments performed on the synthesised V_2AlC MAX phase powder from Batch 2 is presented in figure 4.9. Figure 4.9a illustrates how the mean diameter of the particles varied with milling duration for milling at 300 RPM and 400 RPM. Moreover, the relation between the standard deviation and milling time is presented in figure 4.9b. In both samples, the mean and standard deviation is observed to decrease rapidly during the first two hours of milling, and thereafter a rather moderate decrease is observed for the last four hours of milling. The particle size distribution of the powder prior to milling and after 6 h of milling for the 300 RPM milling procedure and the 400 RPM milling procedure is presented in figure 4.9c and 4.9d, respectively. For the milling procedure utilizing a milling speed of 300 RPM, the pristine particles displayed a bimodal distribution with a mean of 337.2 µm and a standard deviation of 411.5 µm, while the particles that had been milled for 6h displayed a distribution with a mean of 6.3 µm and a standard deviation of 2.6 µm. The bimodal distribution of the pristine sample was observed to change into a unimodal distribution with a mean of 25.5 µm after 10 minutes of milling, and the particle size distributions measured at the different milling durations for both Batch 1 and Batch 2 are included in Appendix A (figure A.1 and A.2). For the procedure utilizing 400 RPM, the pristine powder displayed a distribution with a mean of 47.9 µm and a standard deviation of 44.5 µm, while the powder that had been milled for 6h had a distribution with a mean of 2.0 µm and a standard deviation of

1.5 µm. The discrepancy in the size distributions of the pristine powders from Batch 1 and Batch 2 (blue lines in figure 4.9c and 4.9d) is related to the preparation of the powder prior to milling and will be further discussed in chapter 5.

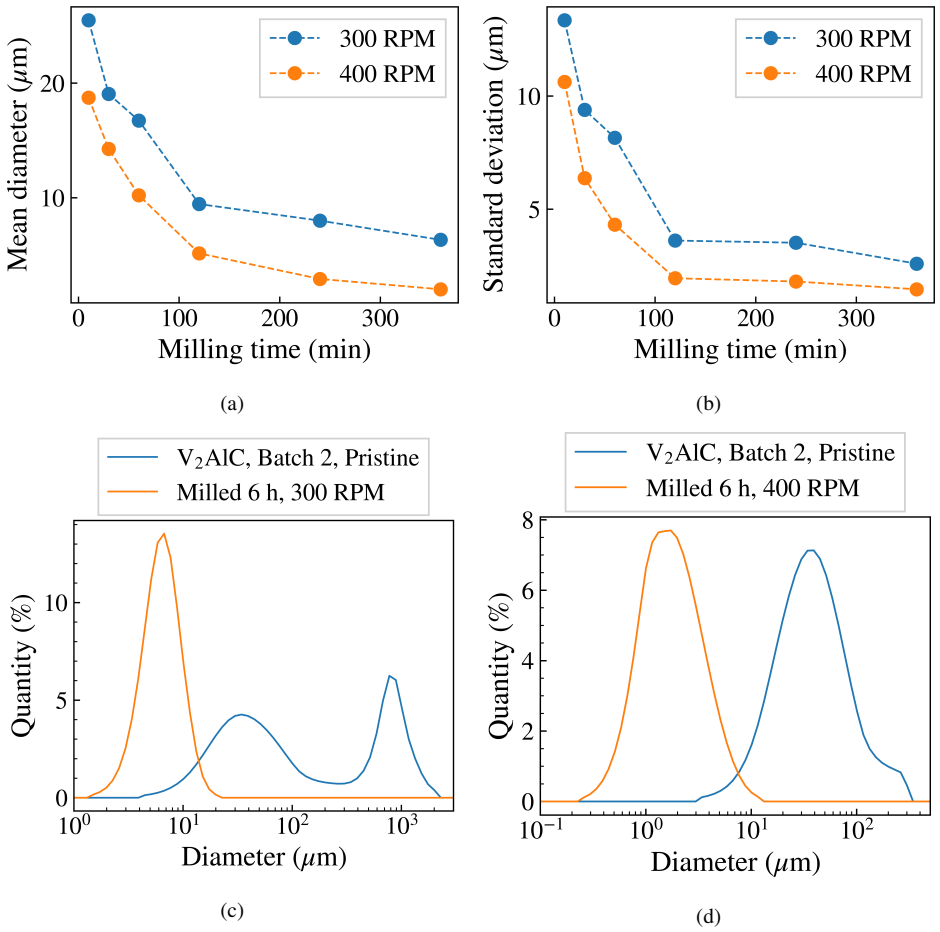

Figure 4.9: (a) Relation between the mean diameter of the MAX phase particles and milling time when milled at 300 RPM (blue) and 400 RPM (orange). (b) Relation between the standard deviation of the particle size distribution and milling time for MAX phase particles milled at 300 RPM and 400 RPM. (c) Particle size distribution of the pristine MAX phase powder (Batch 2) (blue) and the powder milled at 300 RPM for 6h (orange). (d) Particle size distribution of the pristine MAX phase powder (Batch 2) (blue) and the powder milled at 400 RPM for 6h (orange).

The SEM images captured of the MAX phase powder from Batch 2 prior to milling and after milling is presented in figure 4.10. In the image of the pristine powder (figure 4.10a) a wide particle size distribution is observed, with sizes ranging from a few microns to around one hundred microns. The images of the powders milled for 6h (figure 4.10b and 4.10c) confirm smaller particle sizes compared to prior to milling, but the observed size

distributions are still rather wide, ranging from an upper limit of approximately ten microns to submicron. Furthermore, the images indicate that the particle size distribution of the powder milled at 300 RPM has a larger mean than the distribution of the powder milled at 400 RPM, which is consistent with the observations from the particle size distribution measurements.

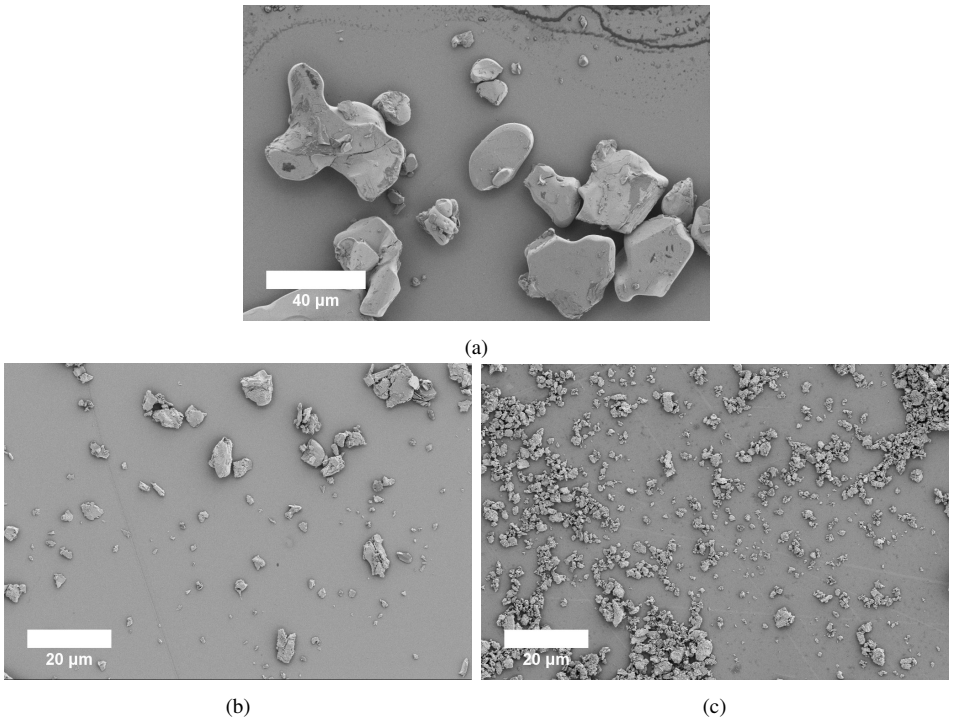

Figure 4.10: SEM images of (a) the pristine V_2AlC MAX phase powder (Batch 2) prior to planetary milling, (b) the MAX phase powder after milling at 300 RPM for 6h and (c) the MAX phase powder after milling at 400 RPM for 6h.

The particle size distribution measurements of the milled MAX phase powders after etching are presented in figure 4.11, with the size distributions of the powders prior to etching included for reference. For the powder milled at 300 RPM, an etching duration of 48h yielded a powder where the particle size distribution had a mean of 6.9 µm and a standard deviation of 4.1 µm, while the powder resulting after 96h of etching displayed a size distribution with a slightly lower mean of 4.8 µm and a standard deviation of 2.3 µm. In other words, only minor changes in the particle size distributions were observed for the etched samples relative to the pristine sample. Interestingly, the powder that was milled at 400 RPM and etched for 24h displayed a bimodal particle size distribution with a mean of 42.4 µm and a standard deviation of 52.6 µm, with the two maxima centred at approximately 1.7 µm and 51.5 µm. Similarly, for the powder milled at 400 RPM and etched for 48h, a bimodal particle size distribution with a mean of 16.3 µm and a standard deviation of 17.0 µm was obtained, where the two maxima are centred at approximately 1.3 µm and 34.3 µm.

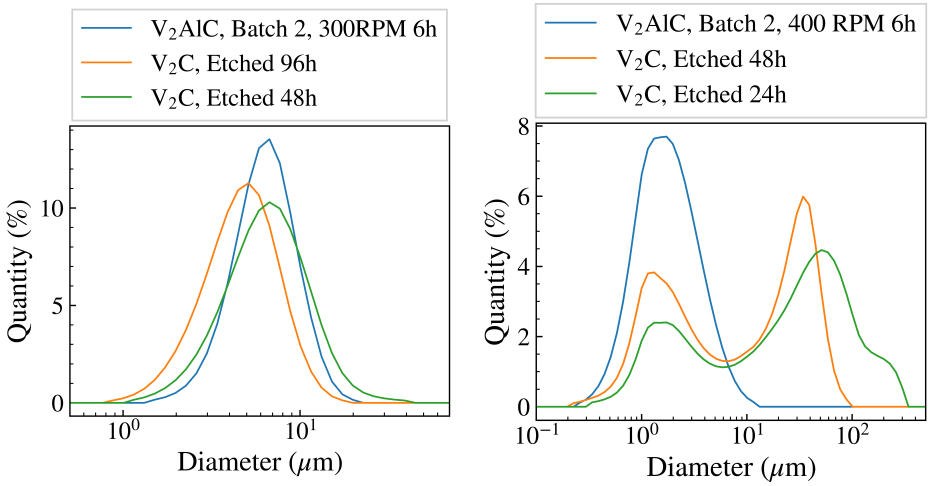

(a) (b)

Figure 4.11: (a) Particle size distributions of the V_2AlC MAX phase powder (Batch 2) milled at 300 RPM for 6h, after etching for 48h and after etching for 96h. (b) Particle size distributions of the V_2AlC MAX phase powder (Batch 2) milled at 400 RPM for 6h, after etching for 24h and after etching for 48h.

The SEM images captured of the powders resulting from the 48h and 96h etching of the MAX phase powder milled at 300 RPM are presented in figure 4.12. Particle sizes ranging from around ten microns to submicron is observed for both etching durations, with the particles in the sample etched for 96h (figure 4.12c and 4.12d) appearing to be smaller compared to the ones in the sample that was etched for 48h (figure 4.12a and 4.12b). Moreover, figure 4.13 presents the SEM images of the powder resulting from the 24h and 48h etching of the MAX phase powder that had been milled at 400 RPM. In general, the particle sizes of the two powders appear to be in the range of a few microns to a couple hundred nanometres. Additionally, a relatively large amount of agglomerates can be observed for both samples.

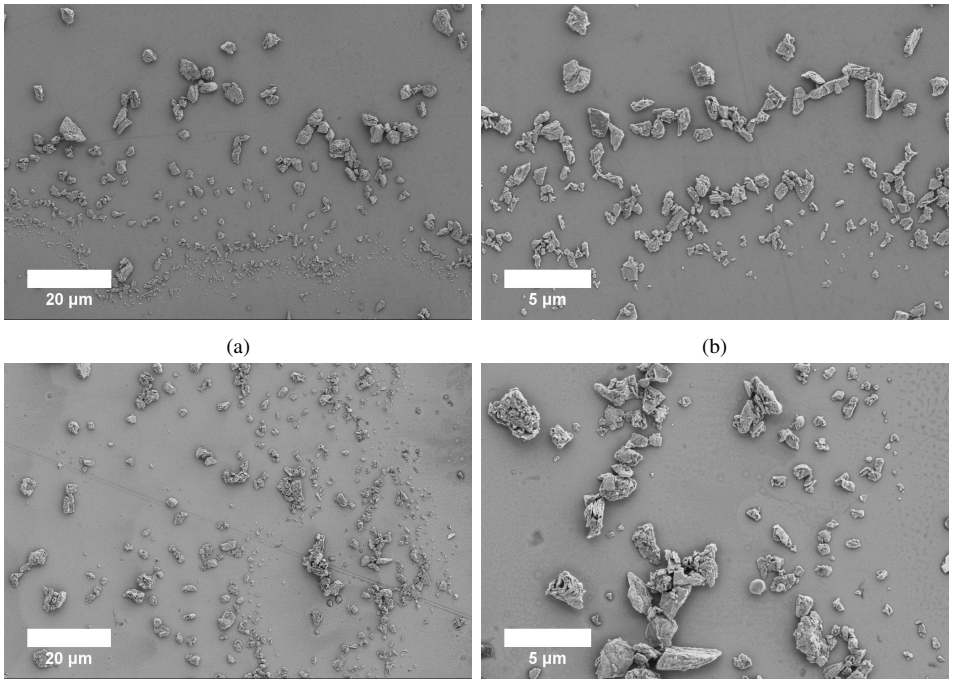

Figure 4.12: SEM images of the powders that had been milled at 300 RPM and etched for 48 h (a and b) and for 96h (c and d).

The EDX measurements of the different V_2AlC MAX phase, V_2C MXene and V_2C-S composite samples are summarised in table 4.3, where the atomic ratios of Al, C, O, F, W and S are given relative to a vanadium content of 2.00. In addition to the expected vanadium, aluminium and carbon elements, all the samples contained significant amounts of oxygen as well. Additionally, fluorine was observed in all of the etched samples. Trace amounts of tungsten was detected in the milled MAX phase samples, and the tungsten was still present after etching for both samples milled at 400 RPM, but not in the two samples milled at 300 RPM.

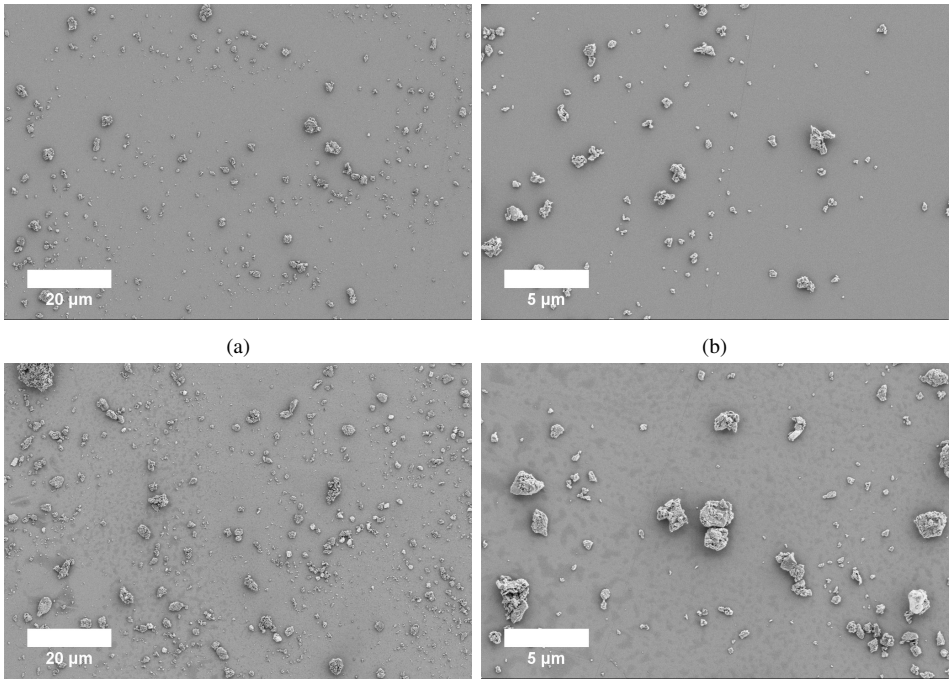

Figure 4.13: SEM images of the powders that had been milled at 400 RPM and etched for 24 h (a and b) and for 48h (c and d).

Table 4.3: Elemental compositions of the different powder samples calculated from EDX measurements, where the atomic ratios are given relative to a vanadium content of 2.00. ”-” indicates that the specific element was not detected in the given sample. *: Tungsten was detected in only one of the fifteen measured points in the sample. **: Tungsten was detected in fourteen of the fifteen measured points in the sample.

Sample	**Element**						
	V	Al	C	O	F	W	S
Batch 1:							
V_2AlC	2.00	0.80	0.60	0.24	-	-	-
V_2C	2.00	0.05	0.51	0.24	0.47	-	-
Batch 2:							
V_2AlC, Pristine	2.00	0.96	0.65	0.15	-	-	-
V_2AlC, Milled 300 RPM	2.00	1.22	0.72	0.30	-	0.01*	-
V_2AlC, Milled 400 RPM	2.00	1.69	1.12	0.74	-	0.01**	-
V_2C, Milled 300 RPM, Etched 48h	2.00	0.05	0.68	0.36	0.59	-	-
V_2C, Milled 300 RPM, Etched 96h	2.00	0.10	1.74	0.63	0.95	-	-
V_2C, Milled 400 RPM, Etched 24h	2.00	0.10	1.00	0.50	0.43	0.29	-
V_2C, Milled 400 RPM, Etched 48h	2.00	0.11	1.15	0.63	0.80	0.04	-
Composite:							
V_2C-S Composite	2.00	0.19	0.65	0.38	0.43	-	<0.01

The SEM images of the synthesised V_2C-S composite are presented in figure 4.14. A number of aggregated particles can be observed in the images, with sizes ranging from a few microns to hundreds of microns.

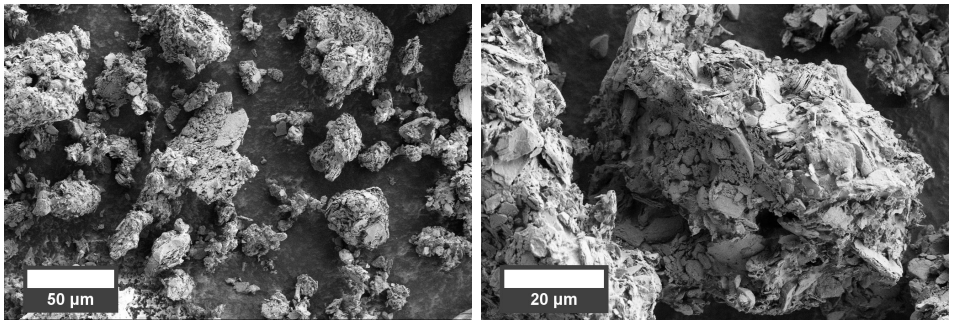

(a) (b)

Figure 4.14: SEM images of the V_2C-S composite particles that were synthesised by melt diffusion of a mixture of elemental sulfur and V_2C MXene powder from Batch 1.

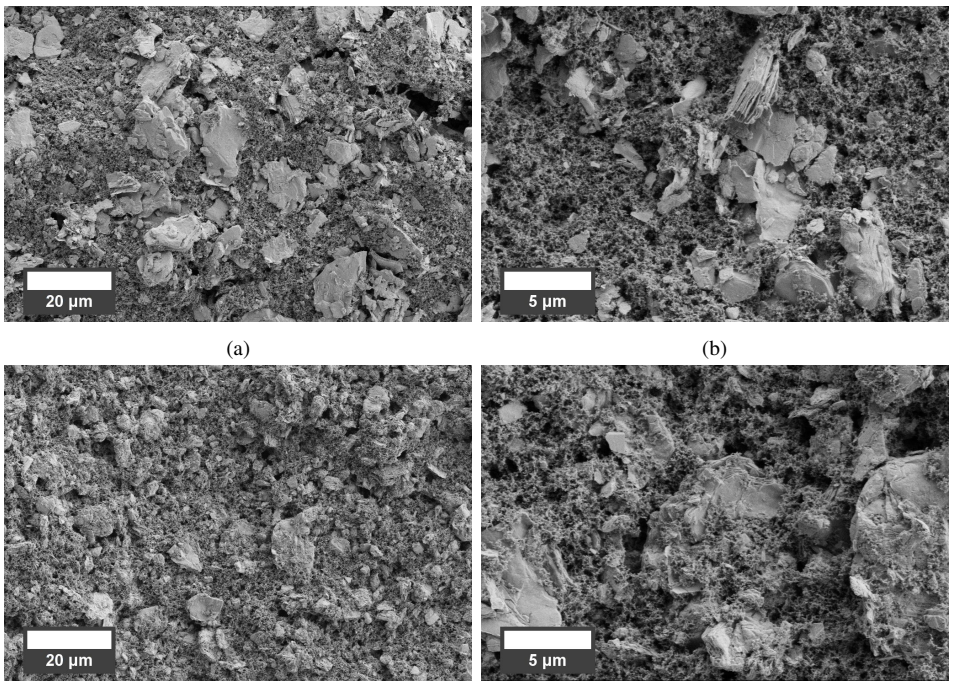

(a) (b)

(c) (d)

Figure 4.15: SEM images of the insertion cathode containing the V_2C MXene from Batch 1 (a and b) and the insertion cathode containing the V_2C MXene from Batch 2 (c and d).

Figure 4.15 shows SEM images captured of one insertion cathode containing V_2C MXene from Batch 1 (4.15a and 4.15b) and one insertion cathode from Batch 2 (4.15c and 4.15d). The overview images captured at the lower magnification (4.15a and 4.15c) depict how the active material is embedded in the composite cathode with carbon black and PVDF, and a rather homogeneous distribution of the particles of active material can be observed for both samples. In the images captured at higher magnification (4.15b and 4.15d), it can be observed that the orientation of the particles vary greatly within each sample.

4.2 Electrochemical characterization

4.2.1 V_2C insertion cathodes

Electrolyte verification

The CV scans of the APC-THF and BMOC-DME electrolytes are presented in figure 4.16 and 4.17, respectively. The APC-THF electrolyte displayed non-symmetric cathodic currents between -0.9 and 0V and anodic currents between 0 and 2.1V. In the first cycle, rather small overpotentials of around 0.1-0.2V are observed, and these are reduced to approximately 0.05V in the second cycle, before stabilizing at values below 0.2V for the remaining cycles. Additionally, decent current rates related to the stripping and plating of magnesium are observed from the first cycle and onwards. Furthermore, for the first nine cycles, the BMOC-DME electrolyte displayed large overpotentials resulting in negligible currents. However, in the tenth cycle, the overpotentials were reduced to values below 0.05V resulting in non-symmetric cathodic currents between -0.9 and 0V and anodic currents between 0 and approximately 1.4V. The overpotentials are further reduced in the subsequent cycles and stabilizes at values below 0.02V, and good current rates related to the stripping and plating of magnesium are observed for the remaining cycles. Both electrolytes appear to be electrochemically stable below the upper cutoff voltage of 2.1V, as the electrolytes display no significant anodic currents at high voltages.

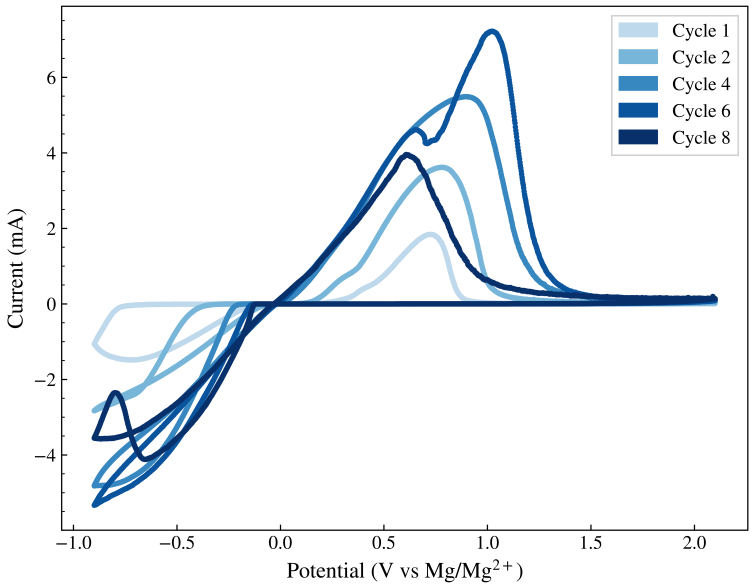

Figure 4.16: Selected cycles from the cyclic voltametry of a coin cell containing a Mg anode, APC-THF electrolyte and steel counter electrode (Mg/APC/Steel).

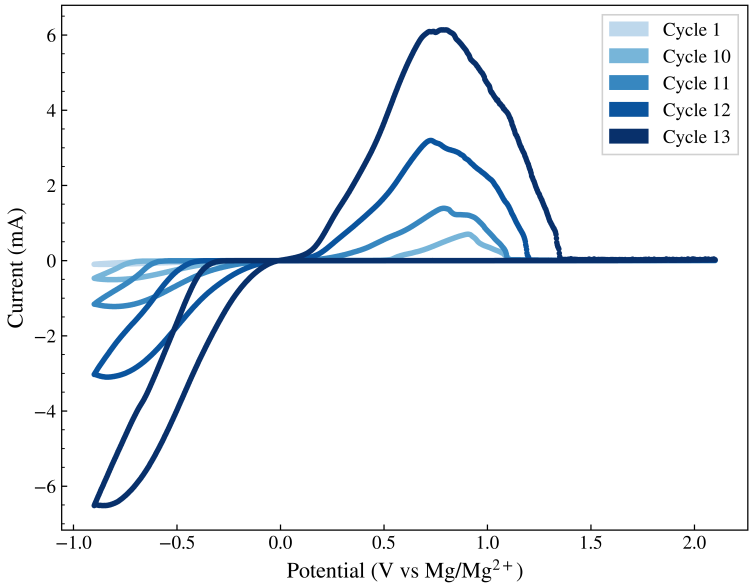

Figure 4.17: Selected cycles from the cyclic voltametry of a coin cell containing a Mg anode, BMOC-DME electrolyte and steel counter electrode (Mg/BMOC/Steel)

Galvanostatic cycling

Figure 4.18 presents an example of typical charge and discharge capacities as well as voltage profiles recorded for the coin cells utilizing insertion cathodes containing the V_2C MXene from Batch 1 and APC-THF electrolyte, cycled with the standard cycling programme. The cells typically displayed initial voltages of approximately 1.6V before cycling, with initial discharge capacities of around 3.7-3.8 mAh/g. The charge and discharge capacities were reduced to about 1.0-1.5 mAh/g after the first cycle, and the cells stabilised around this value for the remainder of the cycles. A figure presenting the cycling results for each of the different cells containing V_2C MXene insertion cathodes from Batch 1 and the APC-THF electrolyte can be found in Appendix B (figure B.1).

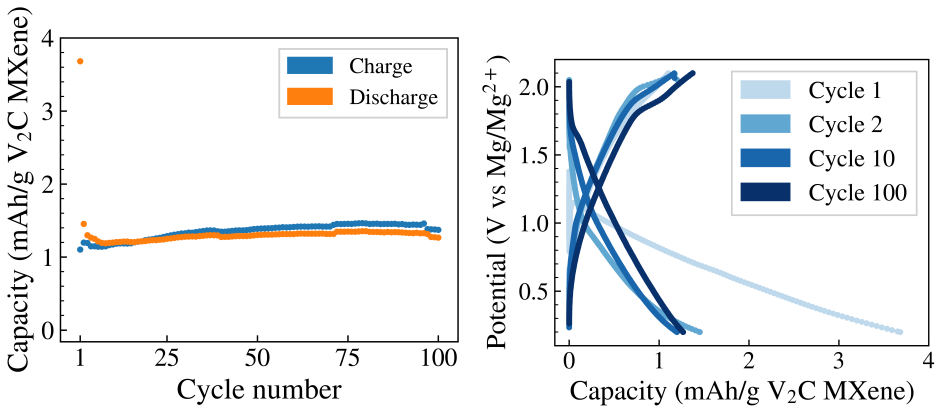

(a) (b)

Figure 4.18: Typical cycling performance and voltage profiles for cycle number 1, 2, 10 and 100 for V_2C MXene insertion cathodes from Batch 1 with APC-THF electrolyte. The results were obtained for Mg/APC/V_2C-B1-1 cycled with the standard cycling programme.

Figure 4.19 displays an example of typical charge and discharge capacities as well as voltage profiles recorded for the coin cells utilizing insertion cathodes containing the V_2C MXene from Batch 1 and the BMOC-DME electrolyte, cycled with the standard cycling programme. The cells displayed initial voltages ranging from 1.5 to 1.9V before cycling. The cells were observed to require between 52 and 68 cycles before they started cycling properly, and following the onset of proper cycling behaviour, initial discharge capacities ranging from 3.8 to 5.6 mAh/g were observed. After the first cycle, the charge and discharge capacities were between 0.3 and 0.6 mAh/g. A figure presenting the cycling results for each of the different cells containing V_2C MXene insertion cathodes from Batch 1 and the BMOC-DME electrolyte, after cycling with the standard cycling programme, can be found in Appendix B (figure B.2).

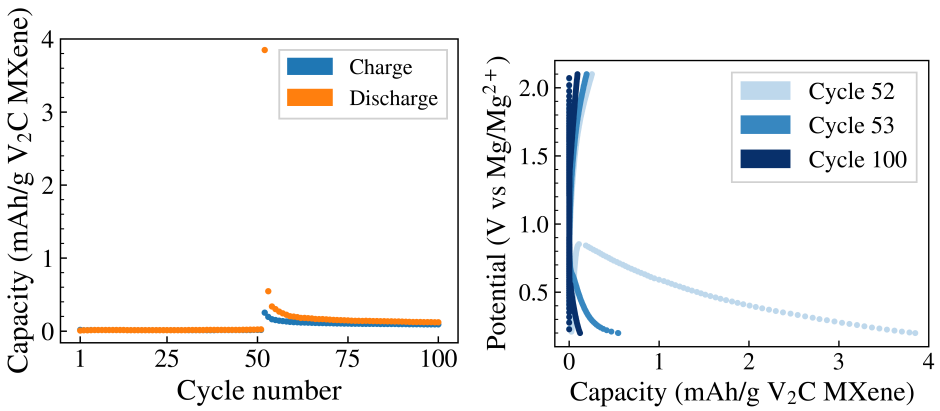

(a) (b)

Figure 4.19: Typical cycling performance and voltage profiles for the first, second, tenth and final cycle (counting from the first cycle where proper cycling behaviour was observed) for V_2C MXene insertion cathodes from Batch 1 with BMOC-DME electrolyte. The results were obtained for Mg/BMOC/V_2C-B1-1 cycled with the standard cycling programme.

An example of the typical cycling behaviour observed for the coin cells containing V_2C MXene insertion cathodes and BMOC-DME electrolyte that were cycled with the extended cycling programme is presented in figure 4.20. The cells displayed initial voltages ranging from 1.7 to 1.9V before cycling, and initial discharge capacities between 8.0 and 11.3 mAh/g. Similarly to the cells cycled with the standard cycling programme, the subsequent charge and discharge capacities of the cells cycled with the extended cycling programme were also reduced after the first cycle, with observed capacities ranging from 1.2 to 1.8 mAh/g. The capacities continued to decrease with further cycling and stabilised around 0.2-0.4 mAh/g. Furthermore, two of the three cells were observed to require several cycles before cycling properly, similar to what was observed for the cells with BMOC-DME electrolyte cycled with the standard cycling programme. The third cell cycled properly from the first cycle. A figure presenting the cycling results for each of the different cells containing V_2C MXene insertion cathodes from Batch 1 and the BMOC-DME electrolyte, after cycling with the extended cycling programme, can be found in Appendix B (figure B.3)

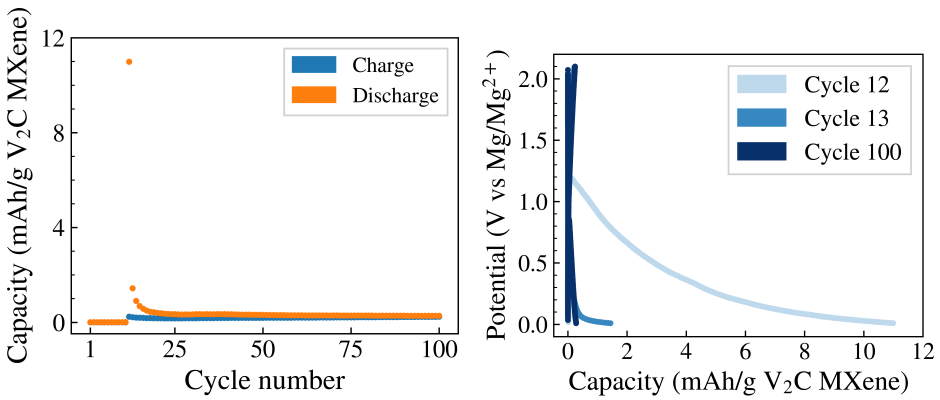

(a) (b)

Figure 4.20: Typical cycling performance and voltage profiles for the first, second, tenth and final cycle (counting from the first cycle where proper cycling behaviour was observed) for V_2C MXene insertion cathodes from Batch 1 with BMOC-DME electrolyte. The results were obtained for Mg/BMOC/V_2C-B1-4 cycled with the extended cycling programme, utilizing a lower cutoff voltage of 0.01V.

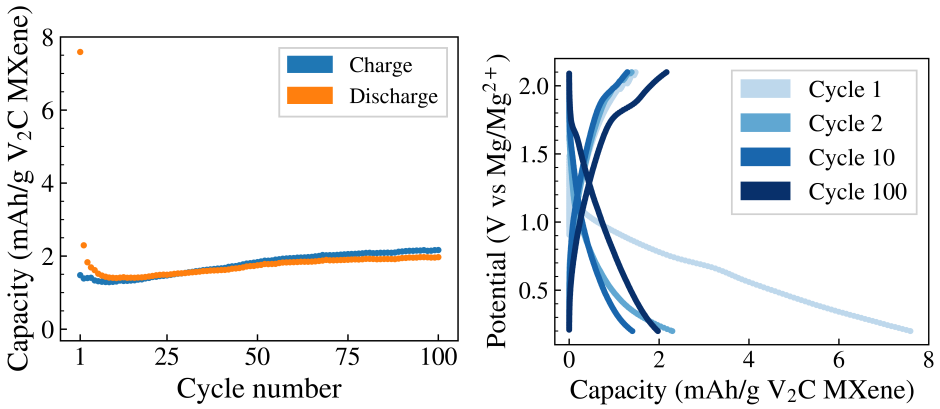

(a) (b)

Figure 4.21: Typical cycling performance and voltage profiles for cycle number 1, 2, 10 and 100 for V_2C MXene insertion cathodes from Batch 2 with APC-THF electrolyte. The results were obtained for Mg/APC/V_2C-B2-1 cycled with the standard cycling programme.

Figure 4.21 displays an example of typical capacities and voltage profiles obtained for the galvanostatic cycling of the coin cells containing V_2C MXene insertion cathodes from Batch 2 and APC-THF electrolyte, cycled with the standard cycling programme. In general, the results from the cycling of cathodes from Batch 2 were similar to the results obtained from the cathodes from Batch 1, but slightly higher specific capacities were ob-

served for Batch 2. More specifically, the cells displayed initial voltages ranging from 1.6 to 1.8V, and initial discharge capacities around 7.6 mAh/g. From cycle two, the charge and discharge capacities were reduced to and remained stable at around 2 mAh/g throughout the rest of the cycling. A figure presenting the cycling results for each of the different cells containing V_2C MXene insertion cathodes from Batch 2 and the APC-THF electrolyte can be found in Appendix B (figure B.4).

Figure 4.22 shows an example of typical cycling behaviour observed for the coin cells containing V_2C MXene insertion cathodes from Batch 2 and BMOC-DME electrolyte, after cycling with the standard cycling programme. The cells displayed initial voltages ranging from 1.7 to 2.0V prior to cycling, and initial discharge capacities between 12.2 to 15.5 mAh/g were observed. Afterthe first cycle, the charge and discharge capacities were reduced to approximately 1 mAh/g, and stabilised around 0.2 to 0.4 mAh/g for the remaining cycles. Noteworthy, one of the cells required 74 cycles before proper cycling behaviour was observed.

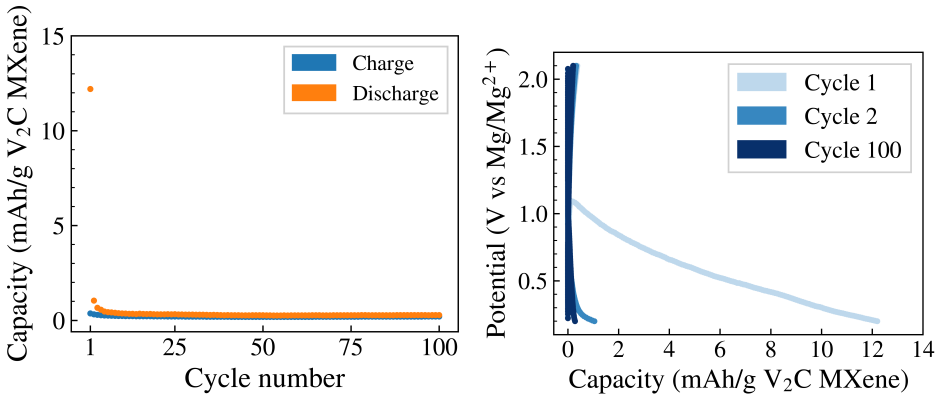

(a) (b)

Figure 4.22: Typical cycling performance and voltage profiles for the first, second, tenth and final cycle (counting from the first cycle where proper cycling behaviour was observed) for V_2C MXene insertion cathodes from Batch 2 with BMOC-DME electrolyte. The results were obtained for Mg/BMOC/V_2C-B2-1 cycled with the standard cycling programme.

In general, all the cells display sloping voltage profiles without any distinct charge or discharge plateaus. The results of the galvanostatic cycling is summarised in table 4.4, where the cathode loading, initial voltage and discharge capacity of cycle number 1, 2, 10 and 100 is given for each of the cycled cells. For the cells that required several cycles of charge and discharge before cycling properly, the first cycle is considered as the first successful discharge and charge cycle. Therefore, the discharge capacities for these cells are given with the cycle number in parentheses to emphasise the discrepancy in cycling behaviour.

Table 4.4: Overview of the results from the galvanostatic cycling of the cells containing V_2C MXene insertion cathodes that were cycled utilizing the standard cycling programme (0.2-2.1V, 10 mA/g, 100 cycles) and the extended cycling programme (0.01-2.1V, 10 mA/g, 100 cycles). In general, the discharge capacities are given for cycle number 1, 2, 10 and 100. However, for the cells requiring multiple cycles of charge and discharge before displaying proper cycling behaviour, the discharge capacities, starting from the first proper discharge and charge cycles, are given with the corresponding cycle number in parenthesis (*).

Cell ID	**Loading [mg/cm^2]**	**Initial voltage [V]**	**Discharge capacity [mAh/g]**			
			Cycle number			
			1.	2.	10.	100.
Standard cycling programme: 0.2-2.1V, 10 mA/g, 100 cycles						
Mg/APC/V_2C-B1-1	2.8	1.6	3.7	1.5	1.2	1.3
Mg/APC/V_2C-B1-2	2.9	1.6	3.8	1.6	1.2	1.4
Mg/APC/V_2C-B1-3	2.1	1.6	-	-	-	-
Mg/BMOC/V_2C-B1-1	2.1	1.5	3.8 (*52)	0.5 (*53)	0.2 (*62)	0.1 (*100)
Mg/BMOC/V_2C-B1-2	4.9	1.9	5.6 (*63)	0.6 (*64)	0.2 (*73)	0.2 (*100)
Mg/BMOC/V_2C-B1-3	3.0	1.9	4.8 (*68)	0.3 (*69)	0.1 (*78)	0.1 (*100)
Mg/APC/V_2C-B2-1	2.2	1.6	7.6	2.3	1.4	2.0
Mg/APC/V_2C-B2-2	2.2	1.8	7.6	2.1	1.2	1.7
Mg/APC/V_2C-B2-3	1.9	1.7	-	-	-	-
Mg/BMOC/V_2C-B2-1	1.7	1.7	12.2	1.0	0.4	0.3
Mg/BMOC/V_2C-B2-2	2.2	2.0	14.3	1.1	0.4	0.3
Mg/BMOC/V_2C-B2-3	2.5	2.0	15.5 (*74)	0.8 (*75)	0.2 (*84)	0.2 (*100)
Extended cycling programme: 0.01-2.1V, 10 mA/g, 100 cycles						
Mg/BMOC/V_2C-B1-4	3.6	1.9	11.0 (*12)	1.4 (*13)	0.4 (*22)	0.3 (*100)
Mg/BMOC/V_2C-B1-5	3.2	1.7	8.0 (*20)	1.2 (*21)	0.3 (*30)	0.2 (*100)
Mg/BMOC/V_2C-B1-6	3.1	1.8	11.3	1.8	0.4	0.3

Electrochemical impedance spectroscopy

Figures 4.23 and 4.24 display the capacities and voltage profiles recorded for the four coin cells subjected to electrochemical impedance spectroscopy measurements. The two cells containing V_2C MXene insertion cathodes from Batch 2 and APC-THF electrolyte display very similar electrochemical performances as the equivalent cells presented above; the cells displayed initial voltages of 1.5V prior to cycling, and initial discharge capacities of around 6.0-6.1 mAh/g. For the second cycle, the charge and discharge capacities were reduced to approximately 1.3 mAh/g, and in the remaining cycles the capacities were stable at values below 1 mAh/g. The two coin cells containing V_2C MXene insertion cathodes from Batch 2 and LiCl-APC-THF electrolyte displayed initial voltages of 1.8V, and initial discharge capacities of 150.5 and 131.5 mAh/g for Mg/LiCl-APC/V_2C-B2-1 and Mg/LiCl-APC/V_2C-B2-1, respectively. For the second cycle, a discharge capacity of 68.4 mAh/g was observed for Mg/LiCl-APC/V_2C-B2-1, and the capacity remained stable between 60 and 70 mAh/g until cycle number 40, where the cell was unable to reach the charge voltage of 2.1V and the cycling was stopped. For Mg/LiCl-APC/V_2C-B2-2 a discharge capacity of 57.7 mAh/g was observed for the second cycle, and the capacity remained stable until cycle number 16, where a sudden drop in capacity to approximately

10 mAh/g was observed (figure 4.24c). Rather low and unstable capacities were then observed for the following cycles, until the cell stabilised at discharge capacities between 50 and 70 mAh/g from cycle number 67 and onwards. After cycle number 92, the cell was unable to reach the charge voltage of 2.1V, and the cycling was stopped. Furthermore, the cells containing the LiCl-APC-THF electrolyte display sloping voltage profiles without distinct charge and discharge plateaus for all but the last cycle. In the final cycle of each cell, a distinct plateau around 2V is observed for the charge sequence. The results of the galvanostatic cycling of the four cells are summarised in table 4.5, where the cathode loading, initial voltage and discharge capacities for the first, second, tenth and final cycle is listed. For the cells that were not able to reach a hundred cycles, the discharge capacity of the final cycle is given with the cycle number in parenthesis.

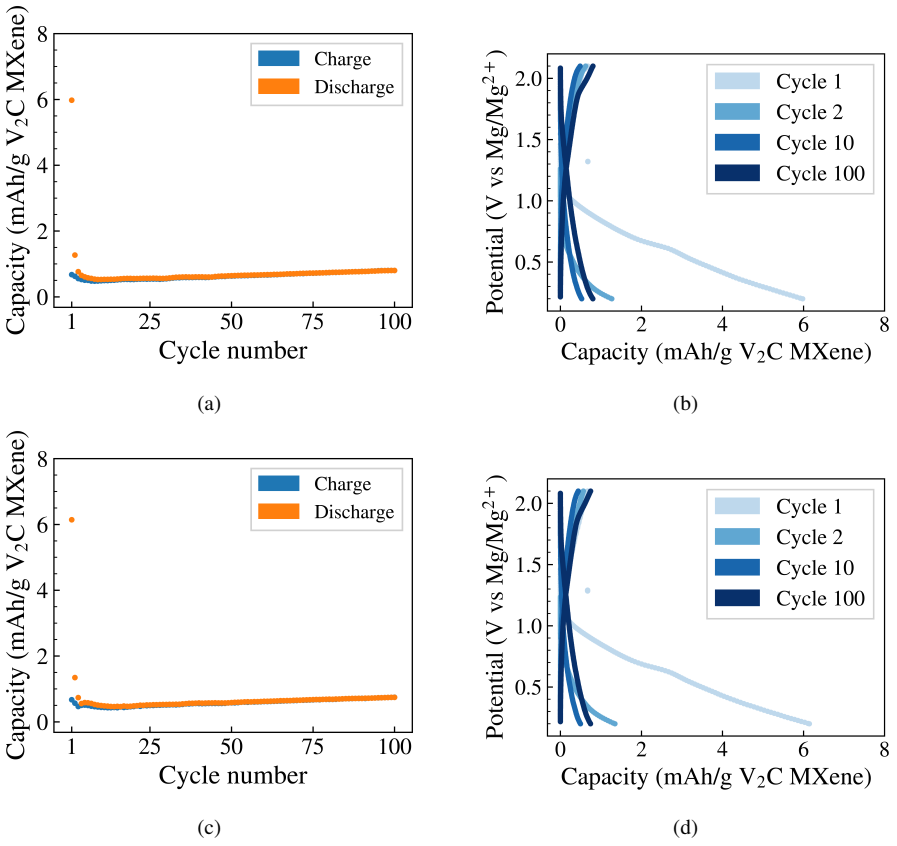

Figure 4.23: Overview of the discharge and charge capacities that were recorded during cycling and the voltage profiles recorded for cycle number 1, 2, 10 and 100 for Mg/APC/V_2C-B2-4 (a and b, respectively) and Mg/APC/V_2C-B2-5 (c and d, respectively).

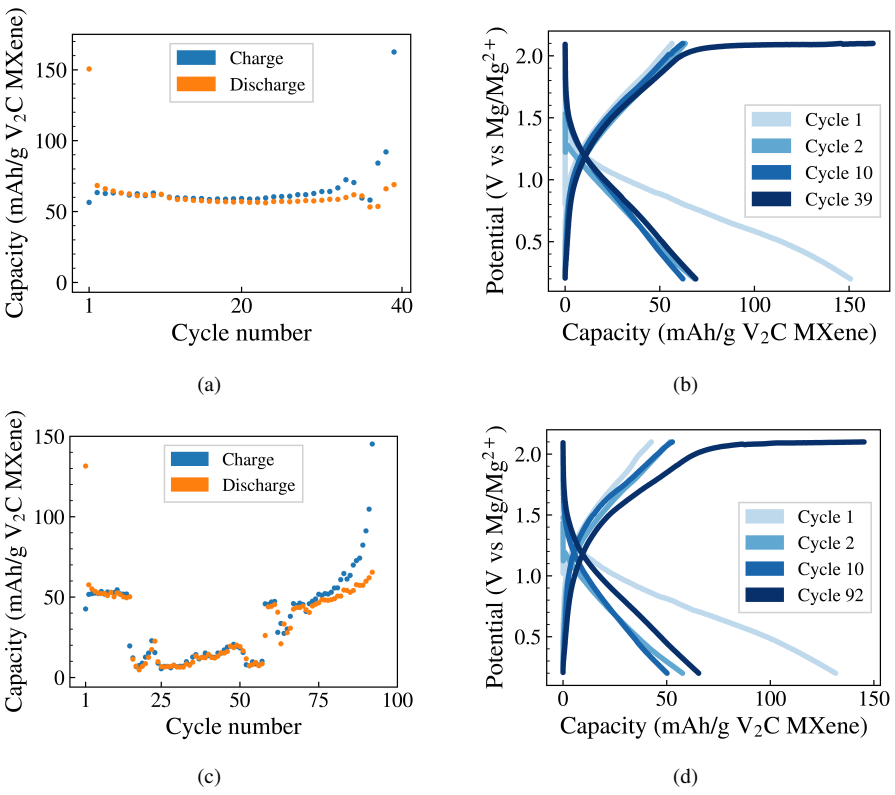

Figure 4.24: Overview of the discharge and charge capacities that were recorded during cycling and the voltage profiles recorded for the first, second, tenth and final cycle for Mg/LiCl-APC/V_2C-B2-1 (a and b, respectively), Mg/LiCl-APC/V_2C-B2-2 (c and d, respectively).

Table 4.5: Overview of the results from the galvanostatic cycling of the four coin cells that were subject to electrochemical impedance spectroscopy, where the cathode loading, initial voltage and discharge cycle for the first, second, tenth and final cycle. (*): For the cells that were rendered defective before completing the one hundred planned cycles, the discharge of the final successful cycle is given in the "100." column, with the corresponding cycle number given in parenthesis.

Cell ID	**Loading [mg/cm^2]**	**Initial voltage [V]**	**Discharge capacity [mAh/g]**			
			Cycle number			
			1.	2.	10.	100.
Electrochemical impedance spectroscopy (Standard cycling programme: 0.2-2.1V, 10 mA/g, 100 cycles)						
Mg/APC/V_2C-B2-4	1.9	1.5	6.0	1.3	0.5	0.8
Mg/APC/V_2C-B2-5	1.9	1.5	6.1	1.3	0.5	0.7
Mg/LiCl-APC/V_2C-B2-1	2.2	1.8	150.5	68.4	62.2	69.0 (*39)
Mg/LiCl-APC/V_2C-B2-2	2.6	1.8	131.5	57.7	50.2	65.4 (*92)

The results of the electrochemical impedance spectroscopy measurements that were performed on the four coin cells are presented in figures 4.25 and 4.26. For the impedance measurements conducted on the cells after one cycle (figure 4.25), two semicircles can be observed in the plots; one rather small semicircle recorded at high frequencies and one larger semicircle measured at lower frequencies. The inset in figure 4.25 focuses on the smaller semicircle located at lower impedance values. Noteworthy, the diameter of the semicircles for the cells utilizing the LiCl-APC-THF electrolyte is significantly smaller than for the cells utilizing the APC-THF electrolyte. Furthermore, the impedance measurements conducted on the coin cells containing the APC-THF electrolyte after one hundred cycles (figure 4.26) display semicircle shapes similar to the ones observed after one cycle. The impedance measurements of the coin cells containing LiCl-APC-THF electrolyte, conducted after the cycling of the cells were stopped, do not display any distinct semicircles.

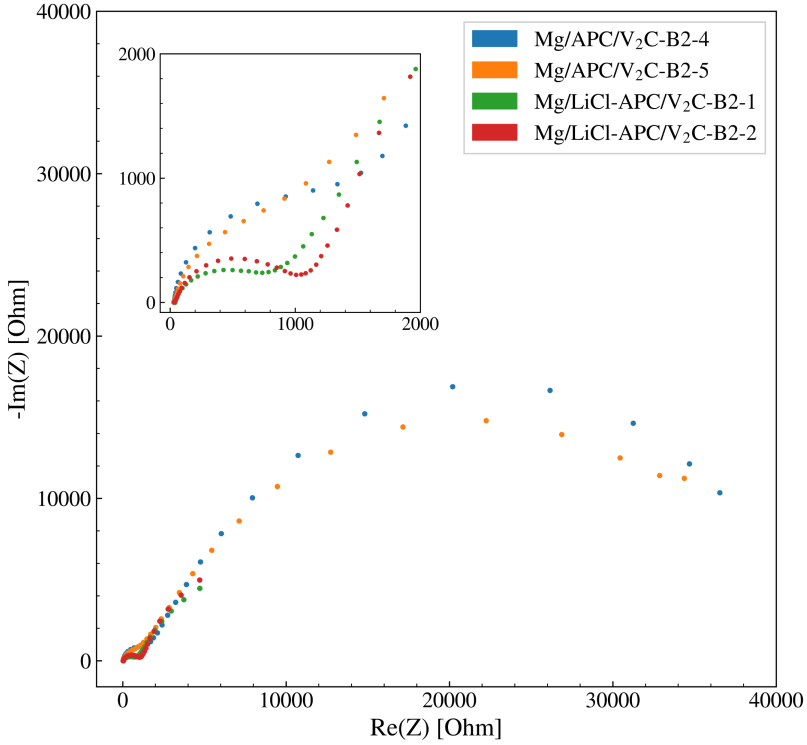

Figure 4.25: Electrochemical impedance spectroscopy of Mg/APC/V_2C-B2-4, Mg/APC/V_2C-B2-5, Mg/LiCl-APC/V_2C-B2-1 and Mg/LiCl-APC/V_2C-B2-2 performed after one cycle with the standard cycling programme. The inset focuses on the smaller semicircles observed at lower impedance values.

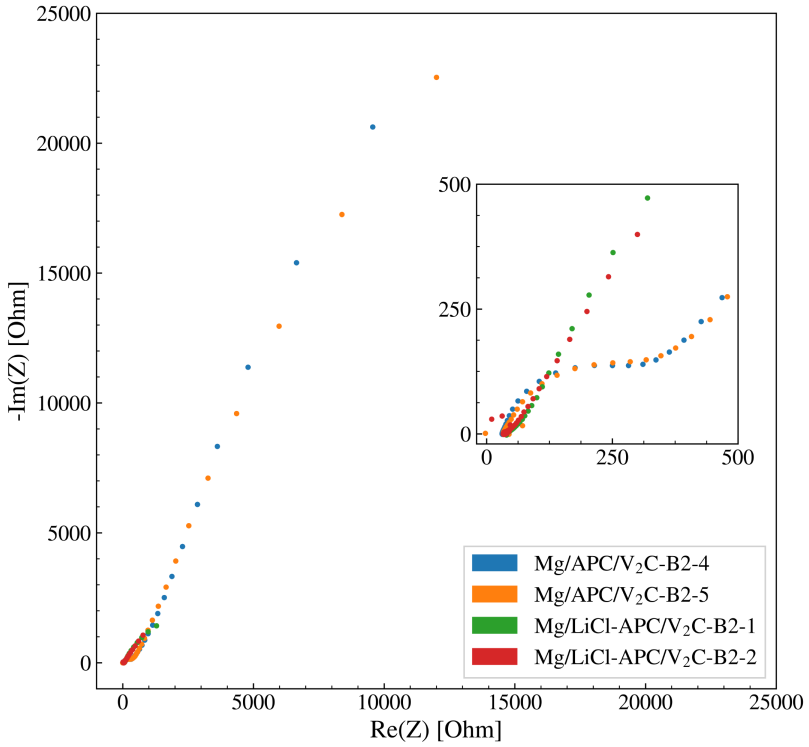

Figure 4.26: Electrochemical impedance spectroscopy of Mg/APC/V_2C-B2-4, Mg/APC/V_2C-B2-5, Mg/LiCl-APC/V_2C-B2-1 and Mg/LiCl-APC/V_2C-B2-2 performed after the final cycle with the standard cycling programme. The inset focuses on the smaller semicircles observed at lower impedance values.

4.2.2 V_2C-S conversion cathodes

Galvanostatic cycling

Figure 4.27 presents the results from the galvanostatic cycling of the three electrode cell, Mg/BMOC/V_2C-S-3-Electrode, that was discharged to 0.4V and charged to 2.1V at a constant current rate of 10 mA/g. An initial voltage of 1.1V and a relatively high initial discharge capacity of 312.4 mAh/g was observed for the cell. In the subsequent charge cycle, the charge capacity was only 37.2 mAh/g, and the discharge capacity was drastically reduced to 24.9 mAh/g in the second cycle and to 4.0 mAh/g in the tenth cycle. As no clear charge plateau was observed for the voltage profiles (figure 4.27b, 4.27c, 4.27d and 4.27e) the cycling was stopped after the tenth cycle, and continued with an increased upper cutoff voltage of 2.3V. With this extended cycling voltage window, a discharge capacity of only 3.5 mAh/g was observed for the first cycle (figure 4.28), and for the following charge sequence the cell displayed a very large charge plateau of approximately 3000 mAh/g initiated at a voltage slightly above 2.2V (figure 4.28b). In the second cycle a discharge capacity of 78.0 mAh/g was observed, but the following charge sequence displayed a charge capacity of only about 20 mAh/g. After ten cycles the discharge capacity was reduced to 10.1 mAh/g, and similar capacities were observed for the remaining cycles as well.

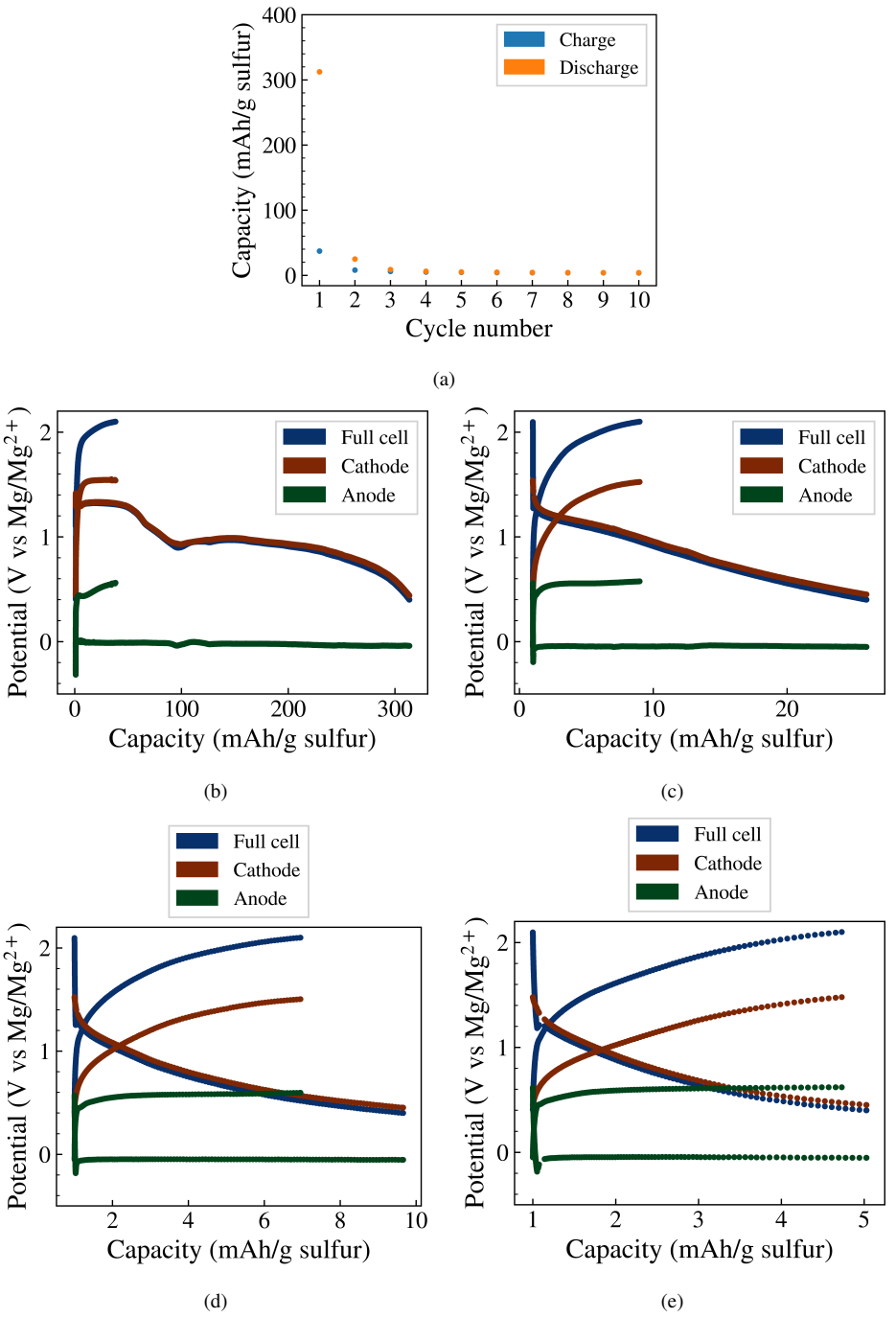

Figure 4.27: (a) Capacity vs cycle number for the galvanostatic cycling of the Mg/BMOC/V_2C-S-3-Electrode cell when cycled between 0.4 and 2.1V, and voltage profiles of the first (b), second (c), third (d) and tenth (e) cycle.

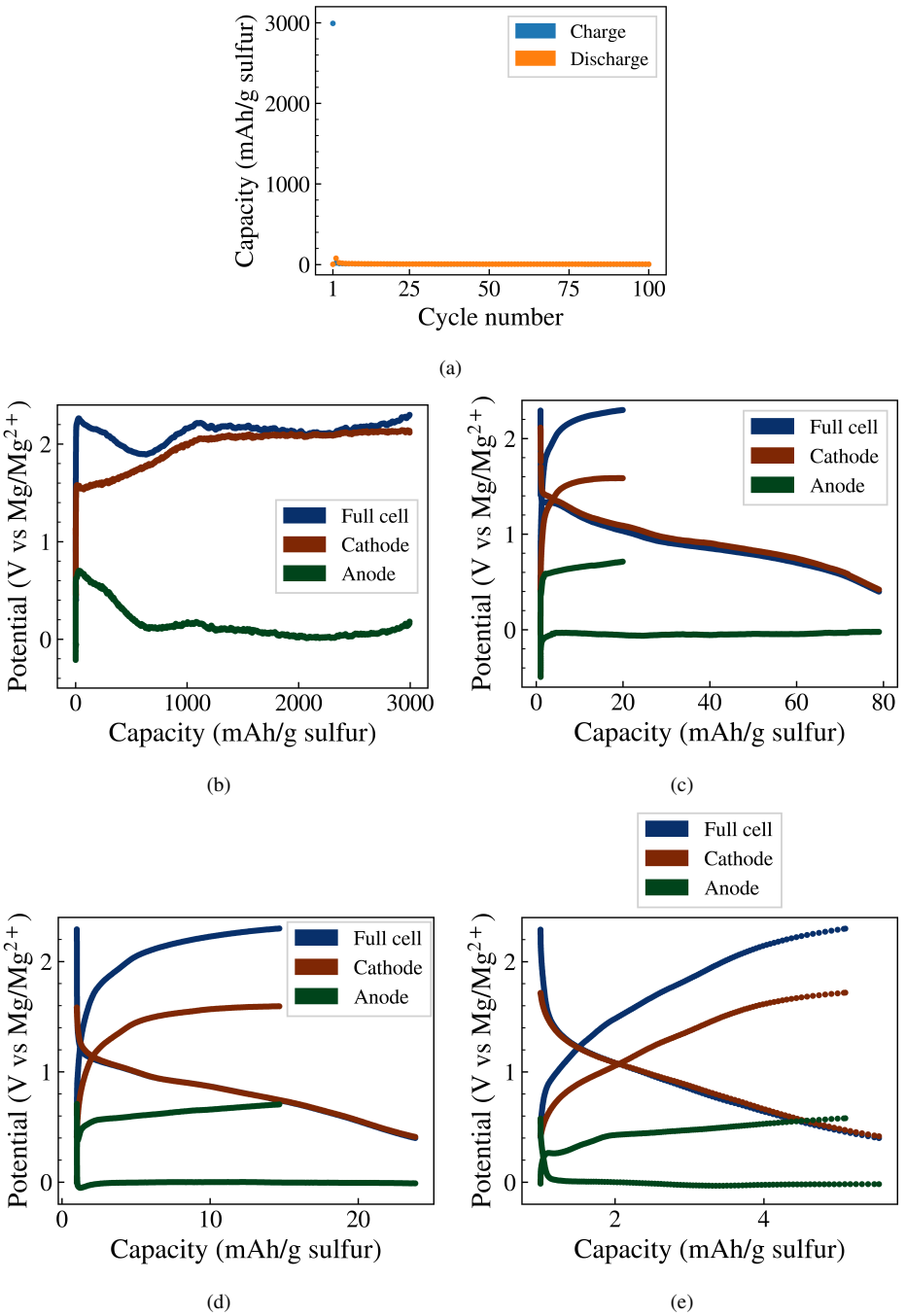

Figure 4.28: (a) Capacity vs cycle number for the galvanostatic cycling of the Mg/BMOC/V_2C-S-3-Electrode cell when cycled between 0.4 and 2.3V, and voltage profiles of cycle one (b), two (c), three (d) and hundred (e).

The capacities and voltage profiles resulting from the galvanostatic cycling of the coin cells containing Li anodes, V_2C-S conversion cathodes and Li(TFSI)-$LiNO_3$-DOL-DME electrolyte are presented in figure 4.29. Initial voltages of 2.5 and 2.4V and first cycle discharge capacities of 594.3 and 602.8 mAh/g were observed for Li/Li(TFSI)/V_2C-S-1 and Li/Li(TFSI)/V_2C-S-2, respectively. One of the cells, Li/Li(TFSI)/V_2C-S-1, displayed a discharge capacity of 485.4 mAh/g in the second cycle and stabilised around 435.2 mAh/g after the tenth cycle. The cell continued to cycle in a stable fashion for about 200 cycles, whereafter a more unstable cycling behaviour with increasing charge capacities and decreasing discharge capacities was observed(figure 4.29a). After 492 cycles the cell was unable to reach the charge voltage and the cycling programme was stopped. Moreover, the second cell displayed a discharge capacity of 502.2 mAh/g in the second cycle and 460.9 mAh/g after the tenth cycle. The discharge capacity remained stable around 450 mAh/g for about 450 cycles, after which a slow decrease in the capacity was observed with cycling. The cycling was abruptly stopped after cycle number 579, when the cell proved unable to reach the charge voltage. Moreover, the voltage profiles of the two cells display a distinct charge plateau starting at approximately 2.2V, and two significant discharge plateaus at approximately 2.35 and 2.05V.

A summary of the galvanostatic cycling results of the three electrode cell and the two Li-based cells is presented in table 4.6, where the cathode loading, initial voltage and discharge capacity of the first, second, tenth and final cycle is given for each of the cells. For the Li-based cells that were cycled until failure, the discharge capacity of the final successful cycle is given with the corresponding cycle number in parenthesis.

Table 4.6: Overview of the results from the galvanostatic cycling of the cells containing V_2C-S conversion cathodes. Note that the Li cells were cycled until failure and the discharge capacity of the final cycle is given with the corresponding cycle number in parenthesis (*).

Cell ID	**Loading [mg/cm^2]**	**Initial voltage [V]**	**Discharge capacity [mAh/g]**				
			Cycle number				
			1.	2.	10.	100.	
Three electrode setup: 0.4-2.1V, 10 mA/g, 10 Cycles							
Mg/BMOC/V_2-S-3-Electrode	0.8	1.1	312.4	24.9	4.0	-	
Three electrode setup: 0.4-2.3V, 10 mA/g, 100 Cycles							
Mg/BMOC/V_2-S-3-Electrode	0.8	1.1	3.5	78.0	10.1	4.5	
Li-systems for reference: 1.8-2.8V, 837.5 mA/g, Cycled until failure							
			Cycle number				
			1.	2.	10.	100.	Final (*)
Li/Li(TFSI)/V_2-S-1	0.8	2.5	594.3	485.4	435.2	405.8	331.5 (492)
Li/Li(TFSI)/V_2-S-2	0.6	2.4	602.8	502.2	460.9	458.0	399.5 (579)

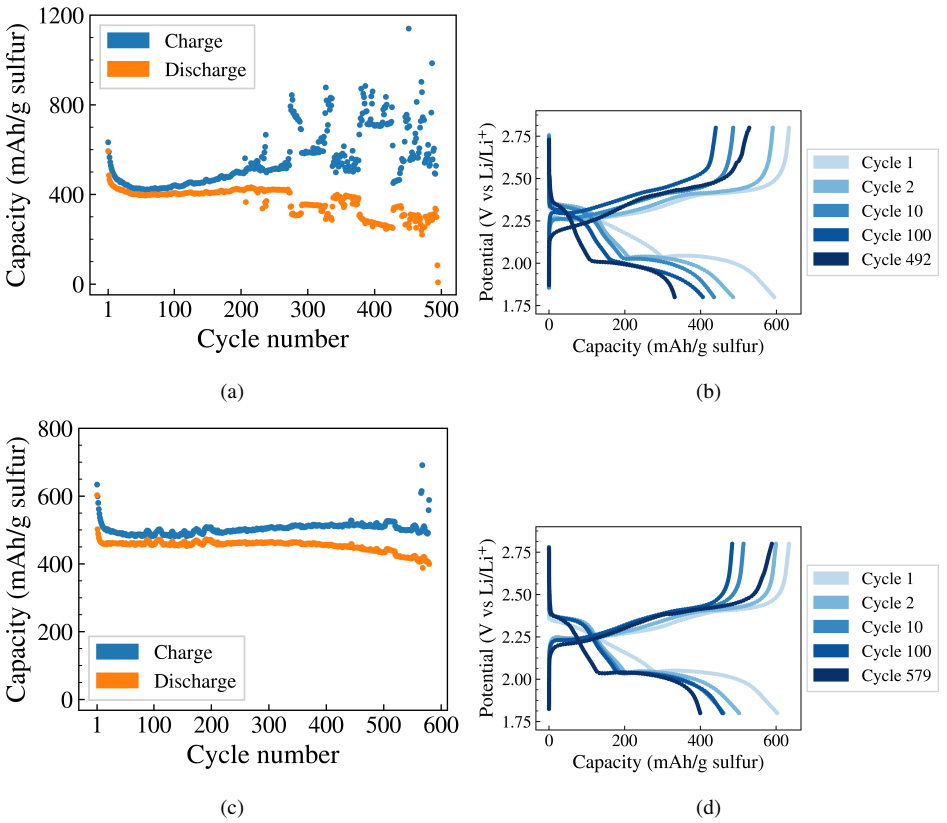

Figure 4.29: Overview of the discharge and charge capacities that were recorded during cycling and the voltage profiles recorded for cycle 1, 2, 10, 100 and the final cycle for Li/Li(TFSI)/V_2C-S-1 (a and b, respectively), Li/Li(TFSI)/V_2C-S-2 (c and d, respectively).

Rate capability test

Figure 4.30 presents the results of the rate capability test performed on the two coin cells containing V_2-S conversion cathodes and BMOC-DME electrolyte; Mg/BMOC/V_2-S-1 and Mg/BMOC/V_2-S-2. Both cells display decreasing capacities with increasing current rates, starting at approximately 20-30 mAh/g for a current rate of 10 mA/g and then being reduced to 10-20 mAh/g for 25 mA/g, 5-10 mAh/g for 50 mA/g and close to zero capacity for 100 mAh/g. In the final step of the rate test, where the current rate was reduced from 100 mA/g to the initial value of 10 mA/g, both cells appeared to regain the capacity that was lost when cycling at higher currents.

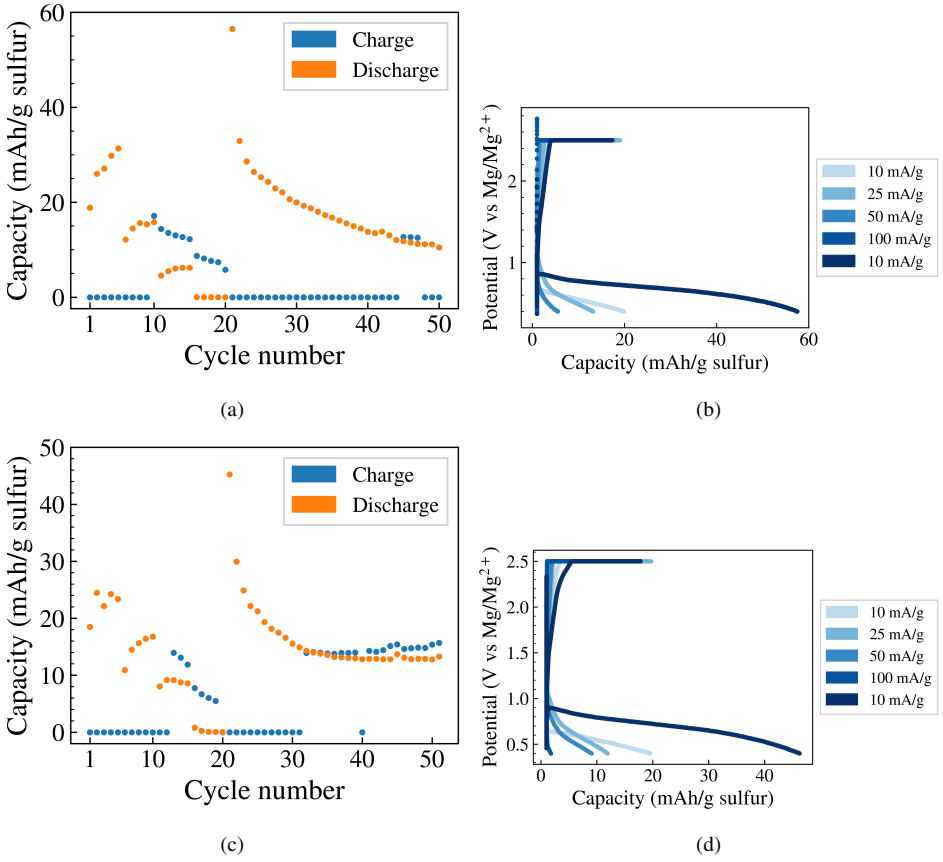

Figure 4.30: Overview of the discharge and charge capacities that were recorded during rate capability testing and the voltage profiles recorded for the first cycle of each current-step in the test for Mg/BMOC/V_2C-S-1 (a and b, respectively), Mg/BMOC/V_2C-S-2 (c and d, respectively).

4.3 Post mortem characterization

Morphology and elemental detection

Figure 4.31 presents an overview of the Mg anode, separator, gold current collector and upper plunger retrieved from the three electrode cell after cycling, as well as the results of the elemental mapping performed on the side of the Mg anode that was in contact with the current collector during cycling. A brown residue from the cycling process was observed on all four cell constituents, and a number of black spots was seen on the edge of the Mg anode. These black spots are observed in the rightmost part of the SEM image of the anode surface (figure 4.31b) as small lumps of unknown material deposited on the otherwise flat surface. The mapping results indicate that the black spots observed on the anode surface contain significant amounts of sulfur and oxygen (figure 4.31d and 4.31e, respectively), as well as some carbon (figure 4.31f). Moreover, the mapping of magnesium (figure 4.31c) indicates that the black spots observed on the anode does not contain any significant amount of magnesium, and that the layer of the unknown material is thick enough to shield the underlying magnesium metal from the EDX measurements. Area scans performed of the anode on the side that was in contact with the current collector during cycling show significant amounts of carbon and oxygen on the anode, as well as smaller amounts of fluorine and sulfur (table 4.7).

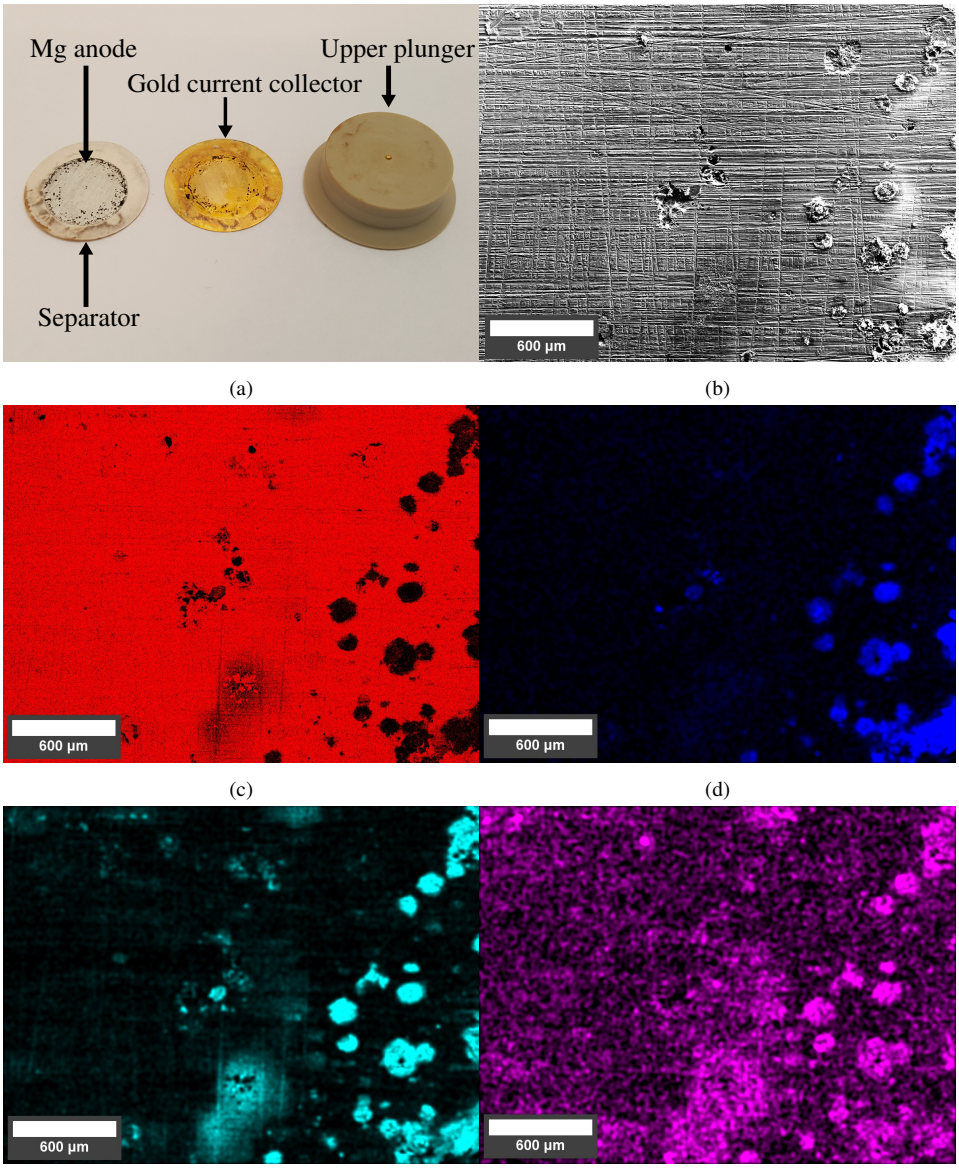

Figure 4.31: (a) Overview of the Mg anode, separator, gold current collector and upper plunger that was retrieved after disassembly of the three electrode cell (Mg/BMOC/V_2-S-3-Electrode) that had been cycled for a total of 110 cycles. (b) SEM image of the side of the Mg anode that was in contact with the gold current collector during cycling, and elemental mapping of the elements present on the depicted area: (c) Mg, (d) S, (e) O and (f) C.

The SEM images captured of the side of the Mg anode that was in contact with the separator during cycling is presented in figure 4.32. In the overview image seen in figure 4.32a, residues from the separator is observed on the anode surface, and a closer view of the surface is provided in figure 4.32b. Additionally, the two separate areas that were subject to EDX area scans are marked by coloured rectangles, where the red rectangle indicates the location of area number one and the blue rectangle indicates the location of area number two. The resulting EDX spectra are presented in figure A.3 (Appendix A). The EDX measurements presented in table 4.7 indicate the presence of a range of different elements on the anode surface; significant amounts of carbon, oxygen, magnesium and boron, and trace amounts of aluminium, fluorine, sulfur, silicon, sodium, potassium, calcium, chlorine and titanium.

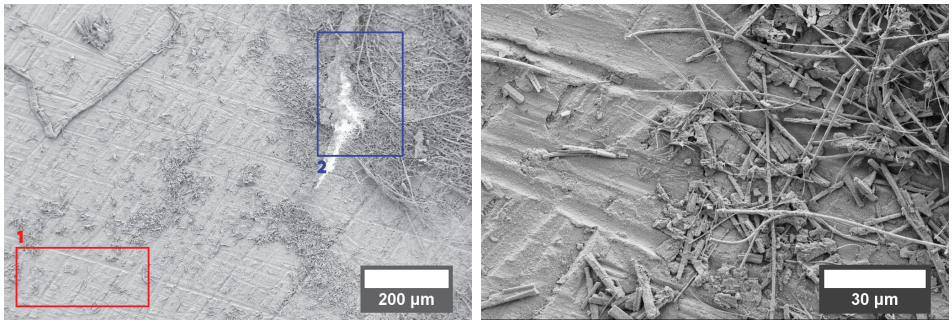

(a) (b)

Figure 4.32: SEM images captured of the Mg anode that was retrieved from the three electrode cell after cycling. (a) Overview of the side of the anode that was in contact with the separator during cycling, with the two areas subjected to EDX area scans indicated by coloured rectangles. (b) High magnification image of the cycled anode, showing residues from the separator on the anode surface.

In figure 4.33, an image of the separator and the Mg anode side facing the separator is presented, as well as a SEM image of the cycled separator. The faces of the separator and anode that are visible in the image (figure 4.33a) were in contact during cycling, and a large piece of the separator is adhered to the Mg anode after separation of the two components. Discolouration of the separator can be observed both around the rim of the separator, which interestingly marks the area that was not covered by the anode during cycling. Additionally, there is some discolouration in the center of the separator, which can also be observed on the part of the separator that is adhered to the anode. The EDX measurements that were performed on both sides of the separator indicate the presence of a large range of elements: aluminium, carbon, oxygen, fluorine, sulfur, magnesium, silicon, sodium, boron, potassium, calcium, titanium and zinc. Noteworthy, the atomic percentages of the different elements appear to be rather similar for the two sides (table 4.7). The EDX spectra resulting from the area scans of the separator are presented in figure A.4 (Appendix A).

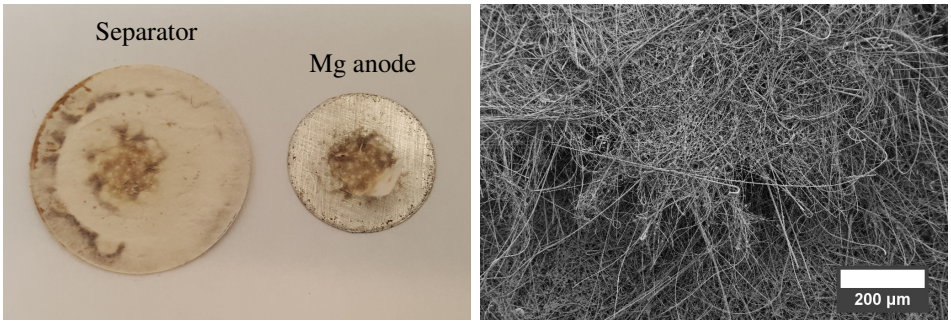

(a) (b)

Figure 4.33: (a) Image of the separator and Mg anode that was retrieved from the cycled three electrode cell (Mg/BMOC/V_2-S-3-Electrode), showing the two sides that were in contact during cycling. A part of the separator can be observed adhered to the centre of the anode disk. (b) SEM image of the cycled separator showing the glass fibre threads making up the separator structure.

Figure 4.34 presents the SEM images captured of an uncycled V_2C-S cathode and the cycled V_2C-S conversion cathode retrieved from the cycled three electrode cell. The images captured after cycling reveal a large amount of cracks in the cathode surface, as well as some glass fibres from the separator. In the high magnification image (figure 4.34d), the area that was subject to the EDX scan is indicated by a red rectangle. The results from the EDX measurement are included in table 4.7 and indicate the presence of vanadium, aluminium, carbon, oxygen, fluorine, sulfur and magnesium in the cathode.

Table 4.7: Overview of the results from the post-mortem EDX characterization of the anode, separator and cathode retrieved from the cycled three electrode cell (Mg/BMOC/V_2-S-3-Electrode). The elemental ratios are given in atomic percent for each of the samples. ”-” indicates that the given element was not detected in the specific sample.

Sample	**Element [at.%]**														
	V	Al	C	O	F	S	Mg	Si	Na	B	K	Ca	Cl	Ti	Zn
Anode (current collector side)	-	-	12.7	12.0	0.5	0.8	74.0	-	-	-	-	-	-	-	-
Anode (separator side, Area 1)	-	0.4	16.9	27.4	0.5	1.1	14.7	2.6	1.0	34.8	0.1	0.6	<0.1	<0.1	-
Anode (separator side, Area 2)	-	0.2	-	6.3	0.1	0.3	61.8	0.3	0.6	30.1	<0.1	<0.1	0.2	<0.1	-
Separator (anode side)	-	1.8	3.8	41.4	0.7	1.2	4.8	15.6	4.8	22.4	1.1	0.7	-	0.8	0.9
Separator (cathode side)	-	1.7	4.4	41.8	0.7	0.4	4.5	15.3	4.7	23.2	1.1	0.7	-	0.7	0.9
Cathode	9.4	1.6	42.8	18.5	13.2	1.7	12.8	-	-	-	-	-	-	-	-

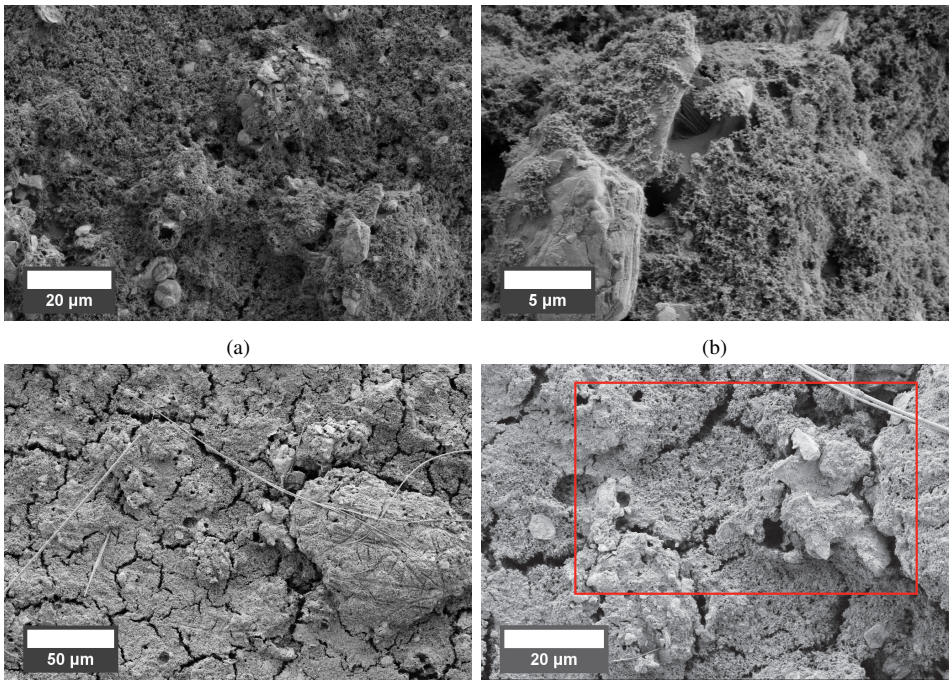

(a) (b)

(c) (d)

Figure 4.34: SEM images of an uncycled V_2C-S cathode and the cycled V_2C-S cycled cathode retrieved after disassembly of the three electrode cell (Mg/BMOC/V_2-S-3-Electrode). (a) Overview and (b) high magnification images of the uncycled cathode. (c) Overview of the cathode surface revealing a number of large cracks in the cathode surface, as well as glass fibres from the separator. (d) High magnification image of the cycled conversion cathode with the area subjected to an EDX area scan marked (red rectangle)

Chapter 5

Discussion

5.1 Overview

This section is divided into four main parts. In the first part, the synthesis of the V_2C MXene, including the optimization of milling and etching parameters, is discussed, with focus on phase purity and particle size distribution. In the second part, the electrochemical characterization of the insertion cathodes is discussed. Similarly, in the third part, the electrochemical and post-mortem characterization of the conversion cathodes is discussed. Finally, in the fourth part, the suitability of V_2C MXene as a constituent in different cathode designs for RMBs is evaluated.

5.2 V_2C MXene synthesis

5.2.1 V_2AlC MAX phase synthesis

Phase purity

The XRD results presented in section 4.1.1 indicate that the syntheses of the two separate V_2AlC MAX phase batches were partially successful, although with varying phase purities of approximately 79.7 and 90.3% for Batch 1 and Batch 2, respectively. This suggests that the synthesis route utilized is suboptimal, and that the formation of secondary phases is a significant challenge. As the main goal of this work was to explore V_2C MXene as a constituent in different cathode designs for RMBs, the presence of approximately 5.7% of the secondary V_4AlC_3 MAX phase in Batch 1 is undesirable. As the secondary MAX phase is expected to be converted to V_4C_3 MXene during the etching step[2,103], the resulting powder will contain two different types of MXene, instead of only the desired V_2C MXene. Since the unwanted MAX phase was formed only in Batch 1 and not in Batch 2, despite the same synthesis route being utilized for both batches, it is reasonable to suggest that the unwanted MAX phase results from a discrepancy in one or more of the steps in the synthesis of Batch 1. Based on the difference in stoichiometry between the V_2AlC MAX

phase and the V_4AlC_3 MAX phase, one possible explanation of the formation of V_4AlC_3 may be local concentration differences within the powder mixture prior to or during sintering. Inhomogeneous mixing of the powders during the ball milling procedure and/or powder separation during the evaporation of the isopropanol in the following synthesis step, may lead to the molar ratio of vanadium, aluminium and carbon to deviate from the intended ratio of 2.00:1.30:1.00 in some parts of the powder mixture. Additionally, evaporation of non-negligible amounts of aluminium during the sintering at 1500 °C may also explain variations in the stoichiometry of the powder mixture, as the continuous flow of argon during the synthesis will remove gaseous species from the reaction chamber. Another possible explanation of the secondary V_4AlC_3 MAX phase formation can be a suboptimal molar ratio for the metal powder precursors. In a similar work, Hu et al.[110] reported on single phase synthesis of V_2AlC by utilizing a molar ration of 2.0:1.2:0.9 for vanadium, aluminium and carbon in a synthesis route similar to the one used in this work. This does not fully explain why the secondary MAX phase was formed for only Batch 1 when the exact same molar ratio between the precursors was used for both batches, but it may still indicate that the molar ratio can be further optimized.

Both MAX phase batches were found to contain significant amounts of Al_2O_3, despite extensive efforts to minimize the exposure of the precursor mixture to ambient air. However, there are several possible explanations for the observed oxide, with the first one being the oxidation of the powder precursor mixture after the evaporation of isopropanol in the rotavapor. As mentioned in section 3.2.1, the rotavapor flask containing the powder mixture is partially submerged in a water bath at 50 °C during evaporation, resulting in heating of the flask and powder mixture inside. Therefore, following the completion of the evaporation step, the elevated temperature of the flask and powder mixture may promote the oxidation of the metallic powders when the inside of the flask is exposed to ambient air during venting. Furthermore, the relatively time consuming pellet pressing procedure is performed in ambient air, which could be another source of oxygen exposure, either due to oxidation of the metallic powders or due to absorption of water from the air. Another possible explanation for the formation of Al_2O_3 can be the presence of oxygen in the tube furnace during sintering, which could either be due to inefficient argon flushing of the furnace prior to heating and/or a potential leak in the furnace allowing air to seep in.

In addition to the secondary phases discussed above, a significant amount of Al_4C_3 was present in Batch 1, and a comparably large amount of VAl_3 was formed in Batch 2. These aluminium-rich impurity phases have previously been observed in similar works[98,110], and one possible explanation for their presence is the excess of aluminium in the molar ratio utilized. A possible solution to reduce the amount of secondary phases containing aluminium is therefore to reduce the molar ratio of aluminium slightly.

Particle size and morphology

The particle size distribution measured for Batch 1 (figure 4.7) indicates that the downsizing by mortar and pestle resulted in a rather broad size distribution. Noteworthy, although a sieve with pore size 44 μm was utilized in the downsizing procedure, particles of sizes

up to about 100 μm appeared to be present in the sample. This can be attributed to two separate aspects. First, particles that are larger than the pore size in one dimension may still pass through the sieve. Second, the laser diffraction technique utilized to measure the particle size distributions assumes spherical particles, and from the SEM images (figure 4.8a and 4.8a) it becomes clear that this is not the case for the MAX phase powder. Thus, the particle size distribution extending beyond the pore size of the sieve is probably due to a combination of larger particles passing the sieve and a certain error in the measurements due to non-spherical particles.

For Batch 2, the downsizing by planetary milling (figure 4.9) at 300 RPM and 400 RPM resulted in particle size distributions with considerably lower mean values than what was achieved for Batch 1. The milling at the higher milling speed of 400 RPM was observed to produce particles of generally smaller size than the milling at the lower milling speed of 300 RPM, which is consistent with the additional energy available to break apart the particles at higher milling speeds. Moreover, the discrepancy observed in the pristine samples presented in figure 4.9c and 4.9d can be attributed to to the fact that the sintered pellets from Batch 2 were lightly crushed in a mortar and pestle in two separate portions prior to milling, resulting in slightly different particle size distributions for the two different portions. In other words, the pellets used for the milling at 400 RPM had been ground down more thoroughly than the pellets used for the milling at 300 RPM prior to the planetary milling. However, considering the rather effective downsizing during the first ten to thirty minutes of the two milling procedures (figure 4.9a), the size difference of the pristine samples is not believed to affect the milling results significantly.

Furthermore, a significant amount of WC was observed in the XRD results and EDX measurements of the sample milled at 400 RPM. This is believed to originate from the milling balls and/or jar that were made from WC, as it is reasonable to argue that the excess energy provided at the milling speed of 400 RPM resulted in the milling equipment being wore down and contaminating the sample. Trace amounts of WC was measured in one of the EDX point measurements of the sample that was milled at 300 RPM, but there were no visible WC diffraction lines in the XRD spectrum of this sample, thus the amount of WC is considered to be negligible. An additional observation that is worth mentioning is the peak broadening seen in the XRD spectra of the milled samples (figure 4.3), which can be attributed to the reduced crystallite sizes and introduction of strain within the particles, due to the milling procedures.

5.2.2 Etching of MAX phase

Effects of particle size and etching duration

The XRD results for Batch 1 (figure 4.1) indicate the successful conversion of V_2AlC MAX phase to V_2C MXene, as a characteristic diffraction line corresponding to V_2C MXene appear at a 2Θ value of 11.2° in the etched sample. However, the diffraction lines corresponding to V_2AlC are still present at relatively strong intensities after etching with 48% HF for 96h, suggesting incomplete etching of the MAX phase particles. This

would further suggest that despite a rather harsh etching regime, the etching duration was insufficient for the etchant molecules to diffuse into the whole bulk of the particles and completely exfoliate the aluminium monolayers. Noteworthy, the diffraction line corresponding to V_4C_3 appearing after etching suggest that the unwanted V_4AlC_3 MAX phase observed prior to etching had been partially exfoliated, resulting in a powder that contains both V_2C and V_4C_3 MXene. This is an undesirable result as the main goal of this work was to investigate the suitability of V_2C MXene as cathode material in RMBs, and the V_4C_3 MXene is expected to contribute to the observed results. Furthermore, the particle size distribution measured after etching showed particles of generally smaller sizes than prior to etching, which is somewhat counter intuitive as the layered particles are expected to swell when the aluminium monolayers are removed, due to the formation of termination groups and hydrogen gas during etching. However, as mentioned in section 2.3.2, complete dissolution of the MAX phase particles during etching have been reported for experiments utilizing high concentrations of HF and long etching durations[82], which suggest that the HF etchant is not fully selective towards the transition metal layers. Therefore, the decrease in particle size observed after etching may be due to partial etching of the transition metal layers, in addition to the removal of the aluminium monolayers. Unfortunately, the secondary phases identified in the MAX phase powder prior to etching appear to be unaffected by the etching procedure and are found to be present in the etched sample as well.

Given the short etching time of 8h reported by Naguib et al. for attrition milled V_2AlC[25], etching durations of 48h and 96h for the powder milled at 300 RPM and 24h and 48h for the powder milled at 400 RPM were chosen, in an attempt to find an optimal combination of particle size and etching duration. For the powder milled at 300 RPM, the XRD results of the etched samples (figure 4.4) confirm the formation of V_2C MXene for both the sample etched for 48h and the sample etched for 96h. Interestingly, in the sample etched for 96h, the (0002) diffraction line corresponding to the V_2AlC MAX phase is not present, suggesting a complete conversion of the MAX phase to MXene. In the sample etched for 48h, the (0002) diffraction line is still present, but with a relatively low intensity. Thus, the etching time of 48h appear to be insufficient for the complete exfoliation of the aluminium monolayers from the MAX phase particles. These results are supported by the EDX measurements presented in table 4.3, as the measured values for aluminium are significantly lower for the etched samples compared to the milled sample prior to etching. Additionally, both samples are observed to contain significant amounts of oxygen and fluorine after etching, which can be attributed to the formation of surface termination groups on the MXene surface. Moreover, the decrease in mean particle size for the sample etched for 96h can be attributed to a partial etching of the transition metal layers as well as the exfoliation of the aluminium monolayers, following the same reasoning as for Batch 1. The slight increase in mean particle size observed for the sample etched for 48h is rather unexpected in light of the results obtained for the sample etched for 96h. Considering that the particle size distribution measurement technique assumes spherical particles, the increase can possibly be attributed to a measurement error, as the SEM images (figure 4.12a and 4.12b) clearly show that the particles are not spherical. An alternative explanation may be that the initial increase in particle size observed after 48h of etching is attributed to swelling of the

particles, and that the subsequent reduction in particle size observed after 96h of etching is attributed to the undesired etching of the transition metal layers as well. This should be further investigated before a conclusion can be drawn. It is also worth noting that similar to Batch 1, the secondary phases observed in the MAX phase powder prior to etching were also present after etching.

For the powder milled at 400 RPM, the XRD results of the etched samples (figure 4.5) indicate the successful formation of V_2C MXene for both the sample etched for 24h and the sample etched for 48h. Interestingly, the diffraction lines corresponding to the V_2AlC MAX phase are present in the samples after etching, implying that both etching durations were insufficient for the complete exfoliation of the particles. This is further supported by the EDX measurements performed on particles from the two samples (table 4.3), as the aluminium content in the two samples is relatively low, but not negligible. Similarly to the samples described in the previous paragraph, the etched samples of the powder milled at 400 RPM contain significant amounts of oxygen and fluorine, which is attributed to the formation of surface termination groups. Additionally, the impurity phases that were observed for the milled powder prior to etching, including the WC impurity, are also present in both the etched samples, suggesting that the secondary phases were not dissolved by the HF. Surprisingly, bimodal particle size distributions were observed for both of the etched samples, which is in clear contrast to the unimodal distribution measured for the milled power prior to etching. In both samples, the peak corresponding to the lower particle sizes is consistent with a decrease in mean particle size compared to the sample prior to etching, similar to what was observed for the sample milled at 300 RPM and etched for 96h. The peaks corresponding to the larger particle sizes in the two bimodal distributions represent particles that have a mean size of more than one order of magnitude larger than the sample measured prior to etching. This observation can be attributed to agglomerated particles that were not broken apart during the sonication step of the particle size distribution measurements. The SEM images of the two powder samples (figure 4.13) partially substantiates this explanation, as a number of small agglomerates are visible.

All in all, the combination of milling at 300 RPM for 6h and etching for 96h in 48% HF was found to give the highest conversion of V_2AlC MAX phase to V_2C MXene of all the explored parameter combinations. Additionally, of the milled powders, the powder milled at 300 RPM resulted in the largest particles, which is favourable when investigating intercalation of species into the bulk, contrary to surface reactions. Based on this, the powder that was milled at 300 RPM and etched for 96h was chosen for further characterization in V_2C MXene insertion cathodes, together with the powder from Batch 1. The reason for using one powder from each batch was to be able to compare the effects of particle size and phase purity on the electrochemical performance of the MXene cathodes.

Preparation of V_2C-S composite

The XRD results presented in figure 4.6 indicate that the sulfur is present in the composite structure in its crystalline state, as the diffraction lines corresponding to crystalline sulfur are observed in the diffractogram. In a similar work by Zhao et al.[24], a Ti_3C_2-S composite was produced by melt diffusion at 155° for 24h, and the resulting material was suggested

to contain sulfur in both a crystalline and non-crystalline state; the sulfur adhering to the MXene particle surface appeared crystalline in XRD, while the sulfur that was incorporated into the MXene structure did not. The strong diffraction lines corresponding to sulfur in figure 4.6 therefore suggest that the sulfur is mainly present on the surface of the MXene particles in the synthesised composite, although it can not be ruled out that a smaller portion of the sulfur is actually incorporated into the structure as well. One possible explanation for why the results obtained in this work differ from the results seen in the previous report can be that an insufficient diffusion time was utilized. As described in section 3.4.1 the melt diffusion was carried out at 155° for 10h, which may be insufficient for the sulfur to completely diffuse into the MXene structure. This could result in the MXene particles being coated with sulfur, rather than the sulfur being intercalated in between the transition metal sheets of the MXene, which is the intended design. The EDX measurements conducted on the composite particles (table 4.3) further strengthen the indications of the sulfur not being properly intercalated into the MXene, as only trace amount of sulfur were detected in the point measurements, which in turn indicate an inhomogeneous distribution of sulfur. Furthermore, the elevated temperature during the melt diffusion does not appear to oxidise or in any other way alter the MXene, as the diffraction lines corresponding to the MXene prior to heat treatment are identical to after the heat treatment.

5.3 Insertion cathodes

Electrolyte verification

The cyclic voltametry of the APC-THF electrolyte (figure 4.16) displayed low overpotentials and a decent current density from the very first cycle. In the following cycles, the overpotentials were further decreased, and the electrolyte generally displayed satisfying Mg stripping and plating capabilities. On the contrary, the cyclic voltametry of the BMOC-DME electrolyte (figure 4.17) displayed high overpotentials and extremely low current densities in the first cycle, and this behaviour was characteristic for the first nine cycles. In the tenth cycle, the overpotentials were reduced and anodic and cathodic currents corresponding to the stripping and plating of Mg, respectively, appeared. The overpotentials were reduced in the following cycles, improving the Mg stripping and plating capabilities. This gradual conditioning of the BMOC-DME electrolyte, improving its performance with prolonged cycling, is consistent with a similar report by Xu et al.[106], suggesting that the electro active species are formed during the first ten to fifteen cycles. Additionally, both electrolytes appear to be stable below the upper voltage limit of 2.1V, as no significant anodic currents are observed at high voltages.

Cycling performance

The cells containing the insertion cathodes produced with V_2C powder from Batch 1 displayed very poor cycling performances, with the cells utilizing the BMOC-DME electrolyte performing slightly better than the cells utilizing the APC-THF electrolyte. Interestingly, the cells cycled with the extended cycling programme displayed higher initial

discharge capacities than the cells cycled with the standard cycling programme. Unfortunately, there were no clear charge or discharge plateaus observed for any of the voltage profiles of the different cells, indicating that no significant reversible or irreversible intercalation of Mg-ions had taken place. It is therefore reasonable to argue that the very limited capacities observed for the different cells can be attributed to surface reactions, instead of the desired intercalation reactions. In a similar work by Lukatskaya et al.[111], Ti_3C_2 MXene was demonstrated to exhibit pseudocapacitive behaviour for Li, and this could possibly be the case for V_2C with Mg as well. Furthermore, the cells utilizing the insertion cathodes containing the V_2C MXene from Batch 2 also displayed very poor capacities, although slightly higher than for the cells utilizing the cathodes from Batch 1. The voltage profiles of these cells did not indicate any significant intercalation of Mg-ions into the MXene cathode, reversibly nor irreversibly. Similarly to the cells containing the insertion cathodes with the MXene from Batch 1, it is reasonable to argue that the rather limited initial discharge capacities observed can be attributed to surface reactions between the electrolyte and the electrodes. The majority of the cells utilizing the BMOC-DME electrolyte were observed to require a large number of cycles before proper cycling behaviour was observed, which can be explained by the gradual conditioning of the electrolyte with prolonged cycling observed in the CV scan.

Electrochemical impedance spectroscopy

The addition of LiCl to the APC-THF electrolyte resulted in significant capacities for the cycled cells, which is interesting as the cells containing the pure APC-THF electrolyte only displayed negligible capacities. The high capacities displayed by the cells containing the LiCl-APC-THF electrolyte are most likely explained by the presence of Li-ions in the electrolyte, as V_2C MXene is known to intercalate Li-ions quite easily[25,26]. Byeon et al.[105] reported on a similar Li/Mg vs MXene hybrid system, where it was demonstrated that the Li-ions were responsible for the observed capacities, which further substantiates the hypothesis described above. Moreover, the rather short cycle lifetime of the cells containing Li may indicate an incompatibility between one or more of the cell constituents, resulting in cell failure after less than a hundred cycles. A likely explanation is increased corrosion, due to higher content of chloride in the elecrolyte, which may lower the oxidative limit below the upper cutoff voltage of 2.1V. Furthermore, the impedance measurements performed on the cells after the first and the final cycle (figure 4.25 and 4.26) indicate that the charge transfer resistance in the cells containing the LiCl-APC-THF is considerably lower than in the cells containing the APC-THF electrolyte, i.e. the charge transfer resistance is lower in cells utilizing Li-ions compared to cells utilizing Mg-ions. This could explain why the cells containing Li-ions performs substantially better than the cells that do not contain Li-ions. However, a more thorough investigation of the charge transfer resistance should be performed to properly interpret the observed semicircles, and experiments utilizing three electrode cells and/or symmetric coin cells could give valuable information about the charge transfer reactions that occur inside the cells.

The fact that indications of Li-ion intercalation was observed, but no signs of Mg-ion intercalation, can be explained by a combination of several aspects. First, the Mg-ions

have a rather high charge density compared to Li-ions, as they have twice the charge and approximately the same volume. This is further related to the typically high migration barriers seen for Mg-ions[112], which in the case of intercalation in MXenes is highly dependant on the surface termination groups[95]. Second, the behaviour of the electrolyte is also important, as the Mg-ions need to successfully desolvate from the electrolyte complex before intercalating into the MXene. This is also one of the reasons for why the BMOC-DME electrolyte was tested in this work, as it utilizes different electroactive species than the APC-THF electrolyte. The slightly higher capacities observed for the BMOC-DME cells compared to the APC-THF cells during galvanostatic cycling could indicate that the electroactive species in the BMOC-DME electrolyte desolvates more successfully than for the APC-THF electrolyte, although no Mg-ion intercalation was observed for either of the electrolytes. All in all, there is a need for further research on this topic to better understand the migration barriers of the Mg-ions, as well as the complicated behaviour of the electrolytes.

5.4 Conversion cathodes

Cycling performance

The cycling results presented in figure 4.27 indicate that the rather decent initial discharge capacity of 312.4 mAh/g can be attributed to reduction of sulfur in the cathode, based on the two observed discharge voltage plateaus. The first and shortest plateau, located at approximately 1.3V, corresponds to the reduction of cyclo-S_8 to polysulfide MgS_4. The second plateau, observed around 0.9V, is attributed to the reduction of MgS_4 to MgS_2, while the downward sloping tail at the very end of the voltage profile corresponds to the reduction of polysuldfide MgS_2 to solid MgS. These results are consistent with reports of similar experiments[69], where a graphene-sulfur nanocomposite was utilized as cathode material. Unfortunately, the following charge sequence only displayed a capacity of approximately 37 mAh/g, suggesting that the reduction reactions observed during discharge were irreversible or that the charge voltage of 2.1V was insufficient. The results of the extended cycling presented in figure 4.28 display an extremely large charge capacity of close to 3000 mAh/g, with an accompanying voltage plateau that fluctuates around 2.2V. In similar work[107,113], the continuous voltage plateau around 2.2V observed during charge was explained by a severe polusulfide shuttling effect, in which the reduction and oxidation of polysulfides are balanced at each of the electrodes, resulting in a constant potential plateau. The polysulfide shuttling effect will be further discussed in the Post-mortem analysis section below. As the polysulfides easily move across the standard glass fibre separators commonly utilized in battery cells, Ford et al.[113] have proposed the use of an ionomer gel separator in Mg-S batteries, as it has been shown to effectively suppress the polysulfide shuttling effect and thus improve the performance of Mg-S systems. Furthermore, the unwanted reduction of polysulfides at the Mg anode can occur irreversibly and form a passivating layer on the anode, which is a possible explanation of the poor cycling performances observed after the first cycle.

Rate capability test

The results of the rate capability test performed for the conversion cathodes paired with the BMOC-DME electrolyte (figure 4.30) indicate that the capacity of the battery system quickly decreases with increasing current densities, further suggesting that current densities of 100 mA/g or more results in negligible capacities. Still, the capacity that is lost at cycling with high current densities is observed to be regained when returning to cycling with the lower current density of 10 mA/g, thus, the capacity loss is considered to be reversible. The quickly decreasing capacities with increasing currents suggest that the transportation and transfer of charge within the cell is rather sluggish, as it appears to become limited by the current already at relatively low current rates. By comparing to the results obtained for the Li reference system discussed below, it becomes clear that the limitations observed in the rate test most likely is due to sluggish kinetics caused by the high charge density of the Mg-ions compared to the Li-ions, rather than the cathode itself.

Post-mortem analysis

In the EDX measurements performed on the cell constituents after cycling (table 4.7), significant amounts of sulfur were detected on both sides of the separator, indicating that polysulfide shuttling had occurred. Significant amounts of sulfur were also found on the side of the anode facing the separator, which suggests that some sort of reaction resulting in sulfur adhering to the anode surface had taken place during cycling. This further strengthens the hypothesis that the extreme charge plateau observed was caused by irreversible reduction and oxidation of polysulfides at the electrodes. However, it is difficult to draw any conclusions regarding the formation of a passivating layer based on only the cycling results and EDX measurements, and a more thorough investigation of the polysufide reactions occurring at the anode should be performed.

Moreover, the EDX mapping (figure 4.31), performed on the side of the Mg anode that was in contact with the current collector during cycling, indicates that the black spots observed along the edge of the anode is an unknown compound containing sulfur. In addition to the sulfur, significant signals from oxygen and carbon was also observed at the locations of the black spots, suggesting that a reaction involving two or more of these elements have occurred. The cell was disassembled in an ambient air atmosphere, and it is therefore reasonable to believe that a large portion of the observed oxygen originate from this procedure. Due to the lack of magnesium at the locations of the black spots, it is reasonable to assume that the observed compound is not magnesium sulfides, but it is difficult to say this conclusively based on the mapping alone. Determining exactly what reactions that have taken place would require a more thorough investigation of the observed compound, but a speculative guess could be the oxidation of sulfur compounds in a reaction with oxygen. Ideally, the oxide layer on the Mg foil should be removed by polishing during anode preparation, but it is not unreasonable to argue that this may not be the case and that oxides on the anode can be a source of oxygen in the system.

The EDX measurements of the cycled conversion cathode show significant amounts of magnesium in the cathode, which can not be attributed to the electrolyte residues alone.

Thus, this suggests that irreversible conversion reactions between magnesium and sulfur have occurred, resulting in significant amounts of solid magnesium sulfide in the cathode structure. Additionally, as polysulfide shuttling was observed, it is reasonable to attribute some of the observed magnesium to polysulfides trapped in the cathodes structure as well. In general, trapping of polysulfides is a desirable trait for a cathode design, as it prevents some or all of the polysulfides from shuttling to the anode side during cycling, thus prolonging the cycle lifetime. However, it should be emphasized that the cell was disassembled in a charged state, where all the polysulfides ideally should be converted back to elementary sulfur. Furthermore, a large number of cracks in the cathode surface is observed in the SEM images of the cycled cathode (figure 4.34c and 4.34d), compared to the uncycled cathode (figure 4.34a and 4.34b). One possible explanation is expansion of the cathode during discharge of the cell, as a large portion of the sulfur in the cathode structure is reduced and forms liquid polysulfides, resulting in a volume increase. In general, conversion cathodes are known to suffer from volume changes reducing the cycle lifetime, thus it is reasonable to believe that this is the case for MXene-S composite cathodes as well.

The EDX measurements of the glass fibre separator indicated the presence of a wide range of elements. As the glass fibres in the separator are made from borosilicate glass, the significant amounts of silicon, oxygen, sodium, carbon, aluminium and boron are attributed to the separator itself. The presence of magnesium, sulfur and fluorine is most likely due to a combination of polysulfides and the BMOC-DME electrolyte soaking the separator. Furthermore, relatively low amounts of potassium, calcium, titanium and zink are also detected in the separator, and the most likely explanation is that these elements originate from the manufacturing of the glass fibre separators.

Reference Li-system

The two cells containing Li anodes confirmed that the V_2C-S conversion cathodes were able to sustain repeated cycles of discharge and charge, with the accompanying repeated reduction and oxidation of the sulfur in the cathode structure. Both cells displayed rather high discharge and charge capacities, with distinct discharge and charge plateaus observed in the voltage profiles, suggesting that the electrochemical reactions taking place at the anode and cathode were reversible. The cell displaying the most stable cycling behaviour sustained almost 600 cycles before abruptly failing, suggesting there were no major issues related to polysulfides or volume expansion of the cathode in the cell. For the other cell, the rather unstable behaviour from around cycle number 200 and onward suggests an issue within the cell. One possible explanation for the observed behaviour is polysulfide shuttling, as the reduction and oxidation of polysulfides would cause an increase in the charge capacity without an increase in the discharge capacity. However, some of the discharge capacity that is lost during cycling is seen to be regained in later cycles, and considering the rather high current density of 837.5 mA/g, it is possible that the fluctuations in capacity is caused by limitations due to the high current density. All in all, the Li containing reference cells performed rather well and there is no doubt that the conversion cathodes are able to sustain prolonged cycling, with repeated cycles of charge and discharge at rather high current densities.

5.5 Evaluation of V_2C MXene based cathodes

The overall performance of the cells utilizing MXene insertion cathodes with different electrolytes were extremely poor, where the largest capacities and initial voltages were measured for the cells utilising the cathodes produced with the MXene from Batch 2 and the BMOC-DME electrolyte. The sloping voltage profile and limited capacities were attributed to surface reactions rather than Mg-ion intercalation, leading to a preliminary conclusion of the unsuitability of V_2C MXene as Mg-ion insertion cathode. However, given the complexity of cathode performances, improvements in the cathode structure or electrolyte, may enable Mg-ion intercalation. For example, the MXene utilized in the production of the insertion cathodes was mainly surface terminated by fluorine and oxygen, which may hinder the intercalation of the divalent Mg-ions and thus limit the performance of the cells. Optimization of the termination groups may thus be an effective strategy to enable V_2C MXene insertion cathodes.

The overall performance of the cells utilizing conversion cathodes were significantly better than what was observed for the insertion cathodes, and conversion cathodes appears to be a promising route for practical RMBs. However, the polysulfide shuttling effect was identified to be a major factor limiting the performance. In this first work on V_2C-S composites, the V_2C MXene was not found to be sufficient to immobilize the polysulfides for the Mg-S batteries. Noteworthy, the Li-reference cells showed excellent capacity retention, which suggests that the polysulfide shuttling is more prominent for Mg-S than Li-S batteries. Still, given the growing literature on MXene as sulfur host for Li-S batteries, V2C MXenes may be an effective constituent of the sulfur composite cathode for Mg-S batteries as well. By optimizing the melt diffusion process to fully integrate the sulfur between the MXene structure, the polysulfide shuttling may be significantly reduced. Together with an improved electrolyte, this may open up for energy dense RMBs based on cheap and highly abundant materials.

Chapter 6

Conclusion

The solid state synthesis of V_2AlC MAX phase from metal powder precursors utilized in this work yielded a V_2AlC MAX phase of moderate phase purity, with significant amounts of secondary phases. In the subsequent etching step, it was shown that particle size and etching duration greatly affect the result of the exfoliation process, with regard to completeness of the etching. It was found that particles with a size distribution having a mean size of 6.3 μm and a standard deviation of 2.6 μm combined with an etching duration of 96h in 48% HF was an optimal combination of parameters, resulting in the complete conversion of V_2AlC MAX phase to V_2C MXene. The resulting MXene contained significant amounts of fluorine and oxygen, which was attributed to the surface terminations formed during the etching procedure.

Coin cells utilizing insertion cathodes containing the synthesised MXene displayed poor electrochemical performances for both the APC-THF and BMOC-DME electrolytes, with very limited charge and discharge capacities. The low capacities that were observed were attributed to surface reactions and pseudocapacitive effects, rather than insertion reactions, as no clear signs of Mg-ion intercalation were found. By addition of LiCl to the APC-THF electrolyte, it was shown that the V_2C MXene cathodes were able to reversibly intercalate Li-ions, suggesting that the high charge density of Mg-ions and the various surface termination groups of the MXene may hinder the intercalation of Mg-ions.

Despite displaying a rather high initial discharge capacity of 312.4 mAh/g, the battery system utilizing a Mg anode, BMOC-DME electrolye and V_2C-S conversion cathode was found to suffer from severe polysulfide shuttling upon charge, resulting in negligible capacities. The conversion cathodes were validated in systems containing Li anodes and the LiTFSI-$LiNO_3$-DOL-DME electrolyte, displaying capacities well above 400 mAh/g for several hundred consecutive cycles.

In conclusion, the two different V_2C MXene cathode designs explored in this work display limited electrochemical performances when tested in magnesium battery systems.

However, this does not exclude V_2C MXene as a constituent in insertion and conversion cathodes for RMBs, but emphasizes the challenging nature of these battery systems. Thus, further fundamental research on the material and its properties is necessary in order to achieve functioning RMBs.

Chapter 7

Further Work

The span of this work only covers a fraction of the research that could be done on V_2C MXene as a possible cathode material in RMBs, and there are several key challenges that require further investigation. The solid state synthesis route utilized for the synthesis of V_2AlC MAX phase obviously requires improvement, as it yields a MAX phase with significant amounts of secondary phases. One suggestion may therefore be to attempt a similar synthesis route, but with vanadium and aluminium carbides as precursors instead of the metallic powders used in this work. This would mitigate the issue of aluminium evaporating during the high temperature sintering step, thus giving better control of the stoichiometry in the precursor mixture throughout the synthesis. Moreover, it would simplify the synthesis procedure, as the carbides are stable in ambient atmospheres, as opposed to the metallic vanadium and aluminium powders utilized in this work.

Another important topic that should be investigated further is the surface termination groups formed during the etching step. As these terminations are expected to greatly influence the intercalation properties of the MXene, it is crucial to understand how the terminations are formed, and to what degree they can be altered or replaced to improve the intercalation properties of the V_2C MXene. Density functional calculations could be applied to investigate the migration of Mg-ions in V_2C MXene, and hopefully indicate which combination of surface termination groups that gives the lowest migration barriers. Another suggestion could be to attempt to replace some of the highly electronegative fluorine terminations with termination groups that are more polarisable, e.g. sulfur or oxygen, as this is predicted to reduce the barrier for Mg-ion intercalation. In order to gain a better understanding of the distribution of the surface termination groups, characterization techniques such as X-ray photoelectron spectroscopy (XPS) and Fourier-transform infrared spectroscopy (FTIR) can be applied in the characterization of the MXene.

Rechargeable Mg-S batteries utilizing MXene-S composite conversion cathodes appear to be rather promising, but a better understanding of the interactions between the electrolyte and sulfur cathode is required. Improvements to the cathode and separator are also desir-

able to mitigate the polysulfide shuttling effect, which is a major challenge that needs to be solved to achieve viable Mg-S batteries.

Bibliography

[1] John B. Goodenough and Kyu-Sung Park. “The Li-Ion Rechargeable Battery: A Perspective”. In: *Journal of the American Chemical Society* 135.4 (2013), pp. 1167–1176.

[2] Chengyi Wang, Zhaojun Xie, and Zhen Zhou. “Lithium-air batteries: Challenges coexist with opportunities”. In: *APL Materials* 7.4 (2019), p. 040701.

[3] BP. *BP Statistical Review of World Energy*. 2018. URL: https://www.bp.com/content/dam/bp/en/corporate/pdf/energy-economics/statistical-review/bp-stats-review-2018-full-report.pdf (visited on 02/07/2019).

[4] Dominique Larcher and Jean-Marie Tarascon. “Towards greener and more sustainable batteries for electrical energy storage”. In: *Nature chemistry* 7.1 (2015), p. 19.

[5] Chris D Thomas, Alison Cameron, Rhys E Green, Michel Bakkenes, Linda J Beaumont, Yvonne C Collingham, Barend FN Erasmus, Marinez Ferreira De Siqueira, Alan Grainger, Lee Hannah, et al. “Extinction risk from climate change”. In: *Nature* 427.6970 (2004), p. 145.

[6] Connor Nolan, Jonathan T Overpeck, Judy RM Allen, Patricia M Anderson, Julio L Betancourt, Heather A Binney, Simon Brewer, Mark B Bush, Brian M Chase, Rachid Cheddadi, et al. “Past and future global transformation of terrestrial ecosystems under climate change”. In: *Science* 361.6405 (2018), pp. 920–923.

[7] Richard E Smalley. “Future global energy prosperity: the terawatt challenge”. In: *Mrs Bulletin* 30.6 (2005), pp. 412–417.

[8] Nathan S Lewis. “Powering the planet”. In: *MRS bulletin* 32.10 (2007), pp. 808–820.

[9] Thomas B Reddy. “Linden’s handbook of batteries”. In: *New York, USA* (2011).

[10] John Muldoon, Claudiu B. Bucur, and Thomas Gregory. “Quest for Nonaqueous Multivalent Secondary Batteries: Magnesium and Beyond”. In: *Chemical Reviews* 114.23 (2014), pp. 11683–11720.

[11] Arumugam Manthiram, Yongzhu Fu, and Yu-Sheng Su. “Challenges and prospects of lithium–sulfur batteries”. In: *Accounts of chemical research* 46.5 (2012), pp. 1125–1134.

[12] Claudiu B Bucur, John Muldoon, Adrian Lita, Joseph B Schlenoff, Ramy A Ghostine, Steve Dietz, and Gary Allred. “Ultrathin tunable ion conducting nanomembranes for encapsulation of sulfur cathodes”. In: *Energy & Environmental Science* 6.11 (2013), pp. 3286–3290.

[13] Peter G Bruce, Stefan A Freunberger, Laurence J Hardwick, and Jean-Marie Tarascon. “Li–O 2 and Li–S batteries with high energy storage”. In: *Nature materials* 11.1 (2012), p. 19.

[14] Michael D Slater, Donghan Kim, Eungje Lee, and Christopher S Johnson. “Sodium-ion batteries”. In: *Advanced Functional Materials* 23.8 (2013), pp. 947–958.

[15] John Muldoon, Claudiu B Bucur, Allen G Oliver, Tsuyoshi Sugimoto, Masaki Matsui, Hee Soo Kim, Gary D Allred, Jaroslav Zajicek, and Yukinari Kotani. “Electrolyte roadblocks to a magnesium rechargeable battery”. In: *Energy & Environmental Science* 5.3 (2012), pp. 5941–5950.

[16] Doron Aurbach, Idit Weissman, Yosef Gofer, and Elena Levi. “Nonaqueous magnesium electrochemistry and its application in secondary batteries”. In: *The Chemical Record* 3.1 (2003), pp. 61–73.

[17] Masaki Matsui. “Study on electrochemically deposited Mg metal”. In: *Journal of Power Sources* 196.16 (2011). 15th International Meeting on Lithium Batteries (IMLB), pp. 7048–7055. ISSN: 0378-7753.

[18] Rana Mohtadi and Fuminori Mizuno. “Magnesium batteries: Current state of the art, issues and future perspectives”. In: *Beilstein Journal of Nanotechnology* 5 (2014), pp. 1291–1311. ISSN: 2190-4286.

[19] Peter C. K. Vesborg and Thomas F. Jaramillo. “Addressing the terawatt challenge: scalability in the supply of chemical elements for renewable energy”. In: *RSC Adv.* 2 (21 2012), pp. 7933–7947.

[20] Michael Naguib, Murat Kurtoglu, Volker Presser, Jun Lu, Junjie Niu, Min Heon, Lars Hultman, Yury Gogotsi, and Michel W Barsoum. “Two-dimensional nanocrystals produced by exfoliation of Ti3AlC2”. In: *Advanced Materials* 23.37 (2011), pp. 4248–4253.

[21] Christopher Eames and M Saiful Islam. “Ion intercalation into two-dimensional transition-metal carbides: global screening for new high-capacity battery materials”. In: *Journal of the American Chemical Society* 136.46 (2014), pp. 16270–16276.

[22] Michael Ghidiu, Maria R Lukatskaya, Meng-Qiang Zhao, Yury Gogotsi, and Michel W Barsoum. “Conductive two-dimensional titanium carbide ‘clay’with high volumetric capacitance”. In: *Nature* 516.7529 (2014), p. 78.

[23] Xiao Liang, Arnd Garsuch, and Linda F Nazar. “Sulfur cathodes based on conductive MXene nanosheets for high-performance lithium–sulfur batteries”. In: *Angewandte Chemie International Edition* 54.13 (2015), pp. 3907–3911.

[24] Xiaoqin Zhao, Min Liu, Yong Chen, Bo Hou, Na Zhang, Binbin Chen, Ning Yang, Ke Chen, Jianlin Li, and Linan An. “Fabrication of layered Ti 3 C 2 with an accordion-like structure as a potential cathode material for high performance lithium–sulfur batteries”. In: *Journal of Materials Chemistry A* 3.15 (2015), pp. 7870–7876.

[25] Michael Naguib, Joseph Halim, Jun Lu, Kevin M Cook, Lars Hultman, Yury Gogotsi, and Michel W Barsoum. “New two-dimensional niobium and vanadium carbides as promising materials for Li-ion batteries”. In: *Journal of the American Chemical Society* 135.43 (2013), pp. 15966–15969.

[26] Fanfan Liu, Jie Zhou, Shuwei Wang, Bingxin Wang, Cai Shen, Libo Wang, Qianku Hu, Qing Huang, and Aiguo Zhou. “Preparation of high-purity V2C MXene and electrochemical properties as Li-ion batteries”. In: *Journal of The Electrochemical Society* 164.4 (2017), A709–A713.

[27] Yohan Dall’Agnese, Pierre-Louis Taberna, Yury Gogotsi, and Patrice Simon. “Two-dimensional vanadium carbide (MXene) as positive electrode for sodium-ion capacitors”. In: *The journal of physical chemistry letters* 6.12 (2015), pp. 2305–2309.

[28] Armin VahidMohammadi, Ali Hadjikhani, Sina Shahbazmohamadi, and Majid Beidaghi. “Two-Dimensional Vanadium Carbide (MXene) as a High-Capacity Cathode Material for Rechargeable Aluminum Batteries”. In: *ACS nano* 11.11 (2017), pp. 11135–11144.

[29] Pankaj Arora and Zhengming (John) Zhang. “Battery Separators”. In: *Chemical Reviews* 104.10 (2004), pp. 4419–4462.

[30] R M Dell and D A J Rand. *Understanding Batteries*. RSC Paperbacks. The Royal Society of Chemistry, 2001, pp. 10–33. ISBN: 978-0-85404-605-8.

[31] Adam H. Whitehead and Martha Schreiber. “Current Collectors for Positive Electrodes of Lithium-Based Batteries”. In: *Journal of The Electrochemical Society* 152 (11 2005), A2105–A2113.

[32] Akira Yoshino, Kenichi Sanechika, and Takayuki Nakajima. “Secondary battery”. Japanese Patent No. 1989293. 1985.

[33] Wu Xu, Jiulin Wang, Fei Ding, Xilin Chen, Eduard Nasybulin, Yaohui Zhang, and Ji-Guang Zhang. “Lithium metal anodes for rechargeable batteries”. In: *Energy Environ. Sci.* 7 (2 2014), pp. 513–537.

[34] M Yoshio, RJ Brodd, and Akiya Kozawa. *Lithium-ion batteries: science and technologies. 2009*.

[35] Martin Winter and Ralph J. Brodd. “What Are Batteries, Fuel Cells, and Supercapacitors?” In: *Chemical Reviews* 104.10 (2004), pp. 4245–4270.

[36] D Aurbach, Z Lu, A Schechter, Y Gofer, H Gizbar, R Turgeman, Y Cohen, M Moshkovich, and El Levi. “Prototype systems for rechargeable magnesium batteries”. In: *Nature* 407.6805 (2000), p. 724.

[37] Toyota.com. *Charging Ahead. Toyota Scientists Make Breakthrough on Safer, Smarter Batteries*. 2016. URL: https://corporatenews.pressroom.toyota.com/releases/toyota-scientists-breakthrough-safer-smarter-batteries.htm?view_id=42844 (visited on 12/12/2018).

[38] Hyun Deog Yoo, Ivgeni Shterenberg, Yosef Gofer, Gregory Gershinsky, Nir Pour, and Doron Aurbach. "Mg rechargeable batteries: an on-going challenge". In: *Energy Environ. Sci.* 6 (8 2013), pp. 2265–2279.

[39] E Levi, Y Gofer, and D Aurbach. "On the way to rechargeable Mg batteries: the challenge of new cathode materials". In: *Chemistry of Materials* 22.3 (2009), pp. 860–868.

[40] Timothy S. Arthur, Nikhilendra Singh, and Masaki Matsui. "Electrodeposited Bi, Sb and Bi1-xSbx alloys as anodes for Mg-ion batteries". In: *Electrochemistry Communications* 16.1 (2012), pp. 103–106. ISSN: 1388-2481.

[41] Jing Zeng, Yang Yang, Chao Li, Jiaqi Li, Jianxing Huang, Jing Wang, and Jinbao Zhao. "Li3VO4: an insertion anode material for magnesium ion batteries with high specific capacity". In: *Electrochimica Acta* 247 (2017), pp. 265–270. ISSN: 0013-4686.

[42] Na Wu, Ying-Chun Lyu, Rui-Juan Xiao, Xiqian Yu, Ya-Xia Yin, Xiao-Qing Yang, Hong Li, Lin Gu, and Yu-Guo Guo. "A highly reversible, low-strain Mg-ion insertion anode material for rechargeable Mg-ion batteries". In: *NPG Asia Materials* 6.8 (2014), e120.

[43] Thomas D Gregory, Ronald J Hoffman, and Richard C Winterton. "Nonaqueous electrochemistry of magnesium applications to energy storage". In: *Journal of The Electrochemical Society* 137.3 (1990), pp. 775–780.

[44] Doron Aurbach, Haim Gizbar, Alex Schechter, Orit Chusid, Hugo E Gottlieb, Yossi Gofer, and Israel Goldberg. "Electrolyte solutions for rechargeable magnesium batteries based on organomagnesium chloroaluminate complexes". In: *Journal of The Electrochemical Society* 149.2 (2002), A115–A121.

[45] Nir Pour, Yossi Gofer, Dan T Major, and Doron Aurbach. "Structural analysis of electrolyte solutions for rechargeable Mg batteries by stereoscopic means and DFT calculations". In: *Journal of the American Chemical Society* 133.16 (2011), pp. 6270–6278.

[46] Oren Mizrahi, Nir Amir, Elad Pollak, Orit Chusid, Vered Marks, Hugo Gottlieb, Liraz Larush, Ella Zinigrad, and Doron Aurbach. "Electrolyte solutions with a wide electrochemical window for rechargeable magnesium batteries". In: *Journal of the Electrochemical Society* 155.2 (2008), A103–A109.

[47] Robert E Doe, Ruoban Han, Jaehee Hwang, Andrew J Gmitter, Ivgeni Shterenberg, Hyun Deog Yoo, Nir Pour, and Doron Aurbach. "Novel, electrolyte solutions comprising fully inorganic salts with high anodic stability for rechargeable magnesium batteries". In: *Chemical Communications* 50.2 (2014), pp. 243–245.

[48] Rana Mohtadi, Masaki Matsui, Timothy S Arthur, and Son-Jong Hwang. "Magnesium borohydride: from hydrogen storage to magnesium battery". In: *Angewandte Chemie International Edition* 51.39 (2012), pp. 9780–9783.

[49] Tyler J Carter, Rana Mohtadi, Timothy S Arthur, Fuminori Mizuno, Ruigang Zhang, Soichi Shirai, and Jeff W Kampf. “Boron Clusters as Highly Stable Magnesium-Battery Electrolytes”. In: *Angewandte Chemie International Edition* 53.12 (2014), pp. 3173–3177.

[50] Oscar Tutusaus, Rana Mohtadi, Timothy S Arthur, Fuminori Mizuno, Emily G Nelson, and Yulia V Sevryugina. “An Efficient Halogen-Free Electrolyte for Use in Rechargeable Magnesium Batteries”. In: *Angewandte Chemie* 127.27 (2015), pp. 8011–8015.

[51] Se-Young Ha, Yong-Won Lee, Sang Won Woo, Bonjae Koo, Jeom-Soo Kim, Jaephil Cho, Kyu Tae Lee, and Nam-Soon Choi. “Magnesium (II) bis (trifluoromethane sulfonyl) imide-based electrolytes with wide electrochemical windows for rechargeable magnesium batteries”. In: *ACS applied materials & interfaces* 6.6 (2014), pp. 4063–4073.

[52] Yanna NuLi, Jun Yang, and Rong Wu. “Reversible deposition and dissolution of magnesium from BMIMBF4 ionic liquid”. In: *Electrochemistry communications* 7.11 (2005), pp. 1105–1110.

[53] GT Cheek, WE O’Grady, S Zein El Abedin, EM Moustafa, and F Endres. “Studies on the electrodeposition of magnesium in ionic liquids”. In: *Journal of the Electrochemical Society* 155.1 (2008), pp. D91–D95.

[54] N Amir, Y Vestfrid, O Chusid, Y Gofer, and D Aurbach. “Progress in nonaqueous magnesium electrochemistry”. In: *Journal of Power Sources* 174.2 (2007), pp. 1234–1240.

[55] G Girish Kumar and N Munichandraiah. “Poly (methylmethacrylate)—magnesium triflate gel polymer electrolyte for solid state magnesium battery application”. In: *Electrochimica acta* 47.7 (2002), pp. 1013–1022.

[56] KM Anilkumar, B Jinisha, M Manoj, and S Jayalekshmi. “Poly (ethylene oxide)(PEO)–Poly (vinyl pyrrolidone)(PVP) blend polymer based solid electrolyte membranes for developing solid state magnesium ion cells”. In: *European Polymer Journal* 89 (2017), pp. 249–262.

[57] M. Rosa Palacín. “Recent advances in rechargeable battery materials: a chemist’s perspective”. In: *Chem. Soc. Rev.* 38 (9 2009), pp. 2565–2575.

[58] E Levi, MD Levi, O Chasid, and D Aurbach. “A review on the problems of the solid state ions diffusion in cathodes for rechargeable Mg batteries”. In: *Journal of electroceramics* 22.1-3 (2009), pp. 13–19.

[59] E Levi, G Gershinsky, D Aurbach, O Isnard, and Gerbrand Ceder. “New insight on the unusually high ionic mobility in chevrel phases”. In: *Chemistry of materials* 21.7 (2009), pp. 1390–1399.

[60] Thanayut Kaewmaraya, Muhammad Ramzan, JM Osorio-Guillén, and Rajeev Ahuja. “Electronic structure and ionic diffusion of green battery cathode material: Mg2Mo6S8”. In: *Solid State Ionics* 261 (2014), pp. 17–20.

[61] Partha Saha, Prashanth H Jampani, Moni Kanchan Datta, Chris U Okoli, Ayyakkannu Manivannan, and Prashant N Kumta. “A convenient approach to Mo6S8 Chevrel phase cathode for rechargeable magnesium battery”. In: *Journal of The Electrochemical Society* 161.4 (2014), A593–A598.

[62] Pieremanuele Canepa, Shou-Hang Bo, Gopalakrishnan Sai Gautam, Baris Key, William D Richards, Tan Shi, Yaosen Tian, Yan Wang, Juchuan Li, and Gerbrand Ceder. “High magnesium mobility in ternary spinel chalcogenides”. In: *Nature communications* 8.1 (2017), p. 1759.

[63] Xiaoqi Sun, Patrick Bonnick, and Linda F Nazar. “Layered TiS2 positive electrode for Mg batteries”. In: *ACS Energy Letters* 1.1 (2016), pp. 297–301.

[64] Chen Ling and Ruigang Zhang. “Manganese dioxide as rechargeable magnesium battery cathode”. In: *Frontiers in Energy Research* 5 (2017), p. 30.

[65] Ruigang Zhang, Timothy S Arthur, Chen Ling, and Fuminori Mizuno. “Manganese dioxides as rechargeable magnesium battery cathode; synthetic approach to understand magnesiation process”. In: *Journal of Power Sources* 282 (2015), pp. 630–638.

[66] Masashi Inamoto, Hideki Kurihara, and Tatsuhiko Yajima. “Vanadium pentoxide-based composite synthesized using microwave water plasma for cathode material in rechargeable magnesium batteries”. In: *Materials* 6.10 (2013), pp. 4514–4522.

[67] Gregory Gershinsky, Hyun Deog Yoo, Yosef Gofer, and Doron Aurbach. “Electrochemical and spectroscopic analysis of Mg2+ intercalation into thin film electrodes of layered oxides: V2O5 and MoO3”. In: *Langmuir* 29.34 (2013), pp. 10964–10972.

[68] MK Aydinol, AF Kohan, G Ceder, K Cho, and J Joannopoulos. “Ab initio study of lithium intercalation in metal oxides and metal dichalcogenides”. In: *Physical Review B* 56.3 (1997), p. 1354.

[69] BP Vinayan, Zhirong Zhao-Karger, Thomas Diemant, Venkata Sai Kiran Chakravadhanula, Nele I Schwarzburger, Musa Ali Cambaz, R Jürgen Behm, Christian Kübel, and Maximilian Fichtner. “Performance study of magnesium–sulfur battery using a graphene based sulfur composite cathode electrode and a non-nucleophilic Mg electrolyte”. In: *Nanoscale* 8.6 (2016), pp. 3296–3306.

[70] Michel W Barsoum. “The MN+ 1AXN phases: A new class of solids: Thermodynamically stable nanolaminates”. In: *Progress in solid state chemistry* 28.1-4 (2000), pp. 201–281.

[71] Tianyu Liu. *The Birth of MXene*. 2017. URL: `https://liutianyuresearch.weebly.com/the-birth-of-mxene.html` (visited on 12/16/2018).

[72] Vincent Ming Hong Ng, Hui Huang, Kun Zhou, Pooi See Lee, Wenxiu Que, Zhichuan J Xu, and Ling Bing Kong. “Correction: Recent progress in layered transition metal carbides and/or nitrides (MXenes) and their composites: synthesis and applications”. In: *Journal of Materials Chemistry A* 5.18 (2017), pp. 8769–8769.

[73] Babak Anasori, Maria R Lukatskaya, and Yury Gogotsi. “2D metal carbides and nitrides (MXenes) for energy storage”. In: *Nature Reviews Materials* 2.2 (2017), p. 16098.

[74] Per Eklund, Johanna Rosen, and Per O Å Persson. “Layered ternary M n+ 1AX n phases and their 2D derivative MXene: an overview from a thin-film perspective”. In: *Journal of Physics D: Applied Physics* 50.11 (2017), p. 113001.

[75] Michael Naguib, Vadym N Mochalin, Michel W Barsoum, and Yury Gogotsi. “25th anniversary article: MXenes: a new family of two-dimensional materials”. In: *Advanced Materials* 26.7 (2014), pp. 992–1005.

[76] Frode Håskjold Fagerli. “Exploring V_2C MXene as a New Cathode Material for Rechargeable Magnesium Batteries”. Master Thesis. Norwegian University of Science and Technology, 2018.

[77] Junping Hu, Bo Xu, Chuying Ouyang, Shengyuan A Yang, and Yugui Yao. “Investigations on V2C and V2CX2 (X= F, OH) monolayer as a promising anode material for Li ion batteries from first-principles calculations”. In: *The Journal of Physical Chemistry C* 118.42 (2014), pp. 24274–24281.

[78] Yuelei Bai, Kun Zhou, Narasimalu Srikanth, John HL Pang, Xiaodong He, and Rongguo Wang. “Dependence of elastic and optical properties on surface terminated groups in two-dimensional MXene monolayers: a first-principles study”. In: *RSC Advances* 6.42 (2016), pp. 35731–35739.

[79] Mohammad Khazaei, Masao Arai, Taizo Sasaki, Ahmad Ranjbar, Yunye Liang, and Seiji Yunoki. “OH-terminated two-dimensional transition metal carbides and nitrides as ultralow work function materials”. In: *Physical Review B* 92.7 (2015), p. 075411.

[80] Yu Xie, Michael Naguib, Vadym N Mochalin, Michel W Barsoum, Yury Gogotsi, Xiqian Yu, Kyung-Wan Nam, Xiao-Qing Yang, Alexander I Kolesnikov, and Paul RC Kent. “Role of surface structure on Li-ion energy storage capacity of two-dimensional transition-metal carbides”. In: *Journal of the American Chemical Society* 136.17 (2014), pp. 6385–6394.

[81] Olha Mashtalir, Michael Naguib, Boris Dyatkin, Yury Gogotsi, and Michel W Barsoum. “Kinetics of aluminum extraction from Ti3AlC2 in hydrofluoric acid”. In: *Materials Chemistry and Physics* 139.1 (2013), pp. 147–152.

[82] Michael Naguib, Olha Mashtalir, Joshua Carle, Volker Presser, Jun Lu, Lars Hultman, Yury Gogotsi, and Michel W Barsoum. “Two-dimensional transition metal carbides”. In: *ACS nano* 6.2 (2012), pp. 1322–1331.

[83] Maria R Lukatskaya, Olha Mashtalir, Chang E Ren, Yohan Dall’Agnese, Patrick Rozier, Pierre Louis Taberna, Michael Naguib, Patrice Simon, Michel W Barsoum, and Yury Gogotsi. “Cation intercalation and high volumetric capacitance of two-dimensional titanium carbide”. In: *Science* 341.6153 (2013), pp. 1502–1505.

[84] Michael Naguib, Raymond R Unocic, Beth L Armstrong, and Jagjit Nanda. “Large-scale delamination of multi-layers transition metal carbides and carbonitrides “MXenes””. In: *Dalton transactions* 44.20 (2015), pp. 9353–9358.

[85] Yu Zhong, Xinhui Xia, Fan Shi, Jiye Zhan, Jiangping Tu, and Hong Jin Fan. “Transition metal carbides and nitrides in energy storage and conversion”. In: *Advanced science* 3.5 (2016), p. 1500286.

[86] Qing Tang, Zhen Zhou, and Panwen Shen. “Are MXenes promising anode materials for Li ion batteries? Computational studies on electronic properties and Li storage capability of Ti3C2 and Ti3C2X2 (X= F, OH) monolayer”. In: *Journal of the American Chemical Society* 134.40 (2012), pp. 16909–16916.

[87] HB Zhang, YC Zhou, YW Bao, and JY Wang. “Oxidation behavior of bulk Ti 3 SiC 2 at intermediate temperatures in dry air”. In: *Journal of materials research* 21.2 (2006), pp. 402–408.

[88] Babak Anasori, Yu Xie, Majid Beidaghi, Jun Lu, Brian C Hosler, Lars Hultman, Paul RC Kent, Yury Gogotsi, and Michel W Barsoum. “Two-dimensional, ordered, double transition metals carbides (MXenes)”. In: *ACS nano* 9.10 (2015), pp. 9507–9516.

[89] Michel W Barsoum and Tamer El-Raghy. “Synthesis and characterization of a remarkable ceramic: Ti3SiC2”. In: *Journal of the American Ceramic Society* 79.7 (1996), pp. 1953–1956.

[90] Jian Yang, Michael Naguib, Michael Ghidiu, Li-Mei Pan, Jian Gu, Jagjit Nanda, Joseph Halim, Yury Gogotsi, and Michel W Barsoum. “Two-Dimensional Nb-Based M4C3 Solid Solutions (MXenes)”. In: *Journal of the American Ceramic Society* 99.2 (2016), pp. 660–666.

[91] Patrice Simon. “Two-dimensional MXene with controlled interlayer spacing for electrochemical energy storage”. In: *ACS nano* 11.3 (2017), pp. 2393–2396.

[92] Eric S Muckley, Michael Naguib, Hsiu-Wen Wang, Lukas Vlcek, Naresh C Osti, Robert L Sacci, Xiahan Sang, Raymond R Unocic, Yu Xie, Madhusudan Tyagi, et al. “Multimodality of structural, electrical, and gravimetric responses of intercalated MXenes to water”. In: *ACS nano* 11.11 (2017), pp. 11118–11126.

[93] Ming Lu, Haojie Li, Wenjuan Han, Junnan Chen, Wen Shi, Jiaheng Wang, Xiang-Min Meng, Jingang Qi, Haibo Li, Bingsen Zhang, et al. “2D titanium carbide (MXene) electrodes with lower-F surface for high performance lithium-ion batteries”. In: *Journal of energy chemistry* 31 (2019), pp. 148–153.

[94] Yohan Dall’Agnese, Maria R Lukatskaya, Kevin M Cook, Pierre-Louis Taberna, Yury Gogotsi, and Patrice Simon. “High capacitance of surface-modified 2D titanium carbide in acidic electrolyte”. In: *Electrochemistry Communications* 48 (2014), pp. 118–122.

[95] Yu Xie, Yohan Dall’Agnese, Michael Naguib, Yury Gogotsi, Michel W Barsoum, Houlong L Zhuang, and Paul RC Kent. “Prediction and characterization of MXene nanosheet anodes for non-lithium-ion batteries”. In: *ACS nano* 8.9 (2014), pp. 9606–9615.

[96] Meng-Qiang Zhao, Chang E Ren, Mohamed Alhabeb, Babak Anasori, Michel W Barsoum, and Yury Gogotsi. “Magnesium-Ion Storage Capability of MXenes”. In: *ACS Applied Energy Materials* (2019).

[97] Weizhai Bao, Dawei Su, Wenxue Zhang, Xin Guo, and Guoxiu Wang. “3D Metal Carbide@ Mesoporous Carbon Hybrid Architecture as a New Polysulfide Reservoir for Lithium-Sulfur Batteries”. In: *Advanced Functional Materials* 26.47 (2016), pp. 8746–8756.

[98] Johannes Etzkorn, Martin Ade, and Harald Hillebrecht. “V2AlC, V4AlC3-x (x ≈ 0.31), and V12Al3C8: synthesis, crystal growth, structure, and superstructure”. In: *Inorganic chemistry* 46.18 (2007), pp. 7646–7653.

[99] Zhimei Sun, Sa Li, Rajeev Ahuja, and Jochen M Schneider. “Calculated elastic properties of M2AlC (M= Ti, V, Cr, Nb and Ta)”. In: *Solid state communications* 129.9 (2004), pp. 589–592.

[100] Koichi Momma and Fujio Izumi. “VESTA 3 for three-dimensional visualization of crystal, volumetric and morphology data”. In: *Journal of applied crystallography* 44.6 (2011), pp. 1272–1276.

[101] Qingmin Shan, Xinpeng Mu, Mohamed Alhabeb, Christopher E Shuck, Di Pang, Xin Zhao, Xue-Feng Chu, Yingjin Wei, Fei Du, Gang Chen, et al. “Two-dimensional vanadium carbide (V2C) MXene as electrode for supercapacitors with aqueous electrolytes”. In: *Electrochemistry Communications* 96 (2018), pp. 103–107.

[102] Meng Wu, Bingxin Wang, Qianku Hu, Libo Wang, and Aiguo Zhou. “The Synthesis Process and Thermal Stability of V2C MXene”. In: *Materials* 11.11 (2018), p. 2112.

[103] Minh H Tran, Timo Schäfer, Ali Shahraei, Michael Dürrschnabel, Leopoldo Molina-Luna, Ulrike I Kramm, and Christina S Birkel. “Adding a New Member to the MXene Family: Synthesis, Structure, and Electrocatalytic Activity for the Hydrogen Evolution Reaction of V4C3T x”. In: *ACS Applied Energy Materials* 1.8 (2018), pp. 3908–3914.

[104] HaM Rietveld. “A profile refinement method for nuclear and magnetic structures”. In: *Journal of applied Crystallography* 2.2 (1969), pp. 65–71.

[105] Ayeong Byeon, Meng-Qiang Zhao, Chang E Ren, Joseph Halim, Sankalp Kota, Patrick Urbankowski, Babak Anasori, Michel W Barsoum, and Yury Gogotsi. “Two-dimensional titanium carbide MXene as a cathode material for hybrid magnesium/lithium-ion batteries”. In: *ACS applied materials & interfaces* 9.5 (2016), pp. 4296–4300.

[106] Huimin Xu, Zhonghua Zhang, Zili Cui, Aobing Du, Chenglong Lu, Shanmu Dong, Jun Ma, Xinhong Zhou, and Guanglei Cui. “Strong anion receptor-assisted boron-based Mg electrolyte with wide electrochemical window and non-nucleophilic characteristic”. In: *Electrochemistry Communications* 83 (2017), pp. 72–76.

[107] Ning Ding, Lan Zhou, Changwei Zhou, Dongsheng Geng, Jin Yang, Sheau Wei Chien, Zhaolin Liu, Man-Fai Ng, Aishui Yu, TS Andy Hor, et al. “Building better lithium-sulfur batteries: from LiNO 3 to solid oxide catalyst”. In: *Scientific reports* 6 (2016), p. 33154.

[108] EL-CELL. *User Manual*. Version 2.31. 2018. URL: `https://el-cell.com/wp-content/uploads/downloads/manuals/Manual_PAT-Cell_Release_2.31.pdf` (visited on 02/06/2019).

[109] William Lawrence Bragg. “The diffraction of short electromagnetic waves by a crystal”. In: *Scientia* 23(45):153 (1929).

[110] Chunfeng Hu, Lingfeng He, Mingyue Liu, Xiaohui Wang, Jingyang Wang, Meishuan Li, Yiwang Bao, and Yanchun Zhou. “In situ reaction synthesis and mechanical properties of V2AlC”. In: *Journal of the American Ceramic Society* 91.12 (2008), pp. 4029–4035.

[111] Maria R Lukatskaya, Seong-Min Bak, Xiqian Yu, Xiao-Qing Yang, Michel W Barsoum, and Yury Gogotsi. “Probing the mechanism of high capacitance in 2D titanium carbide using in situ X-ray absorption spectroscopy”. In: *Advanced Energy Materials* 5.15 (2015), p. 1500589.

[112] Min Xu, Shulai Lei, Jing Qi, Qingyun Dou, Lingyang Liu, Yulan Lu, Qing Huang, Siqi Shi, and Xingbin Yan. “Opening magnesium storage capability of two-dimensional MXene by intercalation of cationic surfactant”. In: *ACS nano* 12.4 (2018), pp. 3733–3740.

[113] Hunter O Ford, Laura C Merrill, Peng He, Sunil P Upadhyay, and Jennifer L Schaefer. “Cross-Linked Ionomer Gel Separators for Polysulfide Shuttle Mitigation in Magnesium–Sulfur Batteries: Elucidation of Structure–Property Relationships”. In: *Macromolecules* 51.21 (2018), pp. 8629–8636.

Appendix A

Additional figures

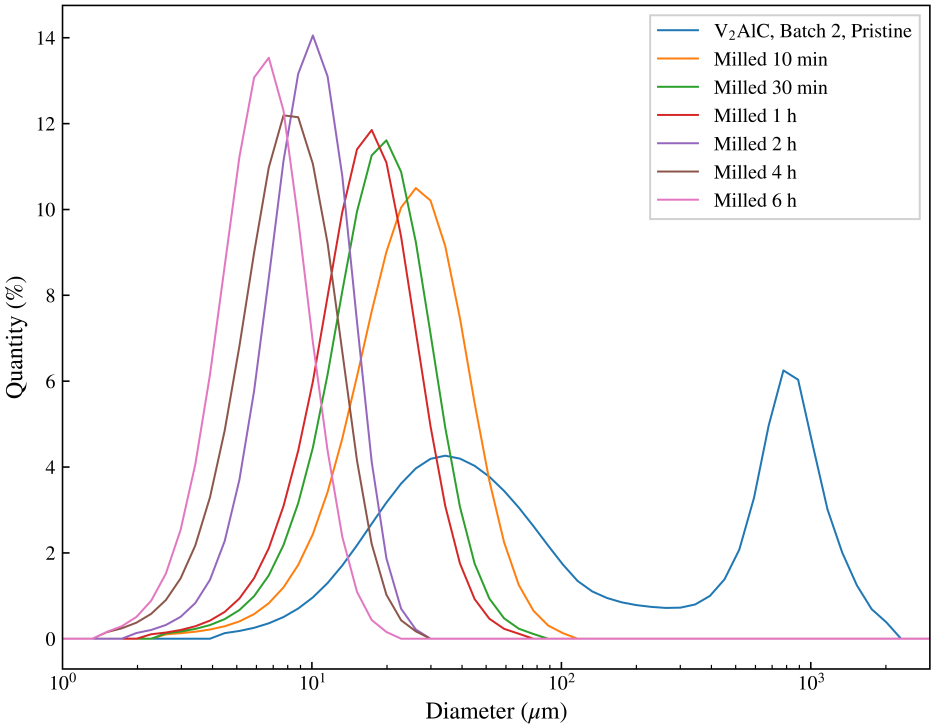

Figure A.1: Particle size distributions of the V_2AlC MAX phase powder from Batch 2 prior to and after 10 min, 30 min, 1h, 2h, 4h and 6h of milling at 300 RPM

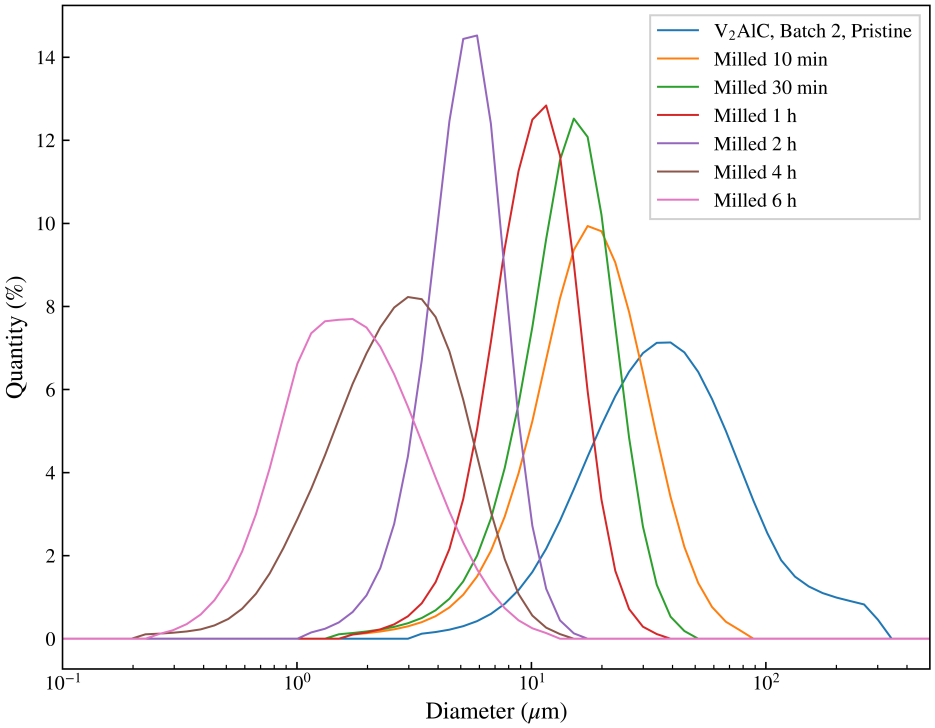

Figure A.2: Particle size distributions of the V_2AlC MAX phase powder from Batch 2 prior to and after 10 min, 30 min, 1h, 2h, 4h and 6h of milling at 400 RPM

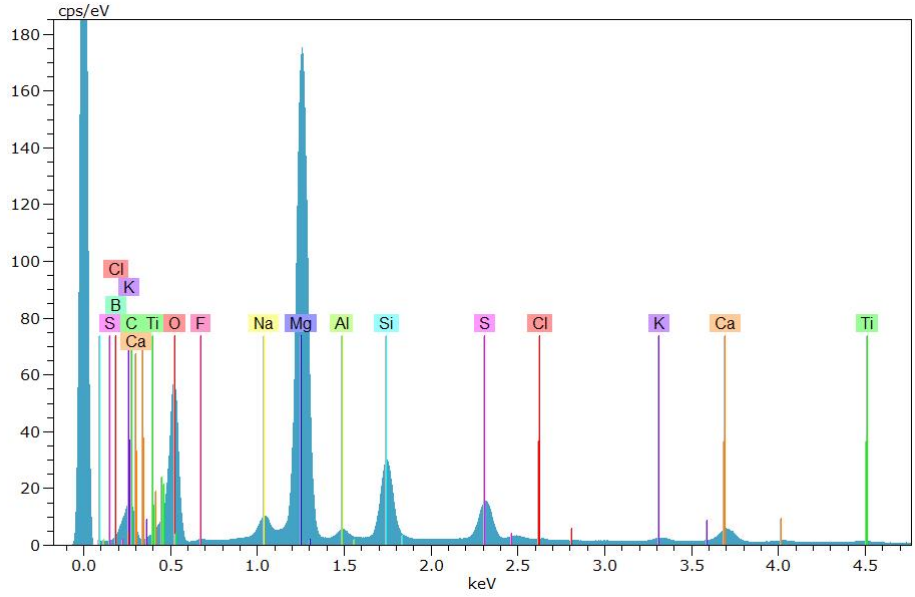

(a)

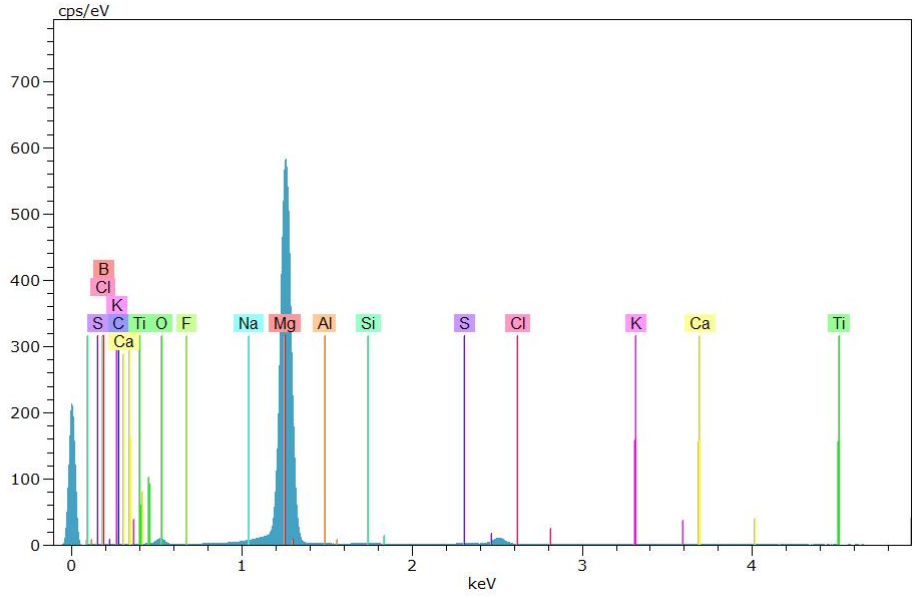

(b)

Figure A.3: EDX spectra resulting from area scans of the anode from the three electrode cell (Mg/BMOC/V_2C-S-3-Electrode) after 110 cycles. The measurements were conducted on the side of the anode that was in contact with the separator during cycling, and (a) and (b) correspond to the area scans of area number 1 and 2 (illustrated in figure 4.32), respectively.

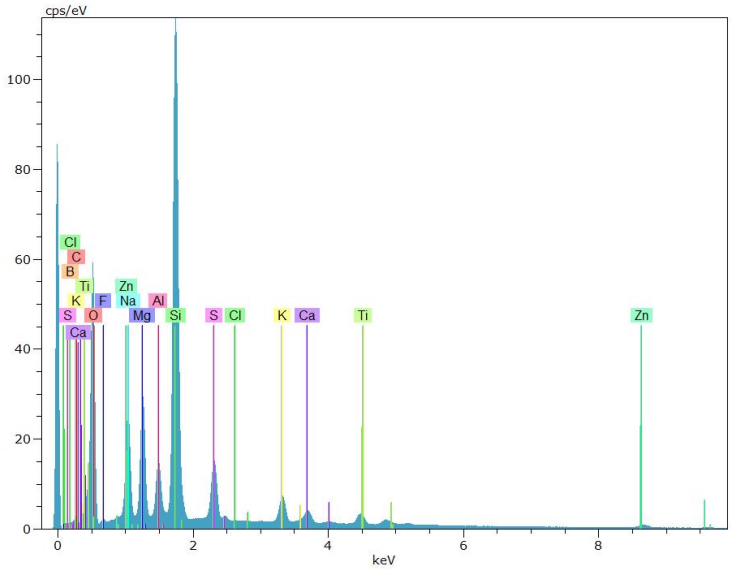

(a)

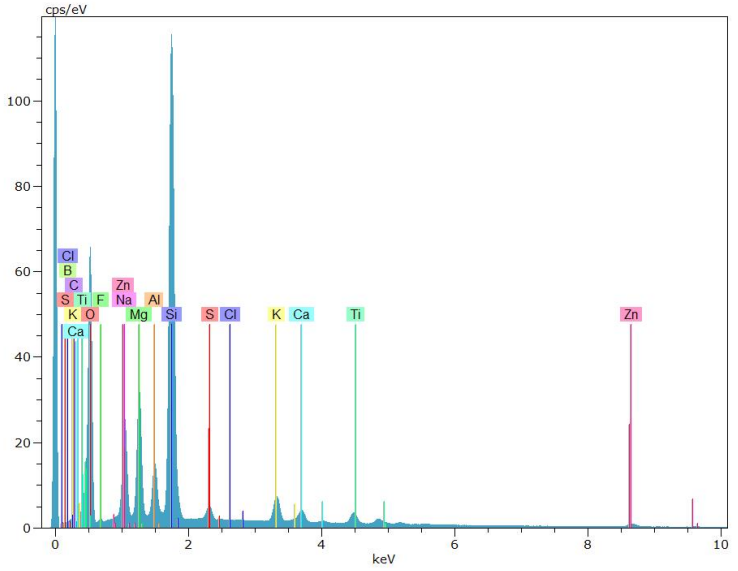

(b)

Figure A.4: EDX spectra resulting from area scans of the separator from the three electrode cell after 110 cycles, where (a) is the scan performed on the side of the separator that was in contact with the anode during cycling and (b) is the scan performed on the side of the separator that was in contact with the cathode during cycling.

Appendix B

Electrochemical results

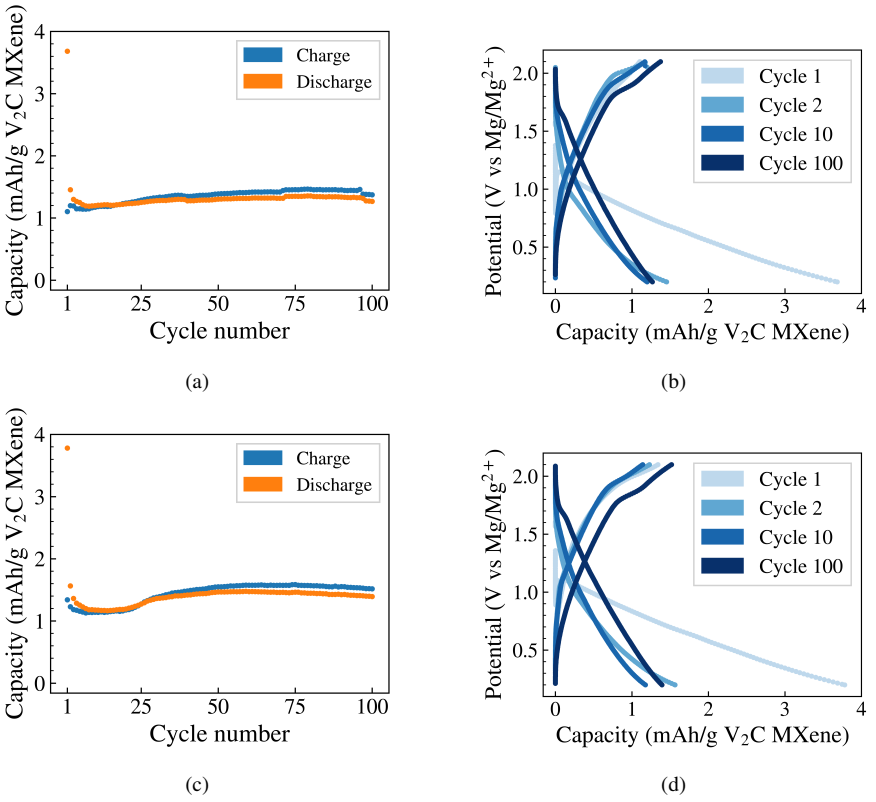

Figure B.1: Cycling performance and voltage profiles for cycle number 1, 2, 10 and 100 for V_2C MXene insertion cathodes from Batch 1 with APC-THF electrolyte; Mg/APC/V_2C-B1-1 (a and b) and Mg/APC/V_2C-B1-2 (c and d). The cells were cycled with the standard cycling programme.

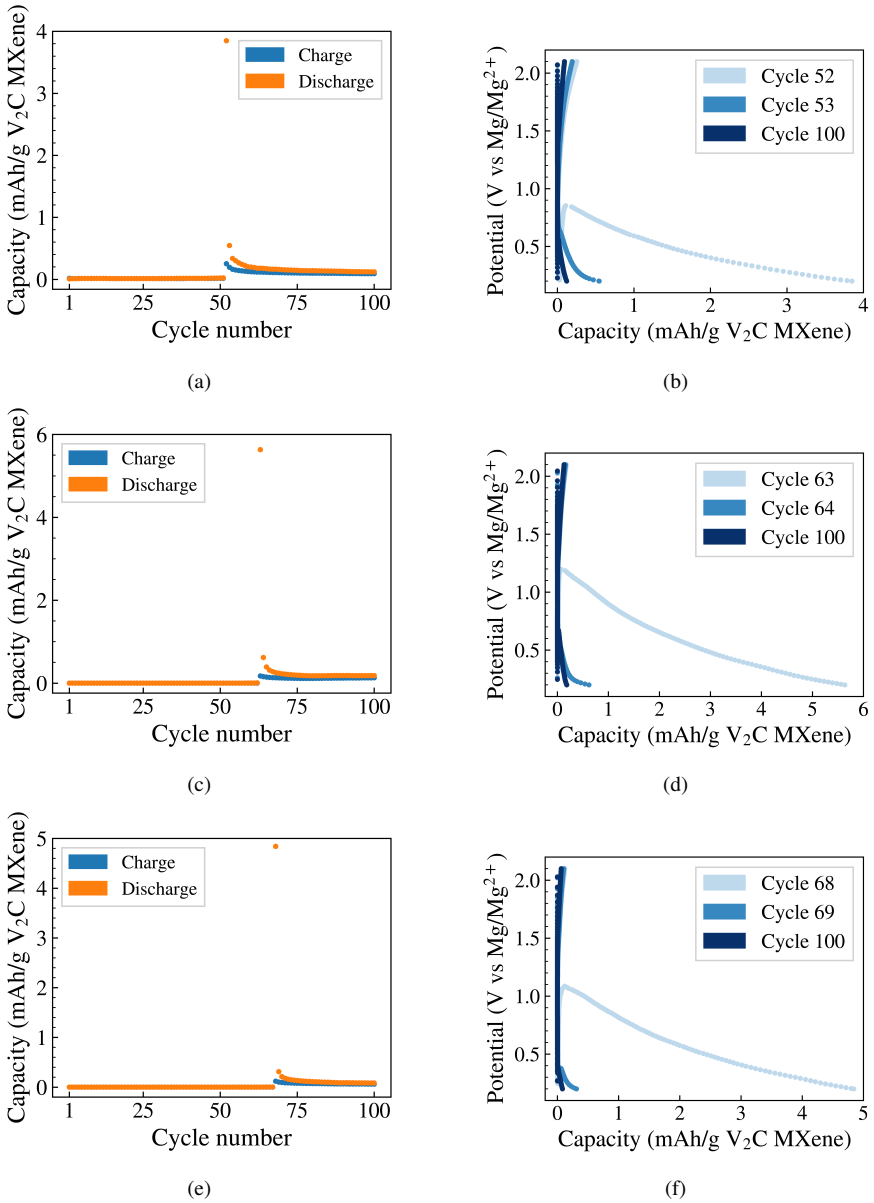

Figure B.2: Cycling performance and voltage profiles for the first, second, tenth and final cycle (counting from the first cycle where proper cycling behaviour was observed) for V_2C MXene insertion cathodes from Batch 1 with BMOC-DME electrolyte; Mg/BMOC/V_2C-B1-1 (a and b), Mg/BMOC/V_2C-B1-2 (c and d) and Mg/BMOC/V_2C-B1-3 (e and f). The cells were cycled with the standard cycling programme.

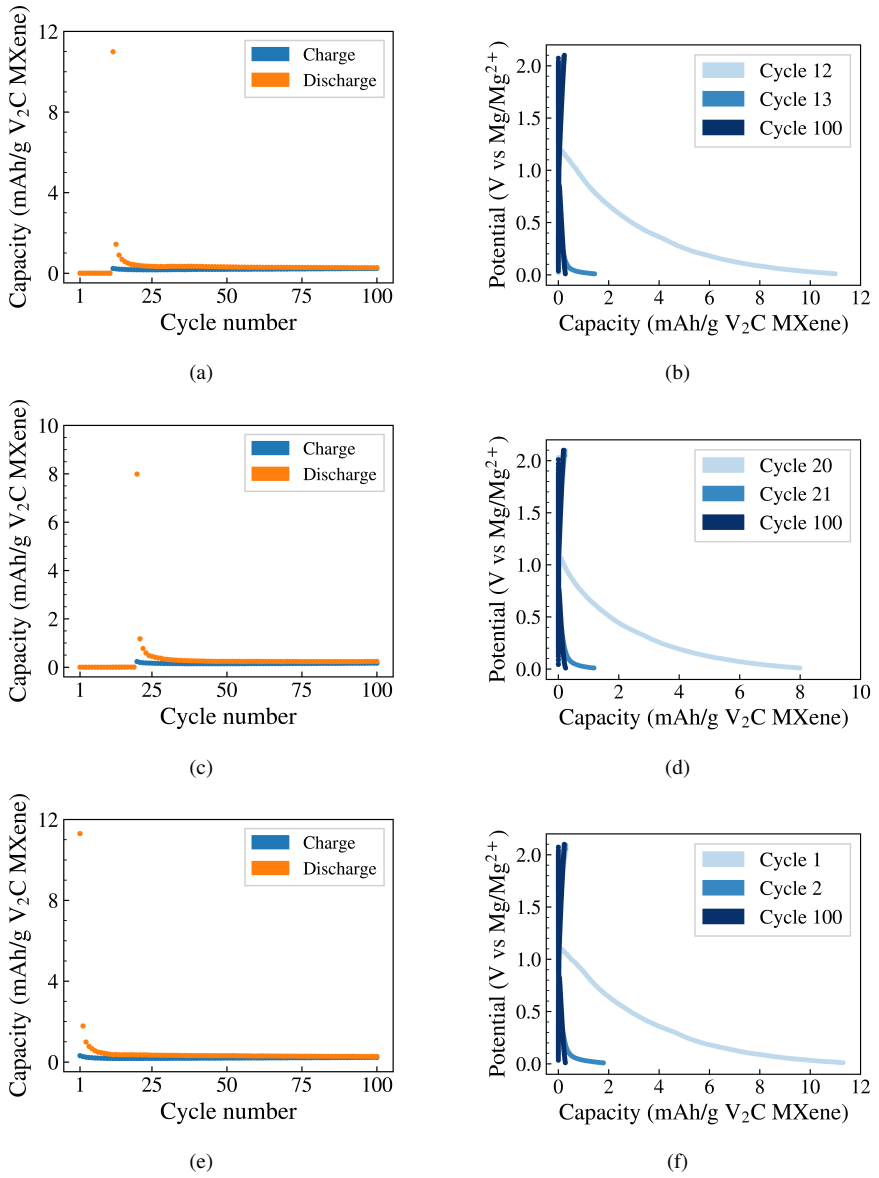

Figure B.3: Cycling performance and voltage profiles for the first, second, tenth and final cycle (counting from the first cycle where proper cycling behaviour was observed) for V_2C MXene insertion cathodes from Batch 1 with BMOC-DME electrolyte; Mg/BMOC/V_2C-B1-4 (a and b), Mg/BMOC/V_2C-B1-5 (c and d) and Mg/BMOC/V_2C-B1-6 (e and f). The cells were cycled with the extended cycling programme.

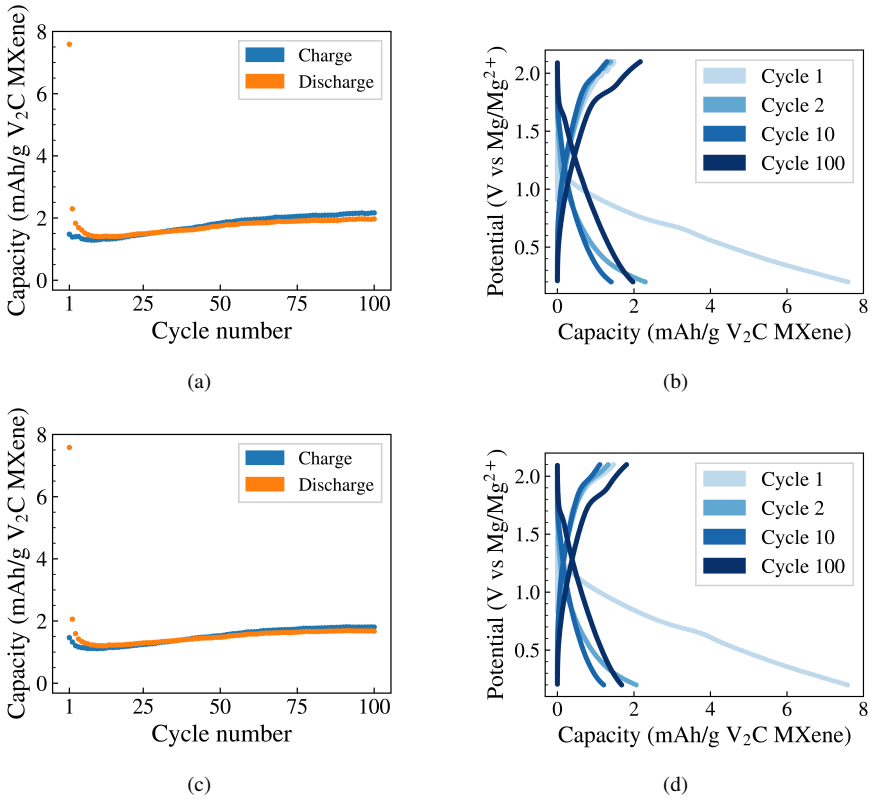

Figure B.4: Cycling performance and voltage profiles for cycle number 1, 2, 10 and 100 for V_2C MXene insertion cathodes from Batch 2 with APC-THF electrolyte; Mg/APC/V_2C-B2-1 (a and b) and Mg/BMOC/V_2C-B2-2 (c and d). The cells were cycled with the standard cycling programme.

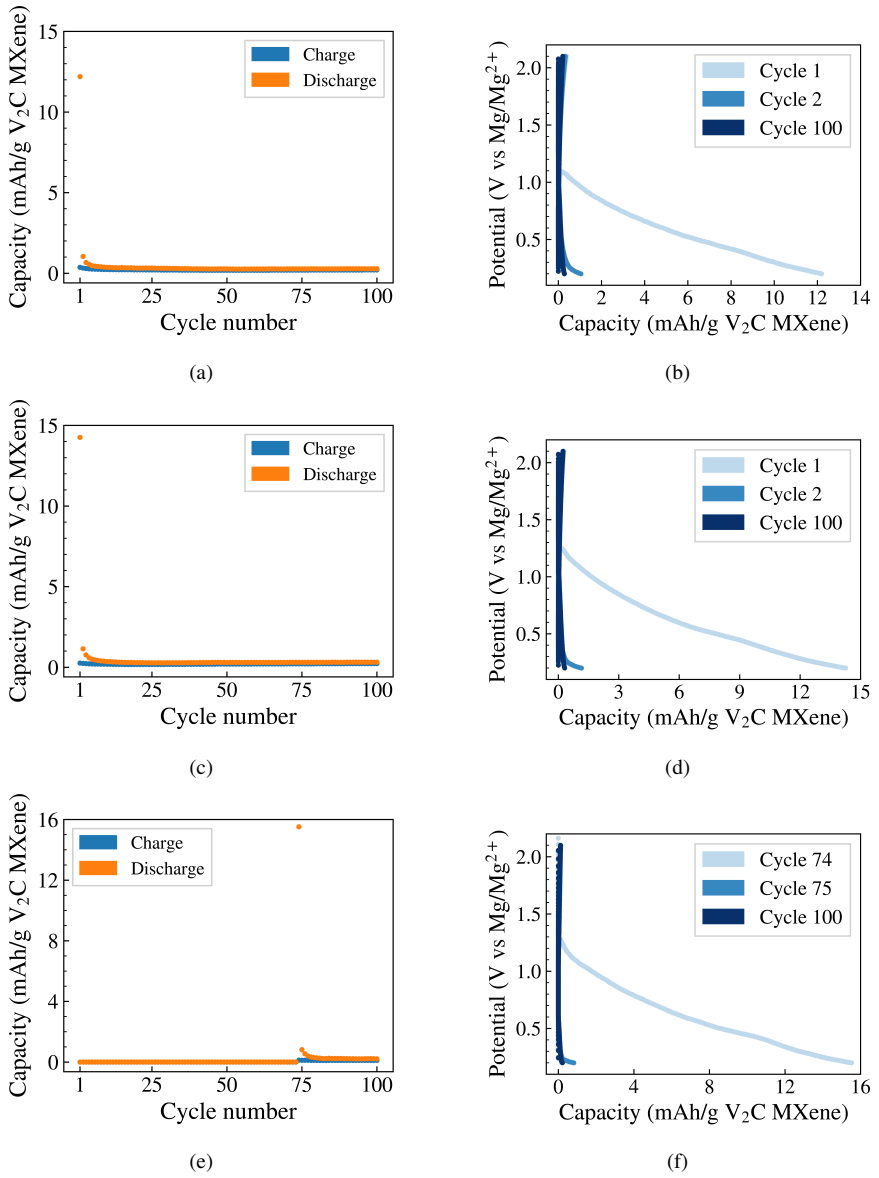

Figure B.5: Cycling performance and voltage profiles for the first, second, tenth and final cycle (counting from the first cycle where proper cycling behaviour was observed) for V_2C MXene insertion cathodes from Batch 2 with BMOC-DME electrolyte; Mg/BMOC/V_2C-B2-1 (a and b), Mg/BMOC/V_2C-B2-2 (c and d) and Mg/BMOC/V_2C-B2-3 (e and f). The cells were cycled with the standard cycling programme.